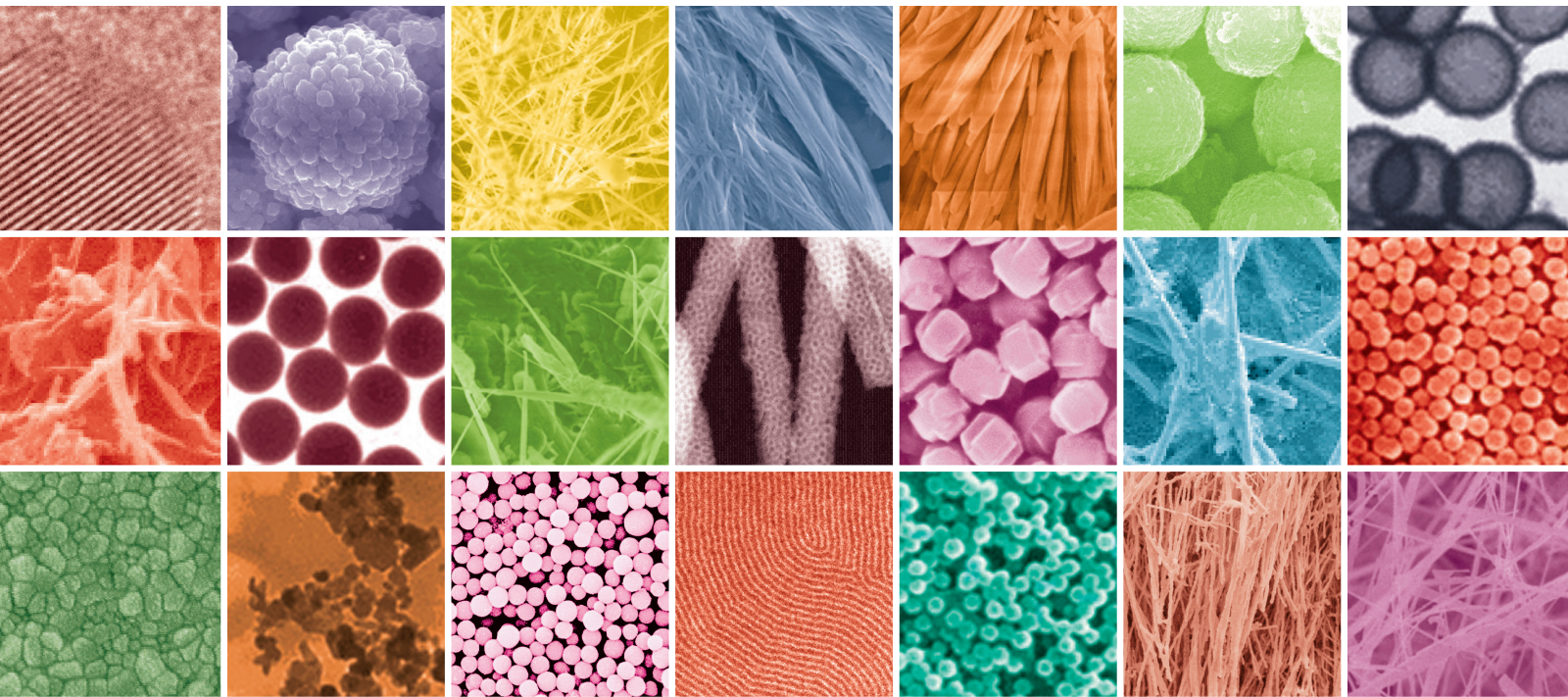


Mechanical Behavior of Nanostructured Materials

Guest Editors: Ning Hu, Xi-Qiao Feng, Shao-Yun Fu, Cheng Yan, Guang-Ping Zhang, and Jihua Gou





Mechanical Behavior of Nanostructured Materials

Mechanical Behavior of Nanostructured Materials

Guest Editors: Ning Hu, Xi-Qiao Feng, Shao-Yun Fu, Cheng Yan, Guang-Ping Zhang, and Jihua Gou



Copyright © 2015 Hindawi Publishing Corporation. All rights reserved.

This is a special issue published in "Journal of Nanomaterials." All articles are open access articles distributed under the Creative Commons Attribution License, which permits unrestricted use, distribution, and reproduction in any medium, provided the original work is properly cited.

Editorial Board

Katerina Aifantis, Greece
Nageh K. Allam, USA
Margarida Amaral, Portugal
Xuedong Bai, China
Enrico Bergamaschi, Italy
Theodorian Borca-Tasciuc, USA
C. Jeffrey Brinker, USA
Christian Brosseau, France
Xuebo Cao, China
Sang-Hee Cho, Republic of Korea
Shafiq Chowdhury, USA
Cui Chunxiang, China
Miguel A. Correa-Duarte, Spain
Shadi A. Dayeh, USA
Ali Eftekhari, USA
Claude Estournes, France
Alan Fuchs, USA
Lian Gao, China
Russell E. Gorga, USA
Hongchen Chen Gu, China
Mustafa O. Guler, Turkey
John Zhanhu Guo, USA
Smrati Gupta, Germany
Michael Harris, USA
Zhongkui Hong, USA
Michael Z. Hu, USA
David Hui, USA
Y.-K. Jeong, Republic of Korea
Sheng-Rui Jian, Taiwan
Wanqin Jin, China
Rakesh K. Joshi, India
Zhenhui Kang, China

Fathallah Karimzadeh, Iran
Do Kyung Kim, Republic of Korea
Kin Tak Lau, Australia
Burtrand Lee, USA
Benxia Li, China
Jun Li, Singapore
Shijun Liao, China
Gong Ru Lin, Taiwan
J.-Y. Liu, USA
Jun Liu, USA
Tianxi Liu, China
Songwei Lu, USA
Daniel Lu, China
Jue Lu, USA
Ed Ma, USA
Gaurav Mago, USA
Sanjay R. Mathur, Germany
Nobuhiro Matsushita, Japan
A. McCormick, USA
Vikas Mittal, UAE
Weihai Ni, Germany
Sherine Obare, USA
Edward Andrew Payzant, USA
Kui-Qing Peng, China
Anukorn Phuruangrat, Thailand
Ugur Serincan, Turkey
Huaiyu Shao, Japan
Donglu Shi, USA
Suprakas Sinha Ray, South Africa
Vladimir Sivakov, Germany
Marinella Striccoli, Italy
Bohua Sun, South Africa

Saikat Talapatra, USA
Nairong Tao, China
Titipun Thongtem, Thailand
Somchai Thongtem, Thailand
Valeri P. Tolstoy, Russia
Tsung-Yen Tsai, Taiwan
Takuya Tsuzuki, Australia
Raquel Verdejo, Spain
Mat U. Wahit, Malaysia
Shiren Wang, USA
Yong Wang, USA
Cheng Wang, China
Zhenbo Wang, China
Jinquan Wei, China
Ching Ping Wong, USA
Xingcai Wu, China
Guodong Xia, Hong Kong
Zhi Li Xiao, USA
Ping Xiao, UK
Shuangxi Xing, China
Yangchuan Xing, USA
N. Xu, China
Doron Yadlovker, Israel
Ying-Kui Yang, China
Khaled Youssef, USA
Kui Yu, Canada
Haibo Zeng, China
Tianyou Zhai, Japan
Renyun Zhang, Sweden
Yanbao Zhao, China
Lianxi Zheng, Singapore
Chunyi Zhi, Japan

Contents

Mechanical Behavior of Nanostructured Materials, Ning Hu, Xi-Qiao Feng, Shao-Yun Fu, Cheng Yan, Guang-Ping Zhang, and Jihua Gou
Volume 2015, Article ID 829367, 2 pages

Fabrication of Al₂O₃-Cu Nanocomposites Using Rotary Chemical Vapor Deposition and Spark Plasma Sintering, Jianfeng Zhang and Takashi Goto
Volume 2015, Article ID 790361, 7 pages

Molecular Dynamics Study on the Effect of Temperature on the Tensile Properties of Single-Walled Carbon Nanotubes with a Ni-Coating, Fulong Zhu, Hengyou Liao, Kai Tang, Youkai Chen, and Sheng Liu
Volume 2015, Article ID 767182, 7 pages

Enhancement in Mode II Interlaminar Fracture Toughness at Cryogenic Temperature of Glass Fiber/Epoxy Composites through Matrix Modification by Carbon Nanotubes and n-Butyl Glycidyl Ether, Yu Liu, Cheng-Bing Qu, Qing-Ping Feng, Hong-Mei Xiao, and Shao-Yun Fu
Volume 2015, Article ID 812061, 6 pages

Micromechanical Behavior of Single-Crystal Superalloy with Different Crystal Orientations by Microindentation, Jinghui Li, Fuguo Li, Junzhe Dong, Zhanwei Yuan, and Shuo Zhang
Volume 2015, Article ID 759753, 15 pages

Atomic Structure and Energy Distribution of Collapsed Carbon Nanotubes of Different Chiralities, Julia A. Baimova, Qin Fan, Liangcai Zeng, Zhigang Wang, Sergey V. Dmitriev, Xiqiao Feng, and Kun Zhou
Volume 2015, Article ID 186231, 5 pages

Mechanisms of Hydrogen Transport in Flexible-Wall Narrow Carbon Nanotubes, Bin-Hao Chen, Chieh Kung, and I-Peng Chu
Volume 2015, Article ID 959402, 10 pages

Preparation and Flame Retardant and Smoke Suppression Properties of Bamboo-Wood Hybrid Scrimber Filled with Calcium and Magnesium Nanoparticles, Bin Fu, Xingong Li, Guangming Yuan, Weimin Chen, and Yage Pan
Volume 2014, Article ID 959135, 6 pages

The Nanomechanical and Tribological Properties of Restorative Dental Composites after Exposure in Different Types of Media, Hong-Yi Fan, Xue-Qi Gan, Yang Liu, Zhuo-Li Zhu, and Hai-Yang Yu
Volume 2014, Article ID 759038, 9 pages

Interaction Potential between Parabolic Rotator and an Outside Particle, Dan Wang, Yajun Yin, Jiye Wu, Xugui Wang, and Zheng Zhong
Volume 2014, Article ID 464925, 8 pages

Editorial

Mechanical Behavior of Nanostructured Materials

Ning Hu,¹ Xi-Qiao Feng,² Shao-Yun Fu,³ Cheng Yan,⁴ Guang-Ping Zhang,⁵ and Jihua Gou⁶

¹College of Aerospace Engineering, Chongqing University, Chongqing 400044, China

²College of Aerospace Engineering, Tsinghua University, Beijing 100084, China

³Technical Institute of Physics and Chemistry, Chinese Academy of Sciences, Beijing 100190, China

⁴School of Chemistry, Physics and Mechanical Engineering, Queensland University of Technology, GPO Box 2434, Brisbane, QLD 4000, Australia

⁵Shenyang National Laboratory for Materials Science, Institute of Metal Research, Chinese Academy of Sciences, Shenyang 110016, China

⁶Department of Mechanical and Aerospace Engineering, University of Central Florida, Orlando, FL 32816, USA

Correspondence should be addressed to Ning Hu; ninghu@cqu.edu.cn

Received 16 March 2015; Accepted 16 March 2015

Copyright © 2015 Ning Hu et al. This is an open access article distributed under the Creative Commons Attribution License, which permits unrestricted use, distribution, and reproduction in any medium, provided the original work is properly cited.

This Special Issue presents recent research advances in various aspects of advanced nanomaterials including synthesis, micro- and nanostructures, mechanical properties, modeling, and applications for material nanotechnology community. In particular, it aims to reflect recent advances in mechanical behaviors, for example, stiffness, strength, ductility, fatigue, and wear resistance, of various nanomaterials including nanocrystalline, inorganic, nonmetallic nanomaterials, composites with nanosized fillers, and biomaterials with nanosized structures. The role of this Special Issue is to bridge the gaps among fabrication techniques, experimental techniques, numerical modeling, and applications for some new nanomaterials and to investigate some key issues related to the mechanical properties of the nanomaterials. It brings together researchers working at the frontier of the mechanical behavior of nanomaterials.

Nanomaterials are truly multidisciplinary. Technically most important properties are mechanical, electrical, catalytic, magnetic, optical, and so forth. Research at the nanoscale material frontier needs to be unified by sharing knowledge, techniques, and expertise on atomic, molecular, and microinteractions. In particular, regarding the mechanical properties, despite the progress made in technology of such materials, their application is still restricted by insufficient experimental data, numerical modeling results, and their interpretation. This applies to the knowledge describing

mechanical behaviors of the above nanomaterials under various conditions, for example, static, dynamic, monotonic, and cyclic conditions, at low and high temperatures. The articles of this Special Issue are grouped in the following main topics: (1) numerical modeling and evaluation of mechanical properties of various nanomaterials; (2) preparation and fabrication technologies and their effects on the mechanical properties of various nanomaterials; (3) experimental characterization of mechanical properties of various nanomaterials.

In the first group, by virtue of molecular dynamics simulations or other numerical means, there are some papers dealing with the mechanical properties of some typical nanomaterials, for example, carbon nanotubes. For example, in aspect of molecular dynamics simulations, the mechanical and structural properties of some collapsed carbon nanotubes and the effects of geometric parameters of carbon nanotubes, such as length, diameter, and chirality, were investigated at atomic scale. The dependence of newly formed rippled structure of the carbon nanotubes after relaxation on the chirality was interestingly uncovered. Moreover, the effect of temperature on the tensile property of single-walled carbon nanotubes processed by a surface Ni-coating technology was explored by molecular dynamics simulations. Due to coated Ni, the possibility of degraded mechanical properties of the single-walled carbon nanotubes was demonstrated. Also, the interaction between hydrogen and carbon nanotubes

was studied using molecular dynamics simulations, and the mechanisms of hydrogen transport in flexible-wall narrow carbon nanotubes were uncovered. Furthermore, at micro/nanoscale, the interaction potential between parabolic rotator and a particle located outside the rotator was numerically studied on the basis of a negative exponential pair potential between particles. It was found that curvatures and the gradient of curvatures are the essential elements forming the driving forces. Through the idealized numerical experiments, the accuracy of the curvature-based potential was preliminarily proven.

The second group collects the research works regarding preparation and fabrication technologies and their effects on the mechanical properties of various nanomaterials. For instance, the mechanical and tribological properties of dental nanocomposites and the effects of acidic solutions were investigated in detail. Compared with microscale fillers, nanoscale fillers can effectively improve the mechanical properties of the dental nanocomposites, for example, hardness and elastic modulus. Also, the acidic solutions can change the failure mechanisms of the dental nanocomposites under the condition of wearing. Moreover, a new fabrication technology which combines rotary chemical vapor deposition and spark plasma sintering together for Al_2O_3 -Cu nanocomposites was proposed. The positive effects of Cu nanoparticles on the nanocomposites' fracture toughness were experimentally confirmed. Moreover, a matrix modification technique by using carbon nanotubes and n-butyl glycidyl ether was developed. The interlaminar fracture toughness of glass fiber/epoxy nanocomposites at cryogenic temperature was confirmed to be increased significantly.

Finally, the papers in the third group describe experimental evaluation of properties of various nanomaterials. For instance, the micromechanical behaviors of single-crystal superalloy with different crystal orientations were characterized by microindentation technology. The reduction of the microhardness H due to dislocation hardening and the relationship between Young's modulus E and interplanar spacing and crystal variable were confirmed experimentally. Furthermore, a simplified material model was proposed to consider the various crystal orientations, and it was verified by a 3D microindentation simulation approach. As for the mechanical and flame retardant and smoke properties of bamboo-wood hybrid scrimber filled by two kinds of nanoparticles, that is, calcium and magnesium, a detailed exploration about the experimental characterization of the above properties was carried out. The confirmation of the improvement of the above physical and mechanical properties after adding the nanoparticles was also obtained.

We first want to congratulate the authors who made this Special Issue possible. Sincere thanks are due to the reviewers for their very accurate and voluntary job. This is the first time the Journal of Nanomaterials had a Special Issue focusing on mechanical properties of various advanced nanomaterials as well as the influences of fabrication techniques, microstructures, and so forth, on them, from the aspects of the numerical and experimental approaches. It should be very helpful to enhance the effective applications of these advanced

nanomaterials. We are grateful to this journal for the support given to the approval and realization of this Special Issue.

*Ning Hu
Xi-Qiao Feng
Shao-Yun Fu
Cheng Yan
Guang-Ping Zhang
Jihua Gou*

Research Article

Fabrication of Al₂O₃-Cu Nanocomposites Using Rotary Chemical Vapor Deposition and Spark Plasma Sintering

Jianfeng Zhang¹ and Takashi Goto²

¹College of Mechanics and Materials, Hohai University, Nanjing 210098, China

²Institute for Materials Research, Tohoku University, Sendai 980-8577, Japan

Correspondence should be addressed to Jianfeng Zhang; jfzhang_sic@163.com

Received 15 August 2014; Revised 30 October 2014; Accepted 31 October 2014

Academic Editor: Shaoyun Fu

Copyright © 2015 J. Zhang and T. Goto. This is an open access article distributed under the Creative Commons Attribution License, which permits unrestricted use, distribution, and reproduction in any medium, provided the original work is properly cited.

A two-step rotary chemical vapor deposition technique was developed to uniformly mix Cu nanoparticles with the γ -Al₂O₃ powders, and then the as-obtained powders were consolidated to Al₂O₃-Cu nanocomposites by spark plasma sintering. In the RCVD process, the metal-organic precursor of copper dipivaloylmethanate (Cu(DPM)₂) reacted with O₂ and then was reduced by H₂ in order to erase the contamination of carbon. At 1473 K, the relative density of Al₂O₃-Cu increased with increasing C_{Cu} and the maximum value was 97.7% at C_{Cu} = 5.2 mass%. The maximum fracture toughness of Al₂O₃-Cu was 4.1 MPa m^{1/2} at C_{Cu} = 3.8 mass%, and 1 MPa m^{1/2} higher than that of monolithic Al₂O₃, validating the beneficial effects of Cu nanoparticles.

1. Introduction

The incorporation of small amounts of metal nanoparticles, such as Cu [1], Ni [2–4], W [5], and Cr [6], has been proved to be beneficial for improving the densification, mechanical properties, and conductivity of Al₂O₃. Particularly, the incorporation of Cu nanoparticles has attracted much attention due to its high ductility and good electrical conductivity [1, 7, 8]. Kim et al. fabricated Al₂O₃-Cu nanopowders by ball milling for 30 h and then sintered at 1100–1400°C for 5 min in vacuum under a pressure of 50 MPa by the pulse electric current sintering (PECS) [7]. The composites sintered at 1250°C for 5 min showed a relative density above 97% and enhanced fracture toughness of 4.5 MPa m^{1/2}. Oh and Yoon fabricated Al₂O₃-Cu nanocomposites by hydrogen reduction and hot pressing of Al₂O₃/CuO powders. The composite prepared from Al₂O₃-Cu nitrate mixture exhibited maximum strength of 953 MPa [8].

In general, that the wet methods such as coprecipitation usually produces γ -Al₂O₃ phase, which would transform to α -Al₂O₃ during high temperature sintering. Thus the uniform distribution of Cu would be quite necessary for high mechanical properties. However, the agglomeration of Cu

nanoparticles in sol-gel process and ball milling is usually unavoidable [9]. Compared to the ball milling and wet sol-gel, the dry CVD technique seems more promising due to its easy operation and low pollution to the environments. Fluidized bed CVD (FBCVD) is one of the most efficient CVD techniques to coat each individual particle of a powder from gaseous species [10]. However, the application of FBCVD on powder is limited depending mainly on density and particle size of powder [11, 12]. The use of a novel rotary CVD (RCVD) technique to prepare Ni nanoparticles on ceramic powders has been reported in our previous work. Ni nanoparticles 13.9–84.5 nm and 10–100 nm in diameter were precipitated on the surface of hBN [13] and cBN [14], respectively. The relative density and hardness of hBN were found to be increased by the incorporation of Ni nanoparticles. The hardness of Al₂O₃-30 vol% cBN/Ni was 27 GPa, about 1 GPa and 5 GPa higher than that of Al₂O₃-30 vol% cBN and monolithic Al₂O₃.

In the present study, Cu nanoparticle was precipitated on γ -Al₂O₃ for uniform mixture by RCVD using copper dipivaloylmethanate (Cu(DPM)₂) as a precursor. In order to erase the carbon contamination, the powder was firstly oxidized by oxygen and then reduced by hydrogen into the metal state.

Then the $\gamma\text{Al}_2\text{O}_3$ -Cu powders were consolidated by spark plasma sintering at 1373 to 1573 K for 0.6 ks. The effects of Cu nanoparticles on the sintering behavior, microstructure, and mechanical properties of Al_2O_3 were investigated.

2. Experimental Procedures

The detailed description about RCVD can be found elsewhere [13]. In the present study, Cu nanoparticles were precipitated on $\gamma\text{Al}_2\text{O}_3$ powders by RCVD at 573 to 873 K for 30 min using $\text{Cu}(\text{DPM})_2$ as a precursor. The $\text{Cu}(\text{DPM})_2$ precursor in the evaporator was heated at 393 to 423 K and carried into the reaction zone by Ar at a flow rate of $1.67 \times 10^{-6} \text{ m}^3 \cdot \text{s}^{-1}$. The supply rate (R_s) of $\text{Cu}(\text{DPM})_2$ was set at $0.56 \times 10^{-6} \text{ kg} \cdot \text{s}^{-1}$, and O_2 was also filled in to erase the carbon contamination from $\text{Cu}(\text{DPM})_2$. The $\gamma\text{Al}_2\text{O}_3$ powder, <100 nm in average diameter and 2 g in weight, was fed into the reactor and preheated at 793 to 823 K. The total inner pressure of the RCVD apparatus was kept at 800 Pa with a partial pressure of 240 Pa for O_2 and 560 Pa for Ar. The deposition time was fixed at 1.8 ks. After deposition, the O_2 was cut off and H_2 was used to reduce the CuO to Cu. The $\gamma\text{Al}_2\text{O}_3$ -Cu powder was consolidated by spark plasma sintering (SPS, model SPS-210LX, SPS Syntex Inc., Japan) at 1373 to 1673 K for 0.6 ks. The heating rate was $3.3 \text{ K} \cdot \text{s}^{-1}$ and the pressure was 100 MPa loaded in the whole sintering process. The temperature was measured by an optical pyrometer focused on a hole ($\phi 2 \times 5 \text{ mm}$) in the graphite die.

The crystal structure and phase of the $\gamma\text{Al}_2\text{O}_3$ -Cu powder and the sintered bodies were identified by X-ray diffraction (XRD) with $\text{CuK}\alpha$ radiation. The microstructure was observed by scanning electron microscopy (SEM) and transmission electron microscopy (TEM). The Cu mass content (hereafter, C_{Cu}) in the Al_2O_3 -Cu powder was estimated by energy-dispersive X-ray spectroscopy (EDS) and was averaged by five measurements at different areas. The specific surface area, a total surface area per unit of mass, was measured by the BET method and calculated using [15]

$$a_{\text{BET}} = \frac{V_m L a_m}{V_L}. \quad (1)$$

Here a_m is the area occupied by a molecule of the adsorbate, L is the Avogadro's number, and V_L is the molar volume of the analysis gas at standard temperature and pressure (STP). V_m is the monolayer adsorbed gas quantity, which could be obtained from

$$\frac{P}{V(P - P_0)} = \frac{1}{V_m} \left(\frac{1}{C} + \frac{C - 1}{C} \times \frac{P}{P_0} \right). \quad (2)$$

Here P and P_0 are the equilibrium and saturation pressure of adsorbates at the temperature of adsorption, V is the adsorbed gas volume quantity, and C is the BET constant.

The bulk density of the sintered body was determined by an Archimedes' method and converted to relative density using the theoretical density of Al_2O_3 ($3.99 \times 10^3 \text{ kg} \cdot \text{m}^{-3}$) [16] and Cu ($8.99 \times 10^3 \text{ kg} \cdot \text{m}^{-3}$) [17]. The hardness of Al_2O_3 -Cu nanocomposites was measured using Vicker's indentation

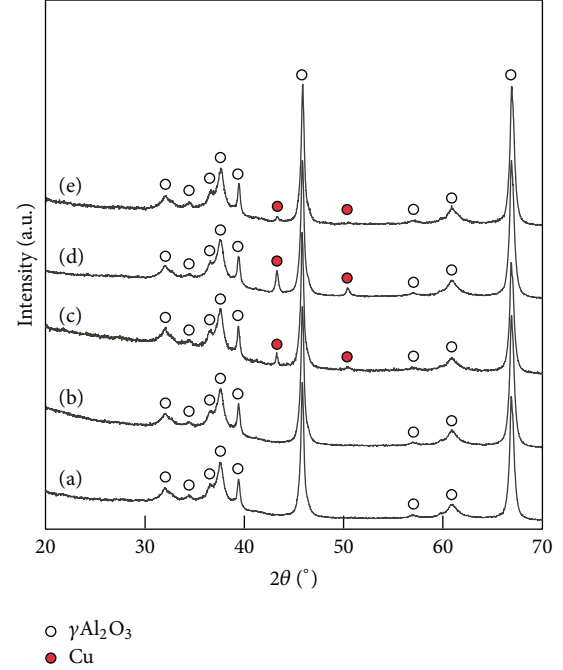


FIGURE 1: XRD patterns of (a) Al_2O_3 and Cu precipitated Al_2O_3 powders at $T_{\text{SPS}} =$ (b) 573, (c) 673, (d) 773, and (e) 873 K.

test under a load of 19.6 N [18] and the fracture toughness was evaluated by measuring the crack length generated by Vicker's indentation [19]. Ten points were averaged for each value of hardness and fracture toughness.

3. Results and Discussion

Figure 1 shows the effects of precipitation temperature (T_p) on phase structure of the RCVD-treated Al_2O_3 powders. At $T_p = 573 \text{ K}$, no Cu peaks were identified due to the low precipitation temperature. At 673 to 873 K, the diffraction peaks at $2\theta = 43.3^\circ$ (111) and 50.5° (200) were indexed to Cu, and no CuO and C peaks were observed. On the other hand, the intensity of Cu peaks varied with the precipitating temperature and showed the highest at 773 K. Figure 2 shows the TEM image and EDS spectrum of Cu precipitated $\gamma\text{Al}_2\text{O}_3$ powders at 773 K. The EDS spectrum showed clearly the presence of Cu peaks. The Mo peaks were also observed due to the Mo mesh grids used to support the powder for TEM observation. However, it is difficult to distinguish the Cu nanoparticles from Al_2O_3 by the TEM images due to the small grain size of Al_2O_3 and Cu. The presence of carbon and oxygen peaks in the EDS spectra was ascribed to the thin organic film coated on the Mo mesh grid to support the powders for TEM observation. Table 1 shows the specific surface area, Cu grain size, and C_{Cu} of Al_2O_3 and Al_2O_3 -Cu powders. The specific surface area of monolithic $\gamma\text{Al}_2\text{O}_3$ was $49.3 \text{ m}^2 \cdot \text{g}^{-1}$. The addition of Cu decreased the specific surface area of Al_2O_3 slightly from 41.8 to $45.4 \text{ m}^2 \cdot \text{g}^{-1}$ due to the high theoretical density of Cu ($\text{kg} \cdot \text{m}^{-3}$). The crystalline grain size of the Cu nanoparticles was obtained by Scherrer's Formula

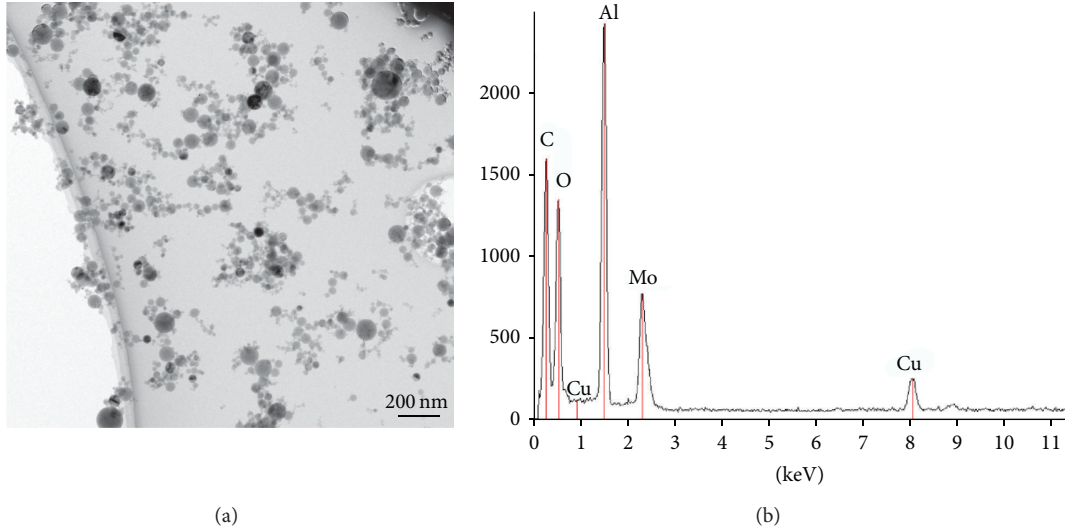


FIGURE 2: (a) TEM image and (b) EDS spectrum of Cu precipitated $\gamma\text{Al}_2\text{O}_3$ powders at $T_p = 773$ K.

TABLE 1: Specific surface area, grain size of Cu and content of Cu in Al_2O_3 and Al_2O_3 -Cu powders.

	Precipitation temperature/K	Specific surface area/ $\text{m}^2 \text{g}^{-1}$	Grain size of Cu*/nm	Content of Cu/mass%
Al_2O_3	—	49.3	—	—
Al_2O_3 -Cu	573	41.8	—	1.2
Al_2O_3 -Cu	673	42.3	18	3.8
Al_2O_3 -Cu	773	45.4	25	5.2
Al_2O_3 -Cu	873	43.8	28	2.1

*The crystalline grain size of the Cu nanoparticles was obtained by Scherrer's formula from the XRD patterns.

for the strongest peak using the diffraction angle of the peak and half width of the peak area of Figure 1. The grain size of Cu increased from 18 to 28 nm with increasing the precipitating temperature from 673 to 873 K. The maximum C_{Cu} reached 5.2 mass% at 773 K.

Figure 3 shows the effect of sintering temperature (T_{SPS}) on the phase structure of Cu precipitated $\gamma\text{Al}_2\text{O}_3$ powders at $T_{\text{SPS}} = 773$ K. The phase transformation of $\gamma\text{Al}_2\text{O}_3$ to $\alpha\text{Al}_2\text{O}_3$ started at $T_{\text{SPS}} = 1273$ K, where three $\alpha\text{Al}_2\text{O}_3$ peaks appeared together with $\gamma\text{Al}_2\text{O}_3$ and Cu peaks. At $T_{\text{SPS}} = 1373$ K, the $\gamma\text{Al}_2\text{O}_3$ transformed completely to $\alpha\text{Al}_2\text{O}_3$.

Figure 4 shows the effect of C_{Cu} on the relative density of Al_2O_3 -Cu nanocomposites. At $T_{\text{SPS}} = 1373, 1473,$ and 1573 K, the relative density of Al_2O_3 was 93.6%, 98.4%, and 97.6%, respectively. The maximum value of 98.4% at $T_{\text{SPS}} = 1473$ K was a little higher than Kim's results at $T_{\text{SPS}} = 1523$ K for 0.3 ks (97%) [7], indicating that RCVD is better in precipitating Cu nanoparticles for the densification of Al_2O_3 . Hotta and Goto have consolidated $\alpha\text{Al}_2\text{O}_3$ by spark plasma sintering from the raw powder of Al_2O_3 of ~ 200 nm in diameter [20]. The relative density at $T_{\text{SPS}} = 1473$ K reached above 99%.

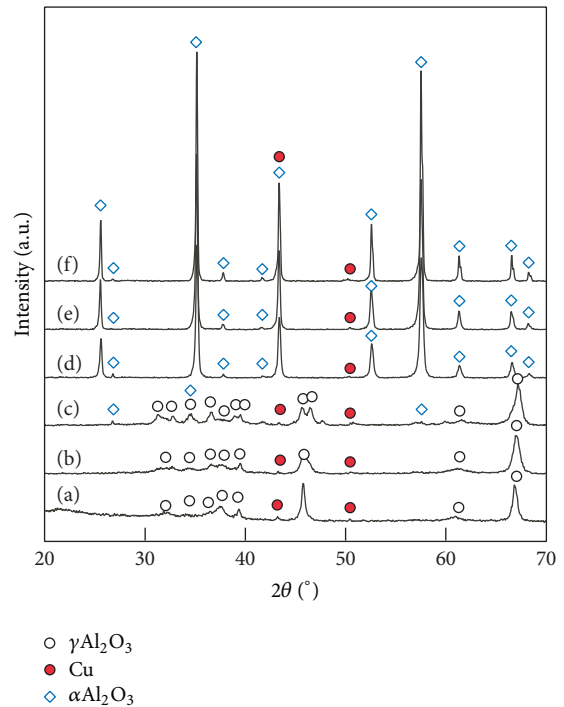


FIGURE 3: XRD patterns of Al_2O_3 -Cu at $C_{\text{Cu}} = 5.2$ mass% by spark plasma sintering at $T_{\text{SPS}} =$ (a) 1073, (b) 1173, (c) 1273, (d) 1373, (e) 1473, and (f) 1573 K.

In our present work, however, the maximum relative density was only 98.4% at $T_{\text{SPS}} = 1473$ K using the $\gamma\text{Al}_2\text{O}_3$ of 80 nm in grain size, lower than Hotta's result using the $\alpha\text{Al}_2\text{O}_3$ starting powder at the same sintering temperature. This could be attributed to the phase transformation of $\gamma\text{Al}_2\text{O}_3$ to $\alpha\text{Al}_2\text{O}_3$ in the present sintering process, which retarded the densification process slightly. At $T_{\text{SPS}} = 1473$ K, the relative density of Al_2O_3 -Cu increased with increasing C_{Cu} and

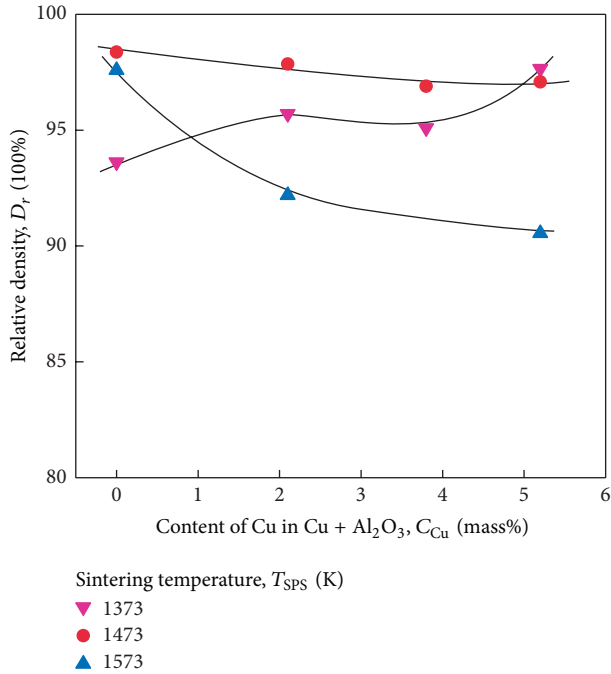


FIGURE 4: The effect of Cu content on the relative density of Al_2O_3 -Cu composites at $T_{SPS} = 1373, 1473,$ and 1573 K, respectively.

the maximum value was 97.7% at $C_{Cu} = 5.2$ mass%. But at $T_{SPS} = 1373$ and 1573 K, the relative density of C_{Cu} decreased with increasing C_{Cu} . At $T_{SPS} = 1573$ K and $C_{Cu} = 5.2$ mass%, the relative density was only 90.6%, about 7% lower than that of monolithic Al_2O_3 at the same sintering temperature. The decrease of the relative density at $T_{SPS} = 1573$ K was explained from the microstructural observation of Figure 5.

Figure 5 shows SEM images of the fracture surface of Al_2O_3 and Al_2O_3 -Cu sintered at $T_{SPS} = 1373$ to 1573 K. At $T_{SPS} = 1373$ K, some pores were observed in Al_2O_3 fracture surfaces. In contrast, almost no pores were identified in Al_2O_3 -Cu at the same sintering temperature, indicating Cu nanoparticles improved the densification of Al_2O_3 . Adding a small amount of nanoparticles could usually inhibit the grain growth of Al_2O_3 . For example, Ji and Yeomans found that 5 vol% Cr apparently decreased the grain growth of Al_2O_3 hot pressed at 1723 K and thus increased the strength and fracture toughness of Al_2O_3 [6]. Zhang et al. also found that Ni could decrease the grain growth of Al_2O_3 [21]. In the present study, however, although the grain size of Al_2O_3 was not apparently inhibited, the relative density was increased due to the decrease of the pores. The reason might be that the Cu was in situ coated on the surface of $\gamma-Al_2O_3$ (80 nm in grain size) instead of ball-mill mixing. At $T_{SPS} = 1473$ and 1573 K, the pores were both observed in Al_2O_3 and Al_2O_3 -Cu. By incorporating pores among grains, the grain size increase of Al_2O_3 -Cu at $T_{SPS} = 1573$ K induced the lower relative density as shown in Figure 4. On the other hand, at 1373 K, the nanocomposite is less porous than monolithic Al_2O_3 , due to the filling of the Cu nanoparticles in the pores of bulk Al_2O_3 . However, the opposite is true at $T_{SPS} = 1573$ K as Cu

might retard the diffusion of the densification process at a high temperature.

Figure 6 shows the effect of C_{Cu} on the Vickers' hardness and fracture toughness at a load of 19.6 N. The maximum hardness was 20.7 ± 1.4 GPa at 2.1 mass% Cu, whereas the maximum fracture toughness was 4.1 ± 0.3 $MPa m^{1/2}$ at $C_{Cu} = 3.8$ mass%. Compared to those values of 19.8 GPa and 3.1 $MPa m^{1/2}$ of the monolithic Al_2O_3 , the hardness and fracture toughness of Al_2O_3 -Cu nanocomposites were about 4% and 32% higher at 3.8 mass%, respectively. The reason that the hardness and toughness were achieved at different compositions is that the concentration of Cu determined these two quantities differently. The Cu nanoparticle would like to fill the pores of Al_2O_3 and thus increased the relative density and the hardness of Al_2O_3 . But the fracture toughness was increased mainly by crack deflecting and bridging. Thus the maximum hardness and toughness were achieved at different compositions as shown in Figure 6.

The incorporation of second particle phases, such as Cu, Cr, and Ni, would often induce the crack deflection and bridging by absorbing the energy and thus increase the fracture toughness related to the indentation crack length [6, 7, 22]. In the present study, the optimum C_{Cu} was 3.8 mass%, with which the crack length is the lowest and then the fracture toughness was calculated to be the largest value according to the method as described in the experimental part [19]. On the other hand, the Al_2O_3 -Cu nanocomposites in [7] has a fracture toughness of 4.5 $MPa m^{1/2}$ and 0.4 $MPa m^{1/2}$ higher than the value in the present study, but the hardness of the nanocomposites was not mentioned [7]. The higher value of the fracture toughness of the nanocomposite in [7] might be due to its lower hardness and the different testing techniques. When the C_{Cu} was higher than 4 mass%, the fracture toughness and hardness of Al_2O_3 -Cu nanocomposites both decreased, which might be due to the agglomeration of Cu nanoparticles at a higher content.

Figure 7 shows a comparison of the hardness and fracture toughness with Al_2O_3 -based nanocomposites in literature mixed by various methods, typically ball milling. The hardness of Al_2O_3 body, Al_2O_3 -Nb, and Al_2O_3 -Nb-CNTs composites ranged from 16 to 22 GPa, with the low fracture toughness of 2.8–3.6 $MPa m^{1/2}$ [6, 23]. The incorporation of soft phases, such as Ti_3SiC_2 , would increase the fracture toughness of Al_2O_3 body with a decrease of hardness [24, 25]. Yao et al. incorporated Ni to increase the fracture toughness of Al_2O_3 to 4.3 $MPa m^{1/2}$, while the hardness was 14.2 GPa [26]. It is common that the higher hardness, the lower fracture toughness. The reported values ranged in the hatched area in Figure 7. In the present study, the fracture toughness increased to 4.1 $MPa m^{1/2}$, about 40% higher than that of Al_2O_3 body with the hardness of 20.4 GPa, higher than most of reported values for the Al_2O_3 body and many Al_2O_3 -based composites in literature.

4. Conclusions

Cu nanoparticles were precipitated on $\gamma-Al_2O_3$ by rotary chemical vapor deposition at $T_{SPS} = 673$ to 873 K for 30 min,

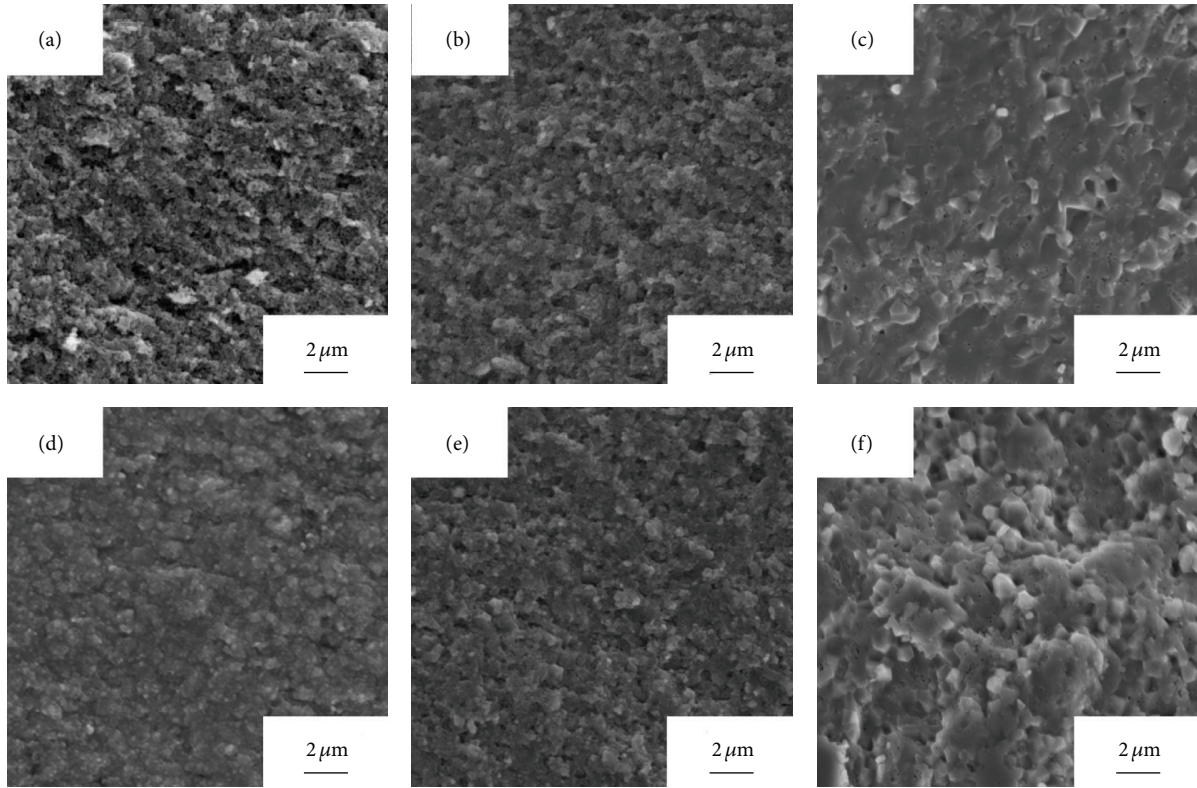


FIGURE 5: SEM fracture surface images of Al_2O_3 sintered at T_{SPS} = (a) 1373 K, (b) 1473 K, and (c) 1573 K and Al_2O_3 -Cu sintered at T_{SPS} = (d) 1373 K, (e) 1473 K, and (f) 1573 K.

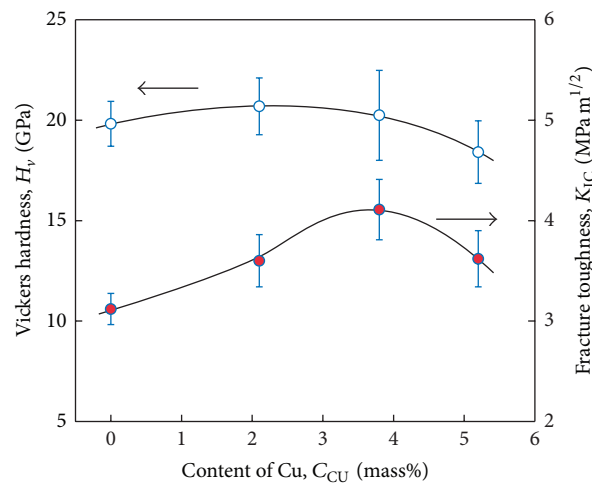


FIGURE 6: The dependence of Vickers hardness and fracture toughness on the mass content of Cu.

and then the as-obtained composite powders were consolidated by spark plasma sintering to get bulk Al_2O_3 -Cu nanocomposites. Although the grain size and C_{Cu} increased with increasing precipitation temperature from $T_{\text{SPS}} = 673$ to 873 K, they were still in the range of nanocomposite powders. The incorporation of Cu enhanced the densification of Al_2O_3 body by SPS at $T_{\text{SPS}} = 1473$ K. The sintered Al_2O_3 -Cu nanocomposites with a fine microstructure showed the maximum hardness and fracture toughness of 20.7 ± 1.4 GPa

at $C_{\text{Cu}} = 2.1$ mass% and 4.1 ± 0.3 $\text{MPa m}^{1/2}$ at $C_{\text{Cu}} = 3.8$ mass%, respectively. Therefore, the treatment of rotary CVD and spark plasma sintering could be a promising route to obtain high performance ceramic-based nanocomposites.

Conflict of Interests

The authors declare that there is no conflict of interests regarding the publication of this paper.

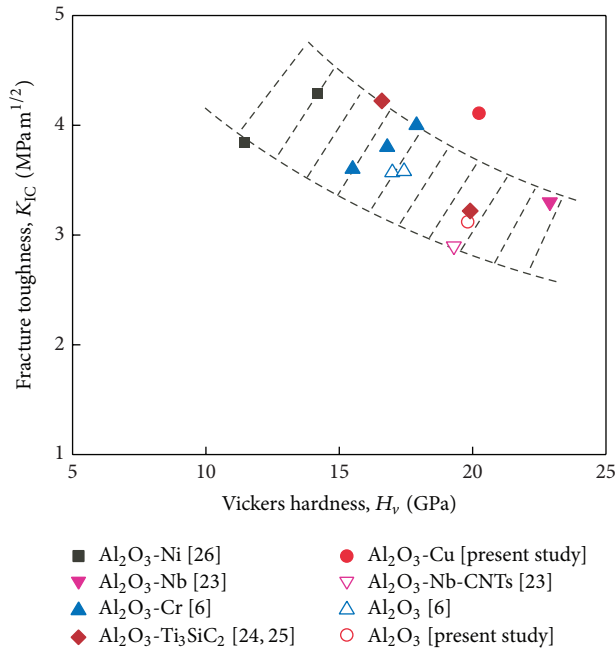


FIGURE 7: Comparison of microhardness and fracture toughness of Al_2O_3 -3.8 mass% Cu nanocomposite with those of the Al_2O_3 -based composites reported in literature.

Acknowledgments

The authors appreciate the financial supports from the Fundamental Research Funds for the Central Universities (2013B34414), and the National 973 Plan Project (2015CB057803).

References

- [1] E. Rocha-Rangel and J. G. Miranda-Hernández, "Alumina-copper composites with high fracture toughness and low electrical resistance," *Materials Science Forum*, vol. 644, pp. 43–46, 2010.
- [2] G. J. Li, X. X. Huang, and J. K. Guo, "Fabrication, microstructure and mechanical properties of $\text{Al}_2\text{O}_3/\text{Ni}$ nanocomposites by a chemical method," *Materials Research Bulletin*, vol. 38, no. 11-12, pp. 1591–1600, 2003.
- [3] T. Isobe, K. Daimon, T. Sato, T. Matsubara, Y. Hikichi, and T. Ota, "Spark plasma sintering technique for reaction sintering of $\text{Al}_2\text{O}_3/\text{Ni}$ nanocomposite and its mechanical properties," *Ceramics International*, vol. 34, no. 1, pp. 213–217, 2008.
- [4] Q. Yan, G. Y. Wang, Z. Huang, and D. Jiang, "A microstructure study of $\text{Ni}/\text{Al}_2\text{O}_3$ composite ceramics," *Journal of Alloys and Compounds*, vol. 467, no. 1-2, pp. 438–443, 2009.
- [5] T. Rodriguez-Suarez, L. A. Diaz, R. Torrecillas et al., "Alumina/tungsten nanocomposites obtained by spark plasma sintering," *Composites Science and Technology*, vol. 69, no. 14, pp. 2467–2473, 2009.
- [6] Y. Ji and J. A. Yeomans, "Processing and mechanical properties of Al_2O_3 -5 vol.% Cr nanocomposites," *Journal of the European Ceramic Society*, vol. 22, no. 12, pp. 1927–1936, 2002.
- [7] Y. D. Kim, S.-T. Oh, K. H. Min, H. Jeon, and I.-H. Moon, "Synthesis of Cu dispersed Al_2O_3 nanocomposites by high energy ball milling and pulse electric current sintering," *Scripta Materialia*, vol. 44, no. 2, pp. 293–297, 2001.
- [8] S.-T. Oh and S.-J. Yoon, "Hydrogen reduction and sintering behavior of $\text{Al}_2\text{O}_3/\text{CuO}$ powder mixtures prepared from different raw powders," in *Science of Engineering Ceramics III*, pp. 181–184, 2006.
- [9] P. K. Jena, E. A. Brocchi, I. G. Solórzano, and M. S. Motta, "Identification of a third phase in $\text{Cu-Al}_2\text{O}_3$ nanocomposites prepared by chemical routes," *Materials Science and Engineering A*, vol. 371, no. 1-2, pp. 72–78, 2004.
- [10] C. Vahlas, B. Caussat, P. Serp, and G. N. Angelopoulos, "Principles and applications of CVD powder technology," *Materials Science and Engineering R: Reports*, vol. 53, no. 1-2, pp. 1–72, 2006.
- [11] D. Geldart, "Types of gas fluidization," *Powder Technology*, vol. 7, no. 5, pp. 285–292, 1973.
- [12] S. Morooka, K. Kusakabe, A. Kobata, and Y. Kato, "Fluidization state of ultrafine powders," *Journal of Chemical Engineering of Japan*, vol. 21, no. 1, pp. 41–46, 1988.
- [13] J. Zhang, R. Tu, and T. Goto, "Preparation of Ni-precipitated hBN powder by rotary chemical vapor deposition and its consolidation by spark plasma sintering," *Journal of Alloys and Compounds*, vol. 502, no. 2, pp. 371–375, 2010.
- [14] J. Zhang, R. Tu, and T. Goto, "Spark plasma sintering of Al_2O_3 -cBN composites facilitated by Ni nanoparticle precipitation on cBN powder by rotary chemical vapor deposition," *Journal of the European Ceramic Society*, vol. 31, no. 12, pp. 2083–2087, 2011.
- [15] S. Brunauer, P. H. Emmett, and E. Teller, "Adsorption of gases in multimolecular layers," *Journal of the American Chemical Society*, vol. 60, no. 2, pp. 309–319, 1938.
- [16] Al_2O_3 , JCPDS, International Centre for Diffraction Data, No. 10-173.
- [17] Cu, JCPDS, International Centre for Diffraction Data, No. 65-9743.
- [18] J. Zhang, R. Tu, and T. Goto, "Densification, microstructure and mechanical properties of SiO_2 -cBN composites by spark plasma sintering," *Ceramics International*, vol. 38, no. 1, pp. 351–356, 2012.
- [19] B. R. Lawn and E. R. Fuller, "Equilibrium penny-like cracks in indentation fracture," *Journal of Materials Science*, vol. 10, no. 12, pp. 2016–2024, 1975.
- [20] M. Hotta and T. Goto, "Densification and microstructure of Al_2O_3 -cBN composites prepared by spark plasma sintering," *Journal of the Ceramic Society of Japan*, vol. 116, no. 1354, pp. 744–748, 2008.
- [21] J. Zhang, R. Tu, and T. Goto, "Spark plasma sintering of Al_2O_3 -Ni nanocomposites using Ni nanoparticles produced by rotary chemical vapour deposition," *Journal of the European Ceramic Society*, vol. 34, no. 2, pp. 435–441, 2014.
- [22] J. Lu, L. Gao, J. Sun, L. Gui, and J. Guo, "Effect of nickel content on the sintering behavior, mechanical and dielectric properties of $\text{Al}_2\text{O}_3/\text{Ni}$ composites from coated powders," *Materials Science and Engineering A*, vol. 293, no. 1-2, pp. 223–228, 2000.
- [23] K. E. Thomson, D. Jiang, J. A. Lemberg, K. J. Koester, R. O. Ritchie, and A. K. Mukherjee, "In situ bend testing of niobium-reinforced alumina nanocomposites with and without single-walled carbon nanotubes," *Materials Science and Engineering A: Structural Materials Properties Microstructure and Processing*, vol. 493, no. 1-2, pp. 256–260, 2008.
- [24] L. YongMing, L. ShuQin, C. Jian, W. RuiGang, L. JianQiang, and P. Wei, "Preparation and characterization of $\text{Al}_2\text{O}_3\text{-Ti}_3\text{SiC}_2$

composites and its functionally graded materials,” *Materials Research Bulletin*, vol. 38, no. 1, pp. 69–78, 2003.

- [25] Y. M. Luo, S. Q. Li, J. Chen, R. G. Wang, J. Q. Li, and W. Pan, “Effect of composition on properties of alumina/titanium silicon carbide composites,” *Journal of the American Ceramic Society*, vol. 85, no. 12, pp. 3099–3101, 2002.
- [26] X. Yao, Z. Huang, L. Chen et al., “Alumina-nickel composites densified by spark plasma sintering,” *Materials Letters*, vol. 59, no. 18, pp. 2314–2318, 2005.

Research Article

Molecular Dynamics Study on the Effect of Temperature on the Tensile Properties of Single-Walled Carbon Nanotubes with a Ni-Coating

Fulong Zhu,¹ Hengyou Liao,² Kai Tang,¹ Youkai Chen,¹ and Sheng Liu¹

¹*Institute of Microsystems, School of Mechanical Science and Engineering, Huazhong University of Science and Technology, 1037 Luoyu Road, Wuhan, Hubei 430074, China*

²*Dongfang Electric Machinery Co., Ltd, Deyang, Sichuan 618000, China*

Correspondence should be addressed to Fulong Zhu; zhufulong@hust.edu.cn

Received 16 September 2014; Accepted 18 January 2015

Academic Editor: Cheng Yan

Copyright © 2015 Fulong Zhu et al. This is an open access article distributed under the Creative Commons Attribution License, which permits unrestricted use, distribution, and reproduction in any medium, provided the original work is properly cited.

The effect of temperature on the tensile behavior of the armchair (6, 6) single-walled carbon nanotubes with a Ni-coating (SWCNT-Ni) was investigated using molecular dynamics (MD) methods. The mechanical properties of SWCNT-Ni and SWCNT were calculated and analyzed at different temperatures in the range from 220 K to 1200 K. From the MD results, temperature was determined to be the crucial factor affecting the mechanical properties of SWCNT-Ni and SWCNT. After coating nickel atoms onto the surface of a SWCNT, the Young's modulus, tensile strength, and tensile failure strain of SWCNT were greatly reduced with temperature rising, indicating that the nickel atoms on the surface of SWCNT degrade its mechanical properties. However, at high temperature, the Young's modulus of both the SWCNT and the SWCNT-Ni exhibited significantly greater temperature sensitivity than at low temperatures, as the mechanical properties of SWCNT-Ni were primarily dominated by temperature and C-Ni interactions. During these stretching processes at different temperatures, the nickel atoms on the surface of SWCNT-Ni could obtain the amount of energy sufficient to break the C-C bonds as the temperature increases.

1. Introduction

Since discovery in 1991 [1] and due to the excellent properties such as high thermal and electrical conductivity, ultra mechanical strength, low density, and high aspect ratio, carbon nanotubes (CNTs) have gained increasing attention from both academia and industry. The thermal conductivity of multiwalled carbon nanotubes (MWCNT) can reach up to 3000 W/mK [2], and the thermal conductivity of single-walled nanotubes (SWCNT) can be even higher [3]. Some types of CNTs are considered to be ideal candidates as reinforcing materials to enhance the properties of composites and electrical and thermal devices [4, 5].

Because of the remarkable mechanical properties of SWCNT, it is believed that the mechanical properties of a metal matrix can be greatly improved by mixing the metal with SWCNT coated by a metal film, such as nickel or copper. For some types of metals, during mixing, the metal could

agglomerate into discrete deposits on SWCNT bundles [6, 7], which could decrease the adhesive force between SWCNT and the metal matrix, thus preventing the improvement of the mechanical properties of the metal by mixing the metal with SWCNTs. To increase the adhesive force between SWCNT and some metal atoms, the surface of each SWCNT must be treated by coating some metal films, such as nickel or copper. After coating certain metal films onto the surfaces of SWCNTs, the SWCNTs with a coating of metal film are suitable to mix with the metal matrix, thereby improving the efficiency of load transfer from the metal matrix to the carbon nanotubes. Coating nickel or copper is one conventional method of decorating the surface of SWCNT. Nickel atoms can be coated onto suspended single-walled carbon nanotubes using electron-beam evaporation, as the coating of nickel atoms on the suspended carbon tubes has been demonstrated to be continuous and quasi-continuous [6]. Some metals were also deposited onto a vertically aligned

SWCNT (VA-SWCNT) film by evaporative deposition [7]; and the continuous spreading of nickel atoms onto carbon nanotubes was investigated using molecular dynamics methods [8]. Some experiments also indicated that the mechanical and tribological properties of the copper matrix composites could be significantly enhanced by the incorporation of SWCNT reinforcements after coating SWCNT with nickel metal [9]. Meanwhile, the decorated CNTs could also be functionalized to satisfy interconnecting processing or for the application of nanoscale sensors [10].

To determine the effect of temperature on the mechanical properties of armchair (6, 6) single-walled carbon nanotubes with a Ni-coating (SWCNT-Ni), a perfect SWCNT decorated with a coating of nickel atoms on its surfaces is considered in this work. Although the influence of nickel atoms on SWCNT was investigated at 0 K and 300 K [11], a wide temperature range will be defined in this paper by considering temperatures of 220 K, 300 K, 500 K, 700 K, 1000 K, and 1200 K. After modeling and analyzing the stretching process of SWCNT and SWCNT-Ni at different temperatures of 220 K, 300 K, 500 K, 700 K, 1000 K, and 1200 K using molecular dynamics methods, the mechanical behaviors of the SWCNT and the SWCNT-Ni can then be determined. In the following molecular dynamics simulation for stretching SWCNT and SWCNT-Ni, a more complicated second-generation Brenner reactive empirical bond-order potential will be introduced for analyzing the behaviors of SWCNT-Ni and SWCNT. In the following section, the stress-strain curves of SWCNT and SWCNT-Ni are determined with the data from these molecular dynamics computational results, their fracture surfaces are also determined, and the influence of temperature on the coating of nickel onto the surface of SWCNT is revealed.

2. Computational Methods and Models

To investigate the effect of nickel atoms and temperature on the mechanical behavior of SWCNT-Ni, the surface of an armchair (6, 6) SWCNT was coated with nickel using metal cluster deposition [8]. After coating nickel atoms onto the surface of SWCNT, nickel clusters were demonstrated to spread and form a continuous smooth surface of a VA-SWCNT, in which the equilibrium position for nickel atoms was the center of the hexagons of the carbon atoms of SWCNT [12]. In this work, molecular dynamics simulations of the stretching process at different temperatures for SWCNT-Ni and SWCNT were performed, based on the large-scale atomic/molecular massively parallel simulator (LAMMPS) code [13]. In the molecular dynamics (MD) modeling of SWCNT and SWCNT-Ni, to simplify the cluster deposition process, nickel atoms were simply placed in the vicinity of the center of a carbon hexagon, with every computing step of the molecular dynamics simulation following a period of energy minimization; MD simulations for the stretching process of SWCNT-Ni and SWCNT were conducted at different temperatures of 220 K, 300 K, 500 K, 700 K, 1000 K, and 1200 K, and Figures 1 and 2 show the stretching models. In the stretching diagrams of Figures 1 and 2, the molecular model of the armchair (6, 6) SWCNT consisted of 576 carbon atoms, and the molecular model of

the armchair (6, 6) SWCNT-Ni had 576 carbon atoms and 264 nickel atoms. In the two models shown in Figures 1 and 2, the first two rings of atoms located at each model's right end were fixed, the last two rings of atoms located at the left end were also restricted in their x - and y -directions, and the stretching process occurred along the z -direction. In the MD simulations for SWCNT and SWCNT-Ni, the entire stretching process occurred in an isothermal environment; the C-C interactions were modeled using the second-generation Brenner reactive empirical bond-order potential [14], which has been successfully used to investigate various carbon and hydrocarbon systems; the C-Ni and Ni-Ni interaction parameters were also determined using the Brenner-type potential, and its potential parameters were used from these results [14]. This type of potential could be described by the following formulae:

$$\begin{aligned}
 E_{ij}^{C-Ni} &= \frac{D_e}{S-1} \exp \left\{ -\beta\sqrt{2S} (r_{ij} - R_e) \right\} \\
 &\quad - B^* \frac{D_e S}{S-1} \exp \left\{ -\beta\sqrt{2/S} (r_{ij} - R_e) \right\}, \\
 B^* &= \left\{ 1 + b (N^C - 1) \right\}^\delta, \\
 E_{ij}^{Ni-Ni} &= \frac{D_e}{S-1} \exp \left\{ -\beta\sqrt{2S} (r_{ij} - R_e) \right\}, \\
 &\quad - \frac{D_e S}{S-1} \exp \left\{ -\beta\sqrt{2/S} (r_{ij} - R_e) \right\}, \quad (1) \\
 D_e &= D_{e1} + D_{e2} \exp \left\{ -C_D (N^M - 1) \right\}, \\
 R_e &= R_{e1} - R_{e2} \exp \left\{ -C_R (N^M - 1) \right\}, \\
 N_i^C &= 1 + \sum_{\text{carbon}} f(r_{ik}), \\
 N_i^M &= 1 + \sum_{\text{metal}} f(r_{ik}).
 \end{aligned}$$

Here, r_{ij} was the distance between the two atoms i and j . D_e and R_e were the binding energy and equilibrium bond length, respectively. S , β , b , and δ determined the shape of the potential functions. For the C-Ni interactions, the many-body effects were defined by using an additional term B^* , which was expressed as a function of the carbon coordination number of a metal atom N^C . For the Ni-Ni interactions, the binding energy D_e and the equilibrium bond length R_e were expressed as direct functions of the metal coordination number N^M . Consider

$$f(r_{ij}) = \begin{cases} 1 & r < R_1, \\ \frac{1}{2} \left[1 + \cos \frac{\pi(r_{ij} - R_1)}{R_2 - R_1} \right] & R_1 \leq r \leq R_2, \\ 0 & r > R_2. \end{cases} \quad (2)$$

The cutoff function equation in the second-generation Brenner reactive empirical bond-order potential introduced a dramatic increase in the interatomic force at $r = R_1$ (similar to a camelback on the force curve) [15], which could rise

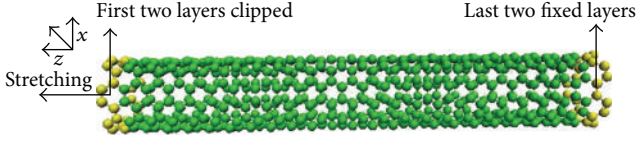


FIGURE 1: Stretching model diagram of a SWCNT.

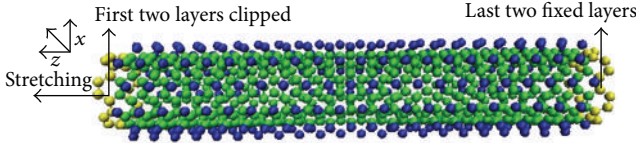


FIGURE 2: Stretching model diagram of a SWCNT-Ni.

sharply with a peak near the bond breaking length. Therefore, $R_1 = R_2 = 2.0 \text{ \AA}$ [16] was used to avoid overestimating the force in the molecular dynamics simulation of this paper.

In this work, the structure of SWCNT-Ni was two concentric cylinders, and the cross-sectional of SWCNT-Ni was two concentric circles; the cross-sectional area of SWCNT-Ni was defined by the area between SWCNT and nickel layer, and the thickness of SWCNT-Ni was the distance between SWCNT and nickel layer. The distance between SWCNT and nickel layer was 1.5 \AA and the diameter of (6, 6) SWCNT was 8.14 \AA . So the cross-sectional area of SWCNT-Ni was defined as $93.74 \text{ \AA} \times \text{ \AA}$. In the atomistic simulation, the stress of σ_{mn} on the m and n directions is given by the following formula [17]:

$$\sigma_{mn} = \frac{1}{N_S} \sum_i \left[\frac{m_i v_i^m v_i^n}{V_i} - \frac{1}{2V_i} \sum_j \frac{\partial U(r_{ij})}{\partial r_{ij}} \frac{r_{ij}^m r_{ij}^n}{r_{ij}} \right], \quad (3)$$

where N_S is the number of particles contained in the region S , and S is defined as the region of atomic interaction, v_i is the velocity of the particle i , and r_{ij}^m and r_{ij}^n are two components of the vector from the atoms i to j . V_i is the volume assigned to atom i .

For each atomic model from this work, the constant pressure and constant temperature (NPT) integration was performed using a Nose/Hoover temperature thermostat and a Nose/Hoover pressure barostat, and the bulk pressure was defined as zero. Subsequently, under the conditions of constant volume and constant temperature (NVT), these models were equilibrated to the desired temperatures using a Nose/Hoover temperature thermostat. The velocity Verlet method was used to integrate the classical equations of motion with a time step of 0.5 fs .

During the entire stretching process shown in Figures 1 and 2, the 47th and 48th rings of carbon atoms at the right end of both models were fixed, the first and second rings of carbon atoms at the left end were also restricted in their x - and y -directions, and the models of SWCNT and SWCNT-Ni were gradually stretched along the z -direction; the tensile load was applied along the z -direction. After every step of stretching, it was necessary that the simulation system provide sufficient time for the model to relax. In the modeling of the stretching

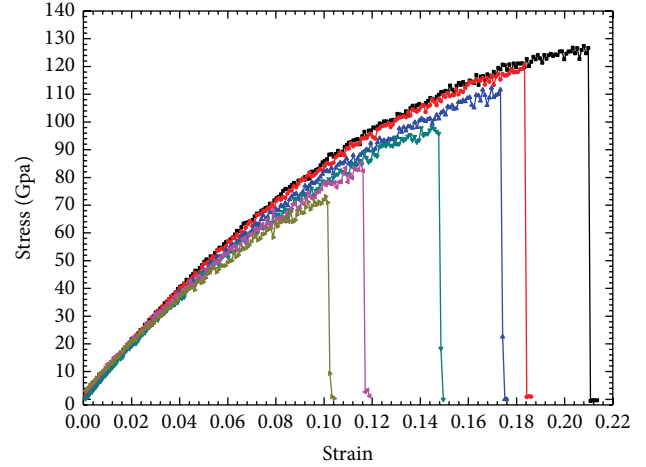


FIGURE 3: Stress-strain curves of SWCNT at different temperatures.

process, the relaxation time was defined to be 10 ps . The external applied force was obtained by summing the internal forces acting on the atoms of the stretching section. All the data used to evaluate the mechanical properties of SWCNT and SWCNT-Ni was extracted from the back 1000 steps after the relaxation time of every instance of stretching. Considering unintentional sudden variations, the average of 10 sets of data at an interval of 100 steps during the above 1000 steps was used to determine the mechanical properties of SWCNT and SWCNT-Ni.

3. Results and Discussions

After the MD computations of the stretching process for SWCNT and SWCNT-Ni at the different temperatures of 220 K , 300 K , 500 K , 700 K , 1000 K , and 1200 K , the internal forces acting on the atoms and the stretching distance were obtained, which could be transformed into the corresponding stress and strain values. Due to the difficulty of defining the thickness of SWCNT-Ni, the definition of stress in the stretching process was from the atomistic stress of the MD modeling [17]. Figures 3 and 4 show all the simulated stress-strain curves over the prescribed temperature range for SWCNT and SWCNT-Ni, which clearly indicates that temperature was the crucial factor that determines the diversity of the stress-strain curves. From the curves in Figure 4, the stress-strain curves of SWCNT-Ni over the temperature range underwent some phase of linear elastic deformation, nonlinear elastic deformation, yield deformation, strengthening, and rupture, for which the length of any phase exhibited the temperature effect. Compared with SWCNT-Ni's stress-strain curves in Figure 4, SWCNT's stress-strain curves in Figure 3 were different. During the stretching process over all the prescribed temperatures, the stress-strain curves of the SWCNT did not exhibit any yielding phase. Unlike SWCNT's stress-strain curves, the stress-strain curve of the

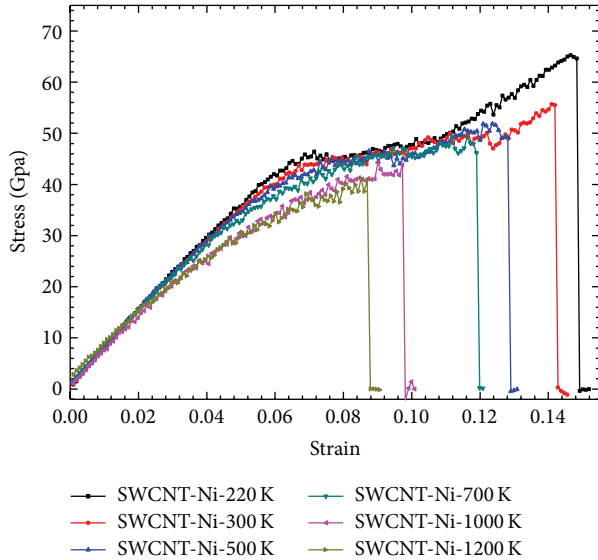


FIGURE 4: Stress-strain curves of SWCNT-Ni at different temperatures.

SWCNT-Ni at 220 K clearly exhibited a yielding section after elastic deformation in Figure 4, which was also found in the other curves of SWCNT-Ni. In Figure 4, SWCNT-Ni's stress-strain curves were different from those of SWCNT, which revealed that the nickel atoms coated onto the surface of SWCNT play an important role in affecting the mechanical behavior of SWCNT-Ni. In SWCNT-Ni's stretching process at different temperatures, nickel atoms' rearrangement can occur, which would change some mechanical properties of SWCNT-Ni. The strain-stress curve of the armchair (5, 5) carbon nanotubes with nickel-coating exhibited a flat phase at the beginning of the stretching at 300 K [11]; this phenomenon did not occur in the stress-strain curves shown in Figure 4, which might be due to the use of a different initial equilibrium method and the change of the cutoff function. In this work, NPT integration was performed using a Nose/Hoover temperature thermostat and Nose/Hoover pressure barostat, the bulk pressure was defined as zero, and the internal stress could be released fully.

According to the force and deformation data from the MD computations for the stretching at different temperatures, the various curves, such as the failure force and temperature, the failure stress and temperature, the failure strain and temperature, and Young's modulus and temperature, could be analyzed, thus enabling the mechanical properties of SWCNT and SWCNT-Ni to be determined at the different temperatures. Figures 5, 6, 7, and 8 show the failure force, failure stress, failure strain, and Young's modulus, respectively, at temperatures of 220 K, 300 K, 500 K, 700 K, 1000 K, and 1200 K. In the failure force and temperature curves in Figure 5, the failure force of SWCNT and SWCNT-Ni decreases as the temperature increases. In the same way, this tendency of decreasing as the temperature increases was observed in the curves of failure stress, failure strain, and Young's modulus in Figures 6, 7, and 8, respectively.

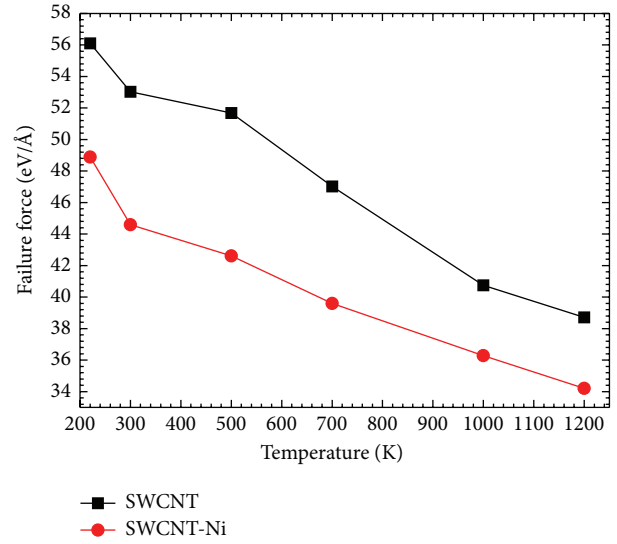


FIGURE 5: Failure force versus temperature curves of SWCNT and SWCNT-Ni.

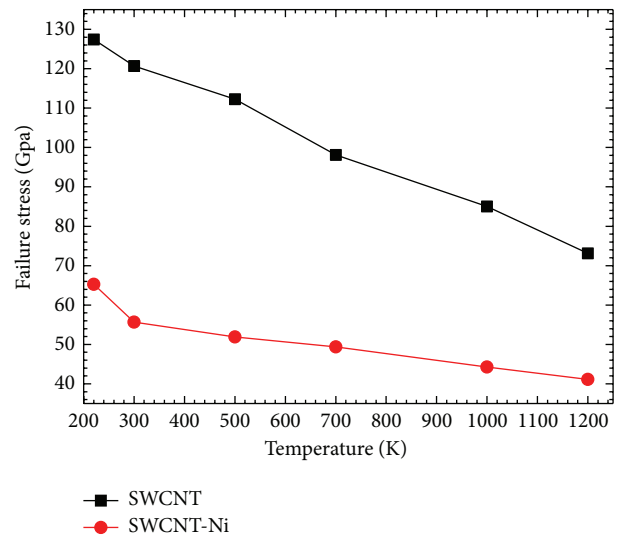


FIGURE 6: Failure stress versus temperature curves of SWCNT and SWCNT-Ni.

As shown in Figure 6, the failure stress of SWCNT decreases more rapidly than that of SWCNT-Ni as the temperature increases. In the MD computation in this work, the attenuation distance R_1 of the cutoff function increased and the failure stress of SWCNT was still higher than the experimental values that range from 11 GPa to 63 GPa at room temperature [18], which resulted from the perfect SWCNT used in the molecular dynamics modeling in this work. At the same time, the failure stress at different temperatures in Figure 6 was still larger than that of the modeling for a (5, 5) pristine SWCNT using a modified Tersoff-Brenner potential [19], which could be caused by differences in the SWCNT modeled. In Figure 6, the failure stress of SWCNT-Ni was nearly half that of SWCNT over the same temperature

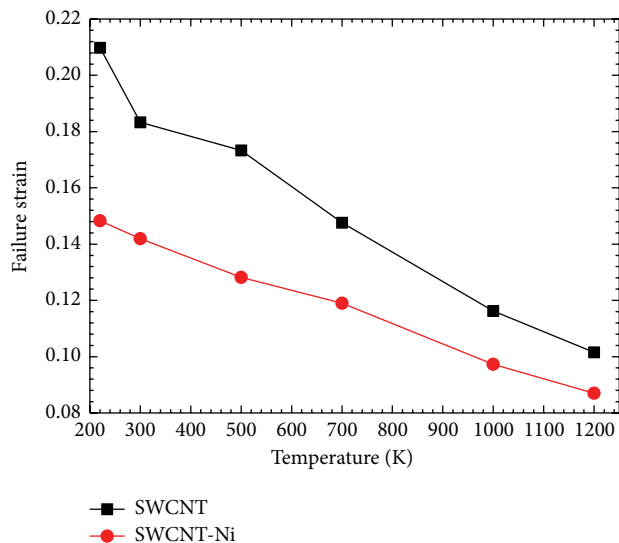


FIGURE 7: Failure strain versus temperature curves of SWCNT and SWCNT-Ni.

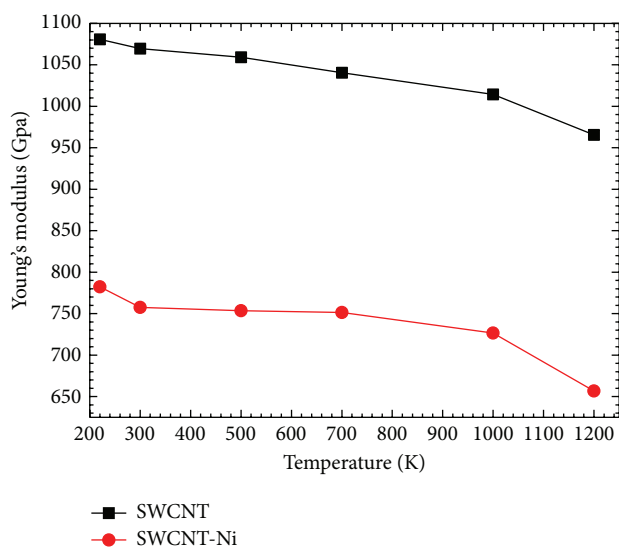


FIGURE 8: Young's modulus versus temperature curves of SWCNT and SWCNT-Ni.

range, which was also found in a previous study [11], and it could be attributed partly to the increase of the cross-sectional diameter and the decrease of the failure force of the SWCNT-Ni. Compared with SWCNT, the nickel atoms on the surface of SWCNT-Ni could weaken the strength of SWCNT. When being stretched, the six-member ring of SWCNT-Ni suffered local distortion, the C-C bond length became longer along the z -axis (tensile direction), and the C-C interaction became equal to the C-Ni interaction, which enabled thermal fluctuation to be a key factor for determining the rupture of SWCNT-Ni. In this work, the MD simulation of SWCNT-Ni was different from those using the pristine Brenner potential and the dissimilar attenuation distance [11].

For the failure strains shown in Figure 7, the failure strain of SWCNT was still larger than the experimental results of 10–13% failure strain [18] and 25% smaller than those results [20]. Figure 7 clearly shows that the failure strain of SWCNT and SWCNT-Ni would decrease almost linearly with temperature, thus indicating that the effect of temperature is dominant when the temperature increases. During the stretching processes, carbon atoms could prefer to exhibit a sp^2 structure and tend to maintain this structure at the Brenner potential [21]. For the stretching of SWCNT-Ni, once a particular C-C bond is broken, the nearby nickel atoms would terminate the dangling bonds of the carbon atoms and form bonds with each other [11]. Unlike the failure stress and failure strain shown in Figures 6 and 7, Young's modulus of SWCNT and SWCNT-Ni was not severely sensitive to temperature. In Figure 8, the variation of Young's modulus of SWCNT was approximately 6% from 220 K to 1000 K, which was consistent with the results of [22]; however, when the temperature increased to 1200 K, Young's modulus of SWCNT decreased by approximately 10.6%. In Figure 8, all Young's modulus values of SWCNT at temperatures from 220 K to 1200 K were larger than the results of [11]. However, compared to those simulations using the Brenner potential function [22] and the modified Morse potential function [15, 23], in this work, Young's modulus of SWCNT was in the range of the computed and experimental values of [18]. After coating nickel onto the surface of SWCNT, Young's modulus of SWCNT-Ni decreased over the temperature range from 220 to 1200 K by approximately 27.6%. Apparently, the sectional diameter of SWCNT-Ni was larger than that of SWCNT, and the C-Ni interactions decreased the C-C bond strength, thereby affecting the mechanical behavior of SWCNT-Ni.

When SWCNT or SWCNT-Ni was stretched to some extent, rupturing failure was inevitable. As shown in Figure 9, all the final rupture surfaces at different temperatures were found to be completely brittle, in agreement with the past report [15]. From the stretching rupture surfaces shown in Figure 9, the rupture surfaces of SWCNT-Ni at different temperatures were completely separated, while the rupture surfaces of SWCNT were slightly connected by a single chain of carbon atoms after breaking failure; similar rupture surfaces were also noted in the past [24]. During the stretching simulation for SWCNT and SWCNT-Ni, when breakage of the C-C bonds occurred, a significant amount of elastic potential energy was released. As the temperature increased, nickel atoms would obtain enough energy to overcome the energy barrier, thereby breaking the nearby C-C bonds, followed by the occurrence of rupture, with the rupture surfaces 45° from the z -direction, as shown Figure 9.

In the MD simulations of stretching SWCNT and SWCNT-Ni at different temperature ranging from 220 to 1200 K, the initial working length, that is, the initial equilibrium total length minus the length of the fixed layer of carbon atoms, could also indicate the effect of temperature on thermal expansion behaviors. The initial working lengths of SWCNT and SWCNT-Ni shown in Figure 10 indicated that the working length of SWCNT-Ni was longer than that of SWCNT at the same temperature, the equilibrium bond

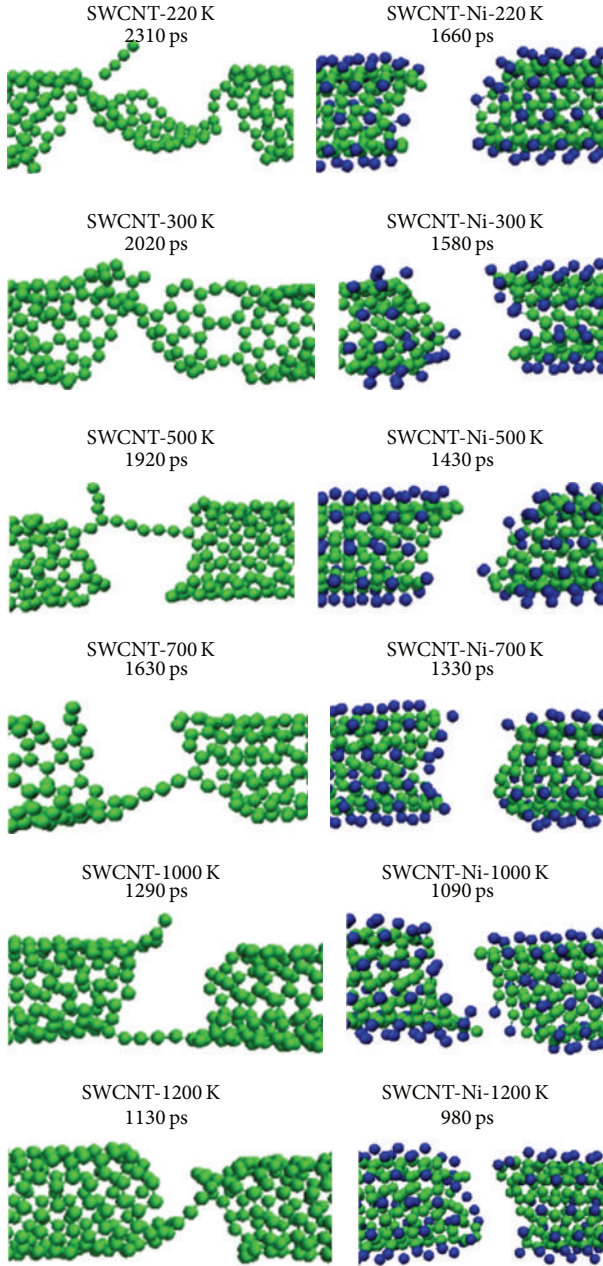


FIGURE 9: Rupture surfaces of SWCNT and SWCNT-Ni at different temperatures.

length of the nickel atoms increased with temperature, and the SWCNT-Ni had a larger thermal expansion coefficient; therefore, SWCNT-Ni was more temperature sensitive than SWCNT. At higher temperature during stretching, the C-C, C-Ni and Ni-Ni interactions were weakened, leading to the diversification of the mechanical properties, while the nickel atoms on the surface of the SWCNT-Ni played a role in interfering with the C-C bonds at a variety of temperatures.

4. Conclusions

In this work, using the second-generation Brenner reactive empirical bond-order potential with a modified attenuation

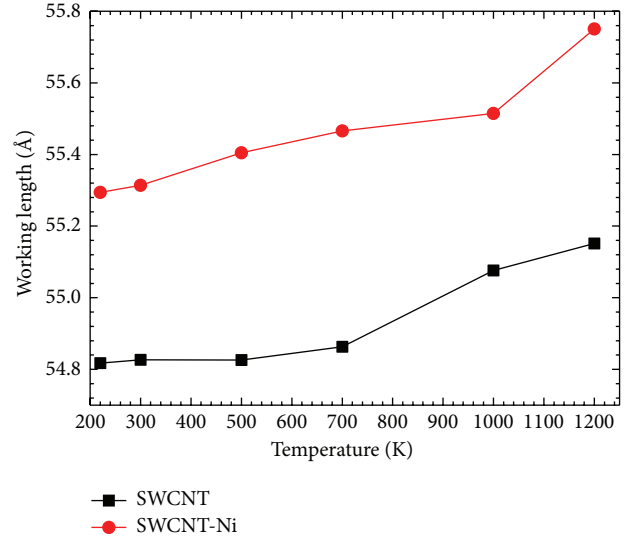


FIGURE 10: Initial working lengths of SWCNT and SWCNT-Ni at different temperatures.

distance of the attenuation function of the Brenner potential, MD simulations of stretching the armchair (6, 6) SWCNT and the SWCNT-Ni were conducted at different temperatures of 220 K, 300 K, 500 K, 700 K, 1000 K, and 1200 K. The simulation results revealed that the mechanical properties of both SWCNT and SWCNT-Ni were influenced by temperature. In particular, the failure stress and failure strain of SWCNT were obviously reduced at higher temperature, but Young's modulus of SWCNT was not very sensitive to temperature; however, when the temperature was above 1000 K, Young's modulus became greatly reduced. Compared with SWCNT, Young's modulus of SWCNT-Ni was lower at the same temperature. Meanwhile, the failure force and the failure stress of SWCNT and SWCNT-Ni were greatly weakened at higher temperatures. When the surface of SWCNT was coated with nickel atoms, the nickel atoms tended to bind to the carbon atoms. With increasing temperature, nickel atoms on the surface of SWCNT-Ni became more active, and the influence of the nickel interference with the C-C bond became more significant, thereby leading to increased temperature sensitivity of the mechanical properties of SWCNT-Ni.

Conflict of Interests

The authors declare that there is no conflict of interests regarding the publication of this paper.

Acknowledgments

This work is supported by 973 project (no. 2015CB057203) and the Fundamental Research Funds for the Central Universities, HUST: 2011TS066, 2013TS023. Technical assistance and suggestions from Dr. Dong Lin of Purdue University are greatly appreciated.

References

- [1] S. Iijima, "Helical microtubules of graphitic carbon," *Nature*, vol. 354, no. 6348, pp. 56–58, 1991.
- [2] P. Kim, L. Shi, A. Majumdar, and P. L. McEuen, "Thermal transport measurements of individual multiwalled nanotubes," *Physical Review Letters*, vol. 87, no. 21, 4 pages, 2001.
- [3] S. Berber, Y. K. Kwon, and D. Tománek, "Unusually high thermal conductivity of carbon nanotubes," *Physical Review Letters*, vol. 84, no. 20, pp. 4613–4616, 2000.
- [4] J. Xu and T. S. Fisher, "Enhancement of thermal interface materials with carbon nanotube arrays," *International Journal of Heat and Mass Transfer*, vol. 49, no. 9-10, pp. 1658–1666, 2006.
- [5] J. N. Coleman, U. Khan, W. J. Blau, and Y. K. Gun'ko, "Small but strong: a review of the mechanical properties of carbon nanotube-polymer composites," *Carbon*, vol. 44, no. 9, pp. 1624–1652, 2006.
- [6] Y. Zhang, N. W. Franklin, R. J. Chen, and H. Dai, "Metal coating on suspended carbon nanotubes and its implication to metal-tube interaction," *Chemical Physics Letters*, vol. 331, no. 1, pp. 35–41, 2000.
- [7] H. M. Duong, K. Ishikawa, J. Okawa et al., "Mechanism and optimization of metal deposition onto vertically aligned single-walled carbon nanotube arrays," *Journal of Physical Chemistry C*, vol. 113, no. 32, pp. 14230–14235, 2009.
- [8] S. Inoue and Y. Matsumura, "Molecular dynamics simulation of physical vapor deposition of metals onto a vertically aligned single-walled carbon nanotube surface," *Carbon*, vol. 46, no. 15, pp. 2046–2052, 2008.
- [9] C. Kim, B. Lim, B. Kim et al., "Strengthening of copper matrix composites by nickel-coated single-walled carbon nanotube reinforcements," *Synthetic Metals*, vol. 159, no. 5-6, pp. 424–429, 2009.
- [10] P. G. Collins, K. Bradley, M. Ishigami, and A. Zettl, "Extreme oxygen sensitivity of electronic properties of carbon nanotubes," *Science*, vol. 287, no. 5459, pp. 1801–1804, 2000.
- [11] S. Inoue and Y. Matsumura, "Influence of metal coating on single-walled carbon nanotube: molecular dynamics approach to determine tensile strength," *Chemical Physics Letters*, vol. 469, no. 1–3, pp. 125–129, 2009.
- [12] Y. Shibuta and S. Maruyama, "Bond-order potential for transition metal carbide cluster for the growth simulation of a single-walled carbon nanotube," *Computational Materials Science*, vol. 39, no. 4, pp. 842–848, 2007.
- [13] <http://lammmps.sandia.gov/>.
- [14] S. J. Stuart, A. B. Tutein, and J. A. Harrison, "A reactive potential for hydrocarbons with intermolecular interactions," *Journal of Chemical Physics*, vol. 112, no. 14, pp. 6472–6486, 2000.
- [15] T. Belytschko, S. P. Xiao, G. C. Schatz, and R. S. Ruoff, "Atomistic simulations of nanotube fracture," *Physical Review B: Condensed Matter and Materials Physics*, vol. 65, no. 23, 8 pages, 2002.
- [16] M. Sammalkorpi, A. Krasheninnikov, A. Kuronen, K. Nordlund, and K. Kaski, "Mechanical properties of carbon nanotubes with vacancies and related defects," *Physical Review B*, vol. 70, pp. 245416–245423, 2004.
- [17] W. J. Chang, "Molecular-dynamics study of mechanical properties of nanoscale copper with vacancies under static and cyclic loading," *Microelectronic Engineering*, vol. 65, no. 1-2, pp. 239–246, 2002.
- [18] M.-F. Yu, O. Lourie, M. J. Dyer, K. Moloni, T. F. Kelly, and R. S. Ruoff, "Strength and breaking mechanism of multiwalled carbon nanotubes under tensile load," *Science*, vol. 287, no. 5453, pp. 637–640, 2000.
- [19] S. L. Mielke, D. Troya, S. Zhang et al., "The role of vacancy defects and holes in the fracture of carbon nanotubes," *Chemical Physics Letters*, vol. 390, no. 4-6, pp. 413–420, 2004.
- [20] Y.-R. Jeng, P.-C. Tsai, and T.-H. Fang, "Effects of temperature and vacancy defects on tensile deformation of single-walled carbon nanotubes," *Journal of Physics and Chemistry of Solids*, vol. 65, no. 11, pp. 1849–1856, 2004.
- [21] K. Talukdar and A. K. Mitra, "Comparative MD simulation study on the mechanical properties of a zigzag single-walled carbon nanotube in the presence of Stone-Thrower-Wales defects," *Composite Structures*, vol. 92, no. 7, pp. 1701–1705, 2010.
- [22] N. Yao and V. Lordi, "Young's modulus of single-walled carbon nanotubes," *Journal of Applied Physics*, vol. 84, no. 4, pp. 1939–1943, 1998.
- [23] J.-P. Salvetat, G. A. D. Briggs, J.-M. Bonard et al., "Elastic and shear moduli of single-walled carbon nanotube ropes," *Physical Review Letters*, vol. 82, no. 5, pp. 944–947, 1999.
- [24] L. G. Zhou and S. Q. Shi, "Molecular dynamic simulations on tensile mechanical properties of single-walled carbon nanotubes with and without hydrogen storage," *Computational Materials Science*, vol. 23, no. 1–4, pp. 166–174, 2002.

Research Article

Enhancement in Mode II Interlaminar Fracture Toughness at Cryogenic Temperature of Glass Fiber/Epoxy Composites through Matrix Modification by Carbon Nanotubes and n-Butyl Glycidyl Ether

Yu Liu, Cheng-Bing Qu, Qing-Ping Feng, Hong-Mei Xiao, and Shao-Yun Fu

Technical Institute of Physics and Chemistry, Chinese Academy of Sciences, Beijing 100190, China

Correspondence should be addressed to Hong-Mei Xiao; hmxiao@mail.ipc.ac.cn and Shao-Yun Fu; syfu@mail.ipc.ac.cn

Received 12 June 2014; Accepted 27 August 2014

Academic Editor: Cheng Yan

Copyright © 2015 Yu Liu et al. This is an open access article distributed under the Creative Commons Attribution License, which permits unrestricted use, distribution, and reproduction in any medium, provided the original work is properly cited.

A typical diglycidyl ether of bisphenol-F (DGEBF)/diethyl toluene diamine (DETD) epoxy system modified by multiwalled carbon nanotubes (MWCNTs) and a reactive aliphatic diluent named n-butyl glycidyl ether (BGE) was used as the matrix for glass fiber composites. The glass fiber (GF) reinforced composites based on the unmodified and modified epoxy matrices were prepared by the hand lay-up hot-press process. Mode II interlaminar fracture toughness at both room temperature (RT) and cryogenic temperature (77 K) of the GF reinforced epoxy composites was investigated to examine the effect of the matrix modification. The result showed that the introduction of MWCNTs and BGE at their previously reported optimal contents led to the remarkable enhancement in mode II interlaminar fracture toughness of the composites. Namely, the 22.9% enhancement at RT and the 31.4% enhancement at 77 K were observed for mode II interlaminar fracture toughness of the fiber composite based on the optimally modified epoxy matrix by MWCNTs and BGE compared to the unmodified case.

1. Introduction

It is well known that matrices play a very important role in load transfer and crack resistance and hence significantly affect the mechanical properties of fiber reinforced composites. Epoxy resins are most popular matrices for fiber reinforced composites. Due to their shortages such as high brittleness, they are often modified by toughening agents. In our previous work [1], a reactive aliphatic diluent, namely, n-butyl glycidyl ether (BGE), was displayed to be a proper toughening agent for modifying epoxy resins. On the other hand, carbon nanotubes (CNTs) have exhibited excellent mechanical properties and also demonstrated a great potential as toughening agents for modifying epoxy resins [2–6].

Delamination of the composite laminates would take place when shear and peeling stress concentrations were high. And the fracture toughness under shear loading (i.e., mode

II interlaminar fracture toughness) is a critical property to evaluate the potential crack growth resistance [7]. Therefore, mode II interlaminar fracture toughness (G_{IIc}) is an important parameter for design of composites in practical applications. Shindo et al. [7] investigated G_{IIc} of glass fiber reinforced epoxy composites at cryogenic temperature. However, there is no report yet about mode II interlaminar fracture of fiber reinforced composites based on modified epoxy resins especially by both stiff modifier like CNTs and soft modifier such as BGE.

In our previous work [8], it has been demonstrated that the 0.5 wt% content of multiwalled CNTs was the optimal amount for modifying the epoxy resins since a higher CNT content would lead to CNT aggregates and thus deteriorated the epoxy performance. On the other hand, reactive BGE has also been displayed to have an effective role in modifying epoxy resins at the optimal content of 10 wt% [8]. At these optimal contents, the glass fiber reinforced composites based

on modified epoxy resins have shown great enhancements in tensile properties [9] and interlaminar shear strength at RT [10].

In this work, the diglycidyl ether of bisphenol F (DGEBF)/diethyl toluene diamine (DET D) epoxy system modified by multiwalled CNTs and BGE was prepared according to our previous works [1, 8–10] as the matrix. The glass fiber reinforced composites based on the unmodified and modified matrices were fabricated by the hand lay-up hot press process. Mode II interlaminar fracture toughness (G_{IIc}) at RT and 77 K of the glass fiber reinforced composites based on the unmodified and modified epoxy resins was investigated to examine the effect of matrix modification by multiwalled carbon nanotubes (MWCNTs) and BGE. The significant enhancement in mode II interlaminar fracture toughness at both RT and 77 K of the glass fiber reinforced composite was observed by the modification of the epoxy at the optimal contents of MWCNTs and BGE.

2. Experimental

2.1. Materials. Woven E-glass fibers (GF) were purchased from Feihangtongda Co., Ltd., China. The average diameter of single GF was about $11\ \mu\text{m}$. The epoxy resin used in this work was diglycidyl ether of bisphenol-F (DGEBF, D.E.R.354, Dow Chemical Co., USA) with the epoxide weight equivalence in the range of 167–174. The curing agent was diethyl toluene diamine (DET D, Kunshan Chemical Material Co., Ltd., China), which is a mixture of the two DET D isomers (74–80 wt.% 2,4-isomer and 18–24 wt.% 2,6-isomer). n-Butyl glycidyl ether (BGE, Changshu Jiafa Chemistry Co., Ltd., China) was used as a soft modifier for epoxy resin. Multiwalled carbon nanotubes (MWCNTs) made by CVD (purity >95 wt.%, Chengdu Organic Chemicals Co., Ltd., China) were employed as a stiff modifier for epoxy resins. The diameters of the nanotubes were in the range of 30–50 nm and the length was between 10 and $20\ \mu\text{m}$ [8]. The chemical structures of DGEBF, DET D, and BGE have been given in our previous work [9].

2.2. Preparation of Composites. The preparation of the glass fiber reinforced epoxy composite has been given in detail in our previous works [10] and is briefly described here. First, the modified epoxy matrix was prepared by mixing epoxy resins and other additives at 50°C . The pure epoxy system was also employed as the matrix for the purpose of comparison. Formulations of unmodified and modified epoxy resins as matrices are shown in Table 1. Second, glass fiber clothes were impregnated with these epoxy resins. Twenty impregnated prepregs were stacked via the hand lay-up method and glass fiber reinforced composites based on the unmodified and modified matrices were fabricated by the hot-press process via the curing press machine (QLB 40T) under 5 MPa. Temperature and pressure profiles for manufacturing composites are shown in Figure 1. In order to induce the initial cracks between the middle layers, thin release films were partially placed during fabrication. Finally, the composites were cured at 130°C for 10 h. The resulting

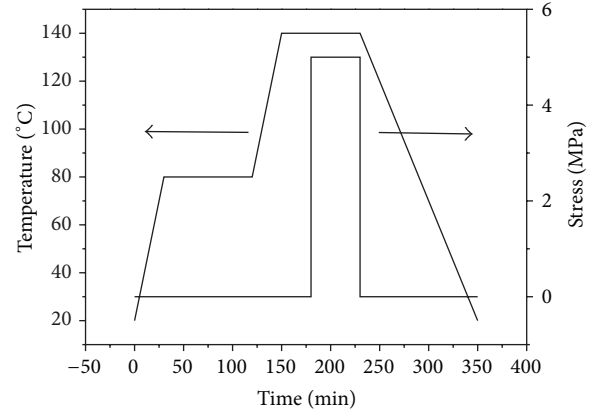


FIGURE 1: Temperature and pressure profiles for manufacturing glass fiber reinforced composites.

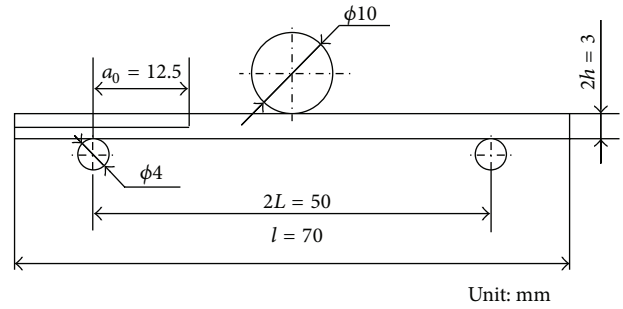


FIGURE 2: The dimensions of the samples for measurement of G_{IIc} .

glass fiber reinforced composites have a fiber volume content of about 56% [10]. The specimens for the mechanical tests were cut from the composite plates. The dimensions of the samples for measurement of G_{IIc} are shown Figure 2.

2.3. Measurement. In the end notched flexure (ENF) test, the critical energy release rate is determined by [11]:

$$G_{IIc} = \frac{9P_1^2 a_1^2 C_1}{2b(3a_1^3 + 2L^3)}, \quad (1)$$

$$a_1 = \left[\frac{C_1}{C_0} a_0^3 + \frac{2}{3} \left(\frac{C_1}{C_0} - 1 \right) L^3 \right]^{1/3},$$

where a_0 and a_1 are the initial crack length and the crack length at the critical load, respectively. C_0 indicates the compliance within initial elastic deformation without crack growth and C_1 indicates the compliance at the critical load. P_1 is the critical load which can be determined by the maximum load or 5% offset load according to the load-displacement curve. b and $2L$ represent the width and the span length of the specimen, respectively. All the tests were performed using an Instron 5882 universal machine with 5 kN load cell. The crosshead rate was 2 mm/min at both RT and 77 K. The cryogenic temperature condition was achieved by immersing the specimens completely in a liquid nitrogen filled cryostat to ensure the uniform temperature of 77 K [12]. At least five specimens were tested for each composition.

TABLE 1: Interlaminar fracture toughness at RT and 77 K for the composites based on unmodified and modified epoxy resins.

Matrix	DGEBF (g)	DETD (g)	MWCNT (g)	BGE (g)	G_{IIC} (kJ/m ²)	
					RT	77 K
A	100	25.8			1.40 ± 0.03	3.25 ± 0.25
B	99.5	25.7	0.5		1.46 ± 0.08	3.63 ± 0.40
C	100	28.4		10	1.59 ± 0.04	3.99 ± 0.42
D	99.5	28.3	0.5	10	1.72 ± 0.07	4.27 ± 0.32

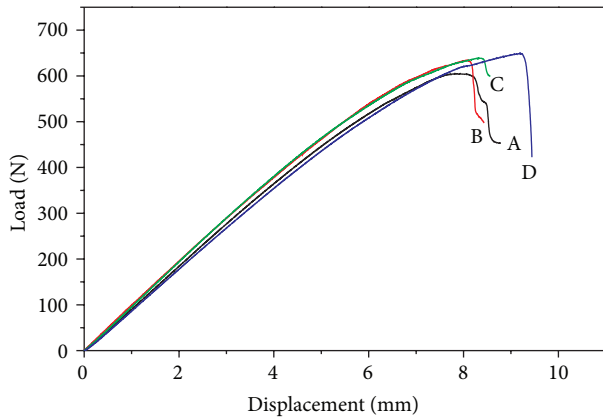


FIGURE 3: Typical ENF load-displacement curves at room temperature for (A) unmodified epoxy/glass fiber composite, (B) MWCNT modified epoxy/glass fiber composite, (C) BGE modified epoxy/glass fiber composite, and (D) both MWCNT and BGE modified epoxy/glass fiber composite.

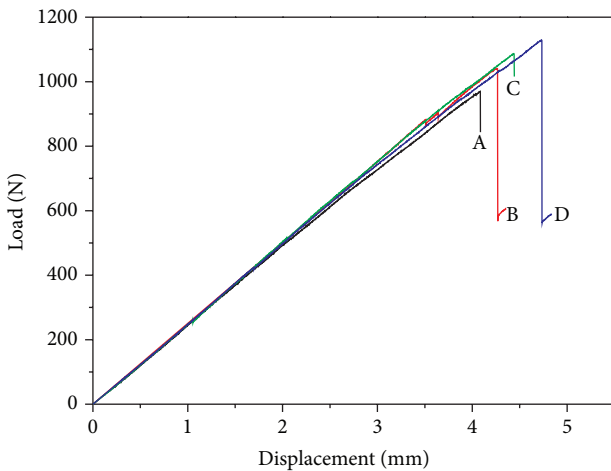


FIGURE 4: Typical ENF load-displacement curves at 77 K for (A) unmodified epoxy/glass fiber composite, (B) MWCNT modified epoxy/glass fiber composite, (C) BGE modified epoxy/glass fiber composite, and (D) both MWCNT and BGE modified epoxy/glass fiber composite.

The fracture surfaces of the composites were evaluated by scanning electron microscopy (SEM, Hitachi S-4300) at an accelerating voltage of 10 kV. All specimens were coated with a thin layer of gold to eliminate charging effects.

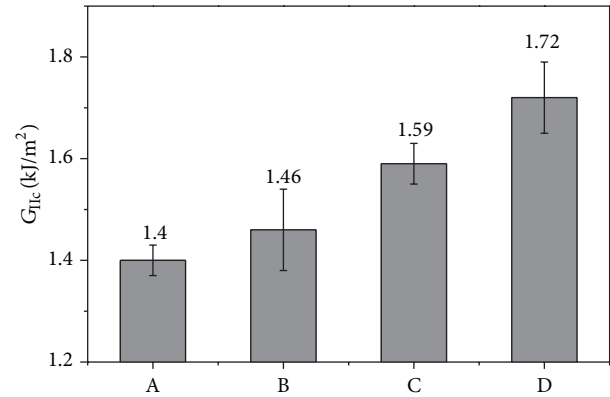


FIGURE 5: The interlaminar fracture toughness at room temperature for (A) unmodified epoxy/glass fiber composite, (B) MWCNT modified epoxy/glass fiber composite, (C) BGE modified epoxy/glass fiber composite, and (D) both MWCNT and BGE modified epoxy/glass fiber composite.

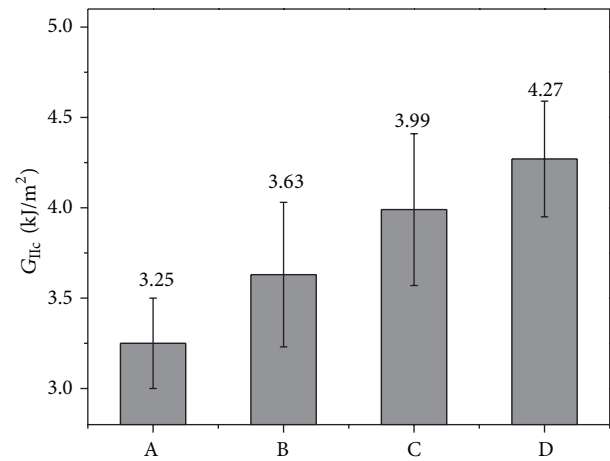


FIGURE 6: The interlaminar fracture toughness at 77 K for (A) unmodified epoxy/glass fiber composite, (B) MWCNT modified epoxy/glass fiber composite, (C) BGE modified epoxy/glass fiber composite, and (D) both MWCNT and BGE modified epoxy/glass fiber composite.

3. Results and Discussion

3.1. Mode II Interlaminar Fracture Toughness. Typical ENF load-displacement curves at room temperature (RT) and liquid nitrogen temperature (77 K) for the composites are shown in Figures 3 and 4, respectively. At RT, the applied load

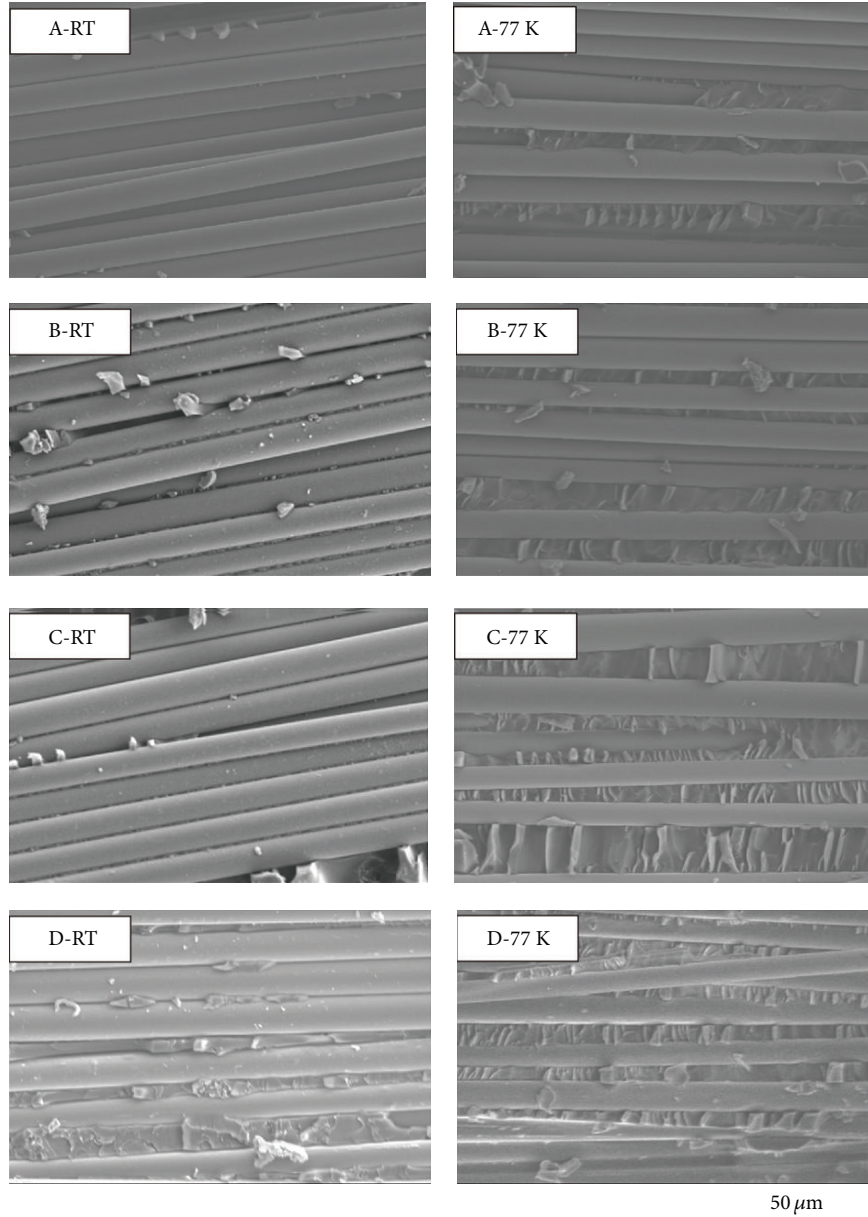


FIGURE 7: SEM images for the fracture surfaces (crack growth from left to right) after testing at RT and 77 K of (A) unmodified epoxy/glass fiber composite, (B) MWCNT modified epoxy/glass fiber composites, (C) BGE modified epoxy/glass fiber composite, and (D) both MWCNT and BGE modified epoxy/glass fiber composites.

shows nonlinearity at a relatively low load about 300 N. After attaining the maximum value, the load decreases gradually to the failure. In contrast, at 77 K, the applied load shows a linear relationship with the displacement and unstable crack growth occurs when the maximum value is reached. Moreover, the maximum load at 77 K is much higher than that at RT. In addition, it should be noted that the maximum load for the composite based on the modified epoxy matrix is higher than that based on the pure epoxy matrix at both RT and 77 K.

The results for the interlaminar fracture toughness at RT and 77 K are shown in Figures 5 and 6, respectively. It can be easily noticed that G_{IIC} of the composites based on the modified matrix is higher than that of the composite

based on the unmodified epoxy matrix at both RT and 77 K. Moreover, G_{IIC} at 77 K is much higher than that at RT for the same composite. When the temperature decreased from RT to 77 K, the chemical bond of the epoxy matrix would shrink and the binding forces between matrix and fiber would become stronger [8]. The higher mechanical performance at 77 K compared to RT might be attributed to the stronger binding forces at 77 K compared to RT.

The data for the interlaminar fracture toughness at RT and 77 K for the composites based on unmodified and modified epoxy matrices are given in Table 1. At RT, G_{IIC} of Samples B and C are 4.3% and 13.6% higher compared to Sample A, respectively. In particular, the incorporation

of both MWCNTs and BGE (Sample D) results in 22.9% improvement in G_{IIC} compared to Sample A. On the other hand, at 77 K, G_{IIC} of Samples B and C are improved by 11.7% and 22.8% compared to Sample A, respectively. Moreover, the G_{IIC} value of Sample D is enhanced by 31.4% compared to Sample A. Consequently, it can be seen that the simultaneous incorporation of MWCNTs and BGE into the epoxy resin leads to the maximum enhancements in G_{IIC} . In addition, the enhancement in G_{IIC} at 77 K was higher than that at RT, this was likely because the chemical bond and molecules of the epoxy matrix would shrink and the binding forces between molecules would become stronger when the temperature decreased from RT to 77 K [8].

3.2. Microstructure of the Composites. The SEM images are presented in Figure 7 for the fracture surfaces of the ENF specimens. It is revealed that at RT, GF of the composite samples with modified matrices have a rougher surface than those of Sample A. The fracture surface observation coincides with the results for G_{IIC} of samples. This indicates that the incorporation of MWCNTs and BGE into the conventional GFRP composites based on the pure epoxy matrix creates an increased fracture surface due to crack deflection [13], which will lead to the enhancement in the interlaminar fracture toughness. Sample D with the simultaneous introduction of MWCNTs and BGE into the epoxy resin shows the noticeable effect on the improvement of interlaminar fracture toughness.

At 77 K, the decrease in temperature makes the epoxy more brittle and reduces its strain to failure. The hackle mark features are shown in Figure 7. These hackle patterns are likely caused by secondary cracks [14]. The hackle patterns are more obvious at 77 K than at RT. The increased fracture surface of the hackle pattern morphology means more surface energy dissipation and therefore an increase of the interlaminar fracture toughness compared to the RT case. The hackle pattern formation also helps to reduce the stress (or strain) concentration at the tip of the principal crack [15]. Therefore, it is reasonable to observe that the simultaneous introduction of MWCNTs and BGE into the epoxy matrix has brought about the significant enhancement in mode II interlaminar fracture toughness.

4. Conclusions

In this work, glass fiber reinforced composites have been prepared by the hand lay-up hot press process based on unmodified and modified epoxy matrices by introducing MWCNTs and BGE into a pure epoxy resin in modifying the epoxy resins. Mode II interlaminar fracture toughness (G_{IIC}) of the glass fiber reinforced composites has been investigated at both room temperature (RT) and cryogenic temperature (77 K) to examine the effect of the matrix modification. It has been clearly demonstrated that the epoxy modification by both MWCNTs and BGE can lead to great enhancements in G_{IIC} at both RT and 77 K.

Conflict of Interests

The authors declare that there is no conflict of interests regarding the publication of this paper.

Acknowledgments

This work was financially supported by the National Natural Science Foundation of China (nos. 51373187 and 11372312) and the Beijing Municipal Natural Science Foundation (no. 2122055).

References

- [1] Z. K. Chen, G. Yang, J. P. Yang, S. Y. Fu, L. Ye, and Y. G. Huang, "Simultaneously increasing cryogenic strength, ductility and impact resistance of epoxy resins modified by n-butyl glycidyl ether," *Polymer*, vol. 50, no. 5, pp. 1316–1323, 2009.
- [2] S. Wang, Z. Liang, T. Liu, B. Wang, and C. Zhang, "Effective amino-functionalization of carbon nanotubes for reinforcing epoxy polymer composites," *Nanotechnology*, vol. 17, no. 6, pp. 1551–1557, 2006.
- [3] P. Guo, X. Chen, X. Gao, H. Song, and H. Shen, "Fabrication and mechanical properties of well-dispersed multiwalled carbon nanotubes/epoxy composites," *Composites Science and Technology*, vol. 67, no. 15–16, pp. 3331–3337, 2007.
- [4] L. Guadagno, L. Vertuccio, A. Sorrentino et al., "Mechanical and barrier properties of epoxy resin filled with multi-walled carbon nanotubes," *Carbon*, vol. 47, no. 10, pp. 2419–2430, 2009.
- [5] Q. F. Cheng, J. P. Wang, J. J. Wen et al., "Carbon nanotube/epoxy composites fabricated by resin transfer molding," *Carbon*, vol. 48, no. 1, pp. 260–266, 2010.
- [6] Y. Breton, G. Désarmot, J. P. Salvetat et al., "Mechanical properties of multiwall carbon nanotubes/epoxy composites: influence of network morphology," *Carbon*, vol. 42, no. 5–6, pp. 1027–1030, 2004.
- [7] Y. Shindo, F. Narita, and T. Sato, "Analysis of mode II interlaminar fracture and damage behavior in end notched flexure testing of GFRP woven laminates at cryogenic temperatures," *Acta Mechanica*, vol. 187, pp. 231–240, 2006.
- [8] Z.-K. Chen, J.-P. Yang, Q.-Q. Ni, S.-Y. Fu, and Y.-G. Huang, "Reinforcement of epoxy resins with multi-walled carbon nanotubes for enhancing cryogenic mechanical properties," *Polymer*, vol. 50, no. 19, pp. 4753–4759, 2009.
- [9] Y. Liu, H. M. Xiao, Q. P. Feng, and S. Y. Fu, "Synergistic effect of carbon nanotubes and n-butyl glycidyl ether on matrix modification for improvement of tensile performance of glass fiber/epoxy composites," *Composites A*, vol. 62, pp. 39–44, 2014.
- [10] Y. Liu, J.-P. Yang, H.-M. Xiao et al., "Role of matrix modification on interlaminar shear strength of glass fibre/epoxy composites," *Composites B: Engineering*, vol. 43, no. 1, pp. 95–98, 2012.
- [11] W.-X. Wang, M. Nakata, Y. Takao, and T. Matsubara, "Experimental investigation on test methods for mode II interlaminar fracture testing of carbon fiber reinforced composites," *Composites A: Applied Science and Manufacturing*, vol. 40, no. 9, pp. 1447–1455, 2009.
- [12] J. P. Yang, G. Yang, G. Xu, and S. Y. Fu, "Cryogenic mechanical behaviors of MMT/epoxy nanocomposites," *Composites Science and Technology*, vol. 67, no. 14, pp. 2934–2940, 2007.
- [13] T. Yokozeki, Y. Iwahori, M. Ishibashi et al., "Fracture toughness improvement of CFRP laminates by dispersion of cup-stacked

carbon nanotubes,” *Composites Science and Technology*, vol. 69, no. 14, pp. 2268–2273, 2009.

- [14] H. Lau and R. E. Rowlands, “Fracture morphology of composites tested at RT and 77K,” *Advances in Cryogenic Engineering*, vol. 36, pp. 913–919, 1990.
- [15] Y. Shindo, D. Shinohe, S. Kumagai, and K. Horiguchi, “Analysis and testing of mixed-mode interlaminar fracture behavior of glass-cloth/epoxy laminates at cryogenic temperatures,” *Journal of Engineering Materials and Technology, Transactions of the ASME*, vol. 127, no. 4, pp. 468–475, 2005.

Research Article

Micromechanical Behavior of Single-Crystal Superalloy with Different Crystal Orientations by Microindentation

Jinghui Li,¹ Fuguo Li,¹ Junzhe Dong,¹ Zhanwei Yuan,² and Shuo Zhang³

¹State Key Laboratory of Solidification Processing, School of Materials Science and Engineering, Northwestern Polytechnical University, Xi'an 710072, China

²School of Materials Science and Engineering, Chang'an University, Xi'an 710061, China

³School of Materials Science and Engineering, Tsinghua University, Beijing 100062, China

Correspondence should be addressed to Fuguo Li; 1037832244@qq.com

Received 2 September 2014; Accepted 5 January 2015

Academic Editor: Sheng-Rui Jian

Copyright © 2015 Jinghui Li et al. This is an open access article distributed under the Creative Commons Attribution License, which permits unrestricted use, distribution, and reproduction in any medium, provided the original work is properly cited.

In order to investigate the anisotropic micromechanical properties of single-crystal nickel-based superalloy DD99 of four crystallographic orientations, (001), (215), (405), and (605), microindentation test (MIT) was conducted with different loads and loading velocities by a sharp Berkovich indenter. Some material parameters reflecting the micromechanical behavior of DD99, such as microhardness H , Young's modulus E , yield stress σ_y , strain hardening component n , and tensile strength σ_b , can be obtained from load-displacement relations. H and E of four different crystal planes evidently decrease with the increase of h . The reduction of H is due to dislocation hardening while E is related to interplanar spacing and crystal variable. σ_y of (215) is the largest among four crystal planes, followed by (605), and (001) has the lowest value. n of (215) is the lowest, followed by (605), and that of (001) is the largest. Subsequently, a simplified elastic-plastic material model was employed for 3D microindentation simulation of DD99 with various crystal orientations. The simulation results agreed well with experimental, which confirmed the accuracy of the simplified material model.

1. Introduction

In recent years, single-crystal nickel-based superalloys are widely used as blade of modern gas turbine aeroengines, as they significantly raise the operation temperature and efficiency due to excellent mechanical properties in service [1–6]. Their excellent high-temperature properties are superior to conventional cast alloys, such as high-temperature creep and oxidation-resistant performance, which results from the elimination of grain boundaries in single-crystal alloys. However, the absence of grain boundaries also leads to orientation-dependent material response [7–9]. To date, a lot of researches concerned about different orientation of single-crystal nickel-based superalloys have been done. Caron et al. [10] investigated the anisotropic creep behavior of some advanced superalloys (CMSX-2, Alloy 454, MXON, and CMSX-4) in the temperature ranging from 1033 to 1323 K. He et al. [11] discussed the creep/fatigue damage characteristics of DD6

and the results show the capability of DD6 to avoid fatigue damage in [011] direction is better than that in [001] direction. Yi et al. [12] gave modeling process of tertiary creep of single-crystal superalloy along different orientations. Wu et al. [13] made extensile and compression tests at different temperatures on DD8 with various strain rates and the results indicate that the tendency to the plastic deformation inhomogeneity decreases in the order of [011], [001], and [111]. The previous investigations mainly concentrated on the fatigue life and creep properties with different orientations, while other fundamental performances of materials, such as hardness, Young's modulus, and yield stress are rarely focused on.

Conventional tensile tests are difficult to conduct at nano- and microscales to determine orientation dependent behavior. Microindentation can be an alternative approach to tension or compression to probe the micromechanical properties, such as elastic modulus and hardness. Due to its precise measurement and advantages of celerity, accuracy,

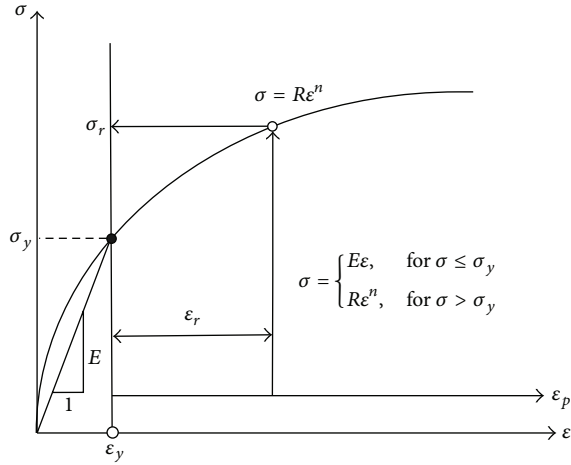


FIGURE 1: Power-law elastic-plastic, true stress-strain behavior [14].

and nondestructiveness [15], it will become increasingly popular in the future. However, thorough understanding of materials behavior under indenter cannot be achieved just through MIT; for example, the equivalent stress and strain cannot be obtained directly by indentation.

FEM may be used as a supplement to solve complex 3D problems and more information can be extracted from microindentation simulation [16–18]. Lim and Munawar Chaudhri [19] investigated microindentation hardness of individual grains [(110) and (111) surfaces] of a polycrystalline copper using a spherical indenter and reported the indentation hardness in copper with different orientations to be very similar. Liu et al. [20] performed nanoindentation simulation using 3D elastic-plastic crystal plasticity FEM on single-crystal copper specimens on three orientations [(011), (100), and (111)] using a conical indenter and reported twofold, fourfold, and sixfold symmetries on (011), (100), and (111) faces, respectively. Fivel et al. [21] developed a 3D model to combine discrete dislocations with FEM for nanoindentation simulation on single-crystal copper. However, most of these researches were based on material properties of single-crystal data obtained from tensile testing at macroscale. In fact, it is essential to extract these parameters at micrometer scale.

In this paper, MIT were conducted on crystal planes of nickel-based single-crystal DD99 to investigate its micromechanical properties. Subsequently, a FEM model based on the results of MIT was implemented in 3D ABAQUS/Explicit to prove the accuracy of this FEM model.

2. Calculation Methods

2.1. Elastic-Plastic Properties. The load-displacement response obtained by microindentation contains information about the elastic and plastic deformation of the indented materials. Therefore, it is often regarded as “fingerprint” of materials’ properties under identification [22]. Mechanical properties, such as the hardness and Young’s modulus, can be readily extracted from the load-displacement curves. In general,

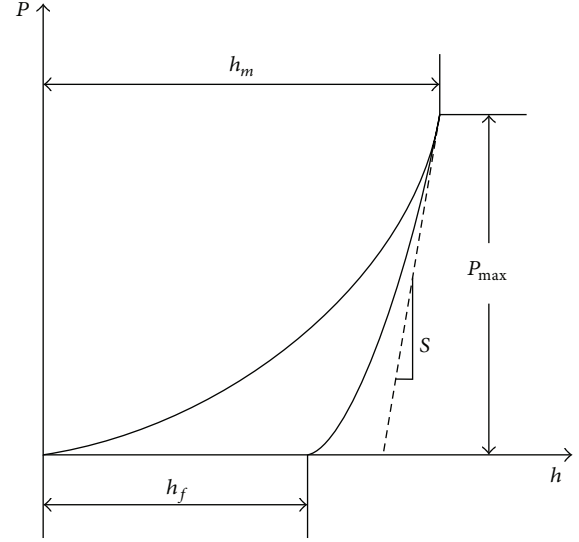


FIGURE 2: The typical P - h curve in instrumented indentation test.

plastic behavior of metals can be characterized by a power-law description, as shown in Figure 1. A simplified elastic-plastic, true stress-strain behavior can be expressed as

$$\sigma = \begin{cases} E\varepsilon, & \text{for } \sigma \leq \sigma_y \\ R\varepsilon^n, & \text{for } \sigma \geq \sigma_y. \end{cases} \quad (1)$$

When σ is equal to σ_y , R can be deduced as follows:

$$R = \sigma_y \left(\frac{E}{\sigma_y} \right)^n. \quad (2)$$

Thus, (1) can be rewritten as follows:

$$\sigma = \begin{cases} E\varepsilon, & \text{for } \sigma \leq \sigma_y \\ \sigma_y \left(1 + \frac{E}{\sigma_y} \varepsilon_r \right)^n, & \text{for } \sigma \geq \sigma_y. \end{cases} \quad (3)$$

In order to describe the mechanical properties of a power-law material, Young’s modulus E , yield stress σ_y , and strain hardening exponent n are needed.

The typical P - h curve of microindentation test is shown in Figure 2. Two important parameters (maximum indentation depth h_m and maximum load P_m) can be obtained from the curve. According to Kick’s law, the loading curve of indentation can be expressed as

$$P = Ch^2. \quad (4)$$

According to the model proposed by Oliver and Pharr [23, 24], unloading curve can be interpreted as

$$P = B \times (h - h_f)^t. \quad (5)$$

The relationship between the apparent modulus E^* and Young’s modulus E is as follows:

$$\frac{1}{E^*} = \frac{1 - \nu^2}{E} + \frac{1 - \nu_i^2}{E_i}. \quad (6)$$

E_i and ν_i are Young's modulus and Poisson's ratio of the indenter whose values are 1141 GPa and 0.07 for diamond indenter, respectively [25].

According to King [26], E^* has the form

$$E^* = \frac{\sqrt{\pi} S}{2\beta Q}. \quad (7)$$

S and Q can be obtained by the following equations, respectively:

$$S = \left. \frac{dP}{dh} \right|_{h=h_m} = m \times B (h_m - h_f)^{m-1}, \quad (8)$$

$$Q = \pi \left(h_m - \gamma \frac{P_m}{S} \right)^2 \tan^2 \theta = K \left(h_m - \gamma \frac{P_m}{S} \right)^2, \quad (9)$$

where K is a constant related with indenter, whose value is 24.56 for Berkovich indenter, and γ is a coefficient with value of 0.75 for Berkovich indenter [27, 28].

The next task is to find the yield stress σ_y and strain hardening exponent n . The method used to obtain σ_y and n is dimensional analysis proposed by Y. T. Cheng and C. M. Cheng and Tunvisut et al. [29–33]. For a sharp indenter (Berkovich indenter in this paper), the load P can be related with the following parameters [34]:

$$P = P(h, E^*, \sigma_c, n). \quad (10)$$

According to Π theorem in dimensional analysis, the equation above can be rewritten as

$$P = \sigma_c h^2 \Pi_1 \left(\frac{E^*}{\sigma_c}, n \right). \quad (11)$$

Π_1 function is independent of n when strain is equal to 0.033 [34]. And $\sigma_{0.033}$ can be obtained as

$$\begin{aligned} \Pi_1 \left(\frac{E^*}{\sigma_{0.033}} \right) &= \frac{C}{\sigma_{0.033}} \\ &= -1.131 \left[\ln \left(\frac{E^*}{\sigma_{0.033}} \right) \right]^3 \\ &\quad + 13.635 \left[\ln \left(\frac{E^*}{\sigma_{0.033}} \right) \right]^2 \\ &\quad - 30.594 \left[\ln \left(\frac{E^*}{\sigma_{0.033}} \right) \right] + 29.267. \end{aligned} \quad (12)$$

Similarly, the unloading slope can be described as follows at $h = h_m$:

$$\left. \frac{dP_u}{dh} \right|_{h=h_m} = S = E^* h_m \Pi_2 \left(\frac{E^*}{\sigma_c}, n \right), \quad (13)$$

$$\begin{aligned} \Pi_2 \left(\frac{E^*}{\sigma_c}, n \right) &= \frac{S}{E^* h_m} \\ &= (-1.40557n^3 + 0.77526n^2 + 0.1583n - 0.06831) \\ &\quad \cdot \left[\ln \left(\frac{E^*}{\sigma_{0.033}} \right) \right]^3 \\ &\quad + (17.93006n^3 - 9.22091n^2 - 2.37733n + 0.86295) \\ &\quad \cdot \left[\ln \left(\frac{E^*}{\sigma_{0.033}} \right) \right]^2 \\ &\quad + (-79.99715n^3 + 40.5562n^2 + 9.00157n - 2.54543) \\ &\quad \cdot \left[\ln \left(\frac{E^*}{\sigma_{0.033}} \right) \right] \\ &\quad + (122.65069n^3 - 63.88418n^2 - 9.58936n + 6.20045). \end{aligned} \quad (14)$$

Finally, after plugging value of $\sigma_{0.033}$ and n into (3), σ_y can be calculated. Thus, one can obtain the elastic-plastic model characterized by a power-law function based on (1) and (2).

2.2. Tensile Strength. The ultimate tensile strength characterizes the resistance of largest uniform plastic deformation. The tensile strength is usually determined by uniaxial tensile test: the highest point of the stress-strain curve is the tensile strength. However, it can also be calculated by MIT.

In the stage of uniform plastic deformation stage, load F is as follows:

$$F = \sigma A. \quad (15)$$

The result of differential calculation of (15) is

$$\frac{dF}{F} = \frac{d\bar{\sigma}}{\bar{\sigma}} + \frac{dA}{A}. \quad (16)$$

When nonuniform deformation such as necking occurs on certain part of materials, F reaches its maximum value and $dF = 0$. According to (16), it can be induced that

$$\frac{d\bar{\sigma}}{\bar{\sigma}} = -\frac{dA}{A} = d\varepsilon, \quad (17)$$

$$\frac{d\bar{\sigma}}{d\varepsilon} = \bar{\sigma}. \quad (18)$$

It has the following relationship, according to (18):

$$\left. \frac{d\sigma}{d\varepsilon} \right|_{\varepsilon=\varepsilon_b} = \bar{\sigma}|_{\varepsilon=\varepsilon_b}. \quad (19)$$

According to (19), ε_b can be calculated and it is equal to n , which has been confirmed by [35]. Consider

$$F = \sigma_b A = \bar{\sigma}_b A_b = (R\varepsilon_b^n) A_b = (Rn^n) A_b, \quad (20)$$

$$\sigma_b = (Rn^n) \frac{A_b}{A}. \quad (21)$$

TABLE 1: Chemical composition of DD99 superalloy (mass fraction, %).

C	Cr	Co	W	Al	Ti	Ta	Ni
0.016	8.5	5.0	9.5	5.5	2.2	2.8	Bal.

Its formula is

$$\ln \frac{A}{A_b} = \varepsilon_b. \quad (22)$$

According to (21) and (22), σ_b can be calculated:

$$\sigma_b = (Rn^n) e^{-\varepsilon_b} = (Rn^n) e^{-n} = R \left(\frac{n}{e} \right)^n. \quad (23)$$

2.3. Microhardness. Hardness is an ability of resistance to permanent (plastic) deformation. It represents the overall mechanical properties of materials. For example, hardness is related to other mechanics parameters, such as Young's modulus, yield stress, and strain hardening component [36]. Besides, many references have shown that the intrinsic material length scale characterizing size scale can be identified from microhardness [37–41]. It has been found that the microhardness of materials is significantly higher than the microhardness and, furthermore, the correlation of microhardness and the indentation depth implies that the materials strength depends on both the absolute specimen size and strain gradients. Therefore, the results of the microhardness provide a new implication for the strain gradient-dependent constitutive equations in continuum plasticity theory. This has led to the development of phenomenological or mechanism-based strain gradient plasticity (SGP) theories, which have been used to interpret the size dependence of hardness from the micro- to nanoscales.

Shim et al. [42] guessed the yield strength very roughly based on the hardness values from Berkovich indentations. Nix and Gao [43] showed that equivalent stress (σ_{eq}) has the following relationship with hardness: $\sigma_{eq} = H/3$. As a testing method under micro- and nanoscale, MIT plays an important role in the evaluation of microhardness and the microhardness can be obtained as follows:

$$H = \frac{P_m}{Q} = \frac{P_m}{\pi (h_m - \gamma (P_m/S))^2 \tan^2 \theta}. \quad (24)$$

3. Experimental and Simulation Procedures

3.1. Experimental Procedure. The nominal chemical compositions of as-received single-crystal nickel-based superalloy DD99 (5 mm × 5 mm × 3 mm rectangle block) which has its crystal plane (001) marked in advance are shown in Table 1.

Although nickel-based single crystal has the optimum performance along crystal orientation [001] [14], there inevitably exist misorientations for actual engineering application. Moreover, as the structures of production, such as blade parts of aeroengine, are complicated, it is difficult to guarantee each plane of the product is parallel to [001]. In order to investigate the orientation dependent properties

and provide performance reference of different planes for engineering applications in the future, the specimens of DD99 were subjected to wire-electrode cutting with angle of 30°, 45°, and 60° to crystal plane (001), as shown in Figures 3(a), 3(b), and 3(c). The red lines in Figure 3 represent molybdenum wire used in wire-electrode cutting and the cutting curve is parallel to [010].

The cutting specimens along with the original one with crystal plane (001) were carefully ground with sand paper. Then, they were polished with 1.5 μm diamond to mirror finish. Subsequently, the specimens were etched with corrosives (5 g CuSO₄ + 20 mL HCl + 100 mL H₂O) for 15 s to reduce the influence of surface hardening. Finally, MIT was performed using the commercial MCT W501 equipped with a Berkovich diamond indenter at room temperature. The test condition was shown in Table 2. There are four different loading velocities and under each of them nine different maximum loads were conducted. Notably, each test was conducted five times and the average values were calculated in order to eliminate the errors.

3.2. Simulation Procedure. In the researches of Li et al. [44] and Yuan et al. [45], the axisymmetric 2D was created by using the quadrilateral elements to simulate the indentation process and the *P-h* line of FEM is slightly higher than that of experiments. Walter and Mitterer [46] found that 2D model predicts higher scatter and relatively higher mean Young's modulus compared to 3D model. According to researches from FEM simulation of indentation, it can be concluded that the main differences between 2D and 3D model are in the following two aspects.

In terms of the shape of indenter, the Berkovich indenter of 2D model is represented by a straight with an angle of 70.3° to axis of symmetry, indicating the indenter itself as a whole is conical. In contrast, the real shape of Berkovich indenter is triangular pyramid. Considering the boundary conditions, circumferential displacement in 2D model is constrained and only the displacement in radial direction is permitted. By comparison, constrained circumferential displacement just appears on the symmetry plane and deformation can be expanded in both circumferential and radial direction within matrix in 3D model. Considering above variations and the fact that 2D model cannot be utilized to discuss the orientation dependent properties due to its rotational symmetry, a 3D simulation seems preferable, even though computational time is considerably higher.

The Berkovich indenter is a triangular-based pyramid having a threefold symmetry. The load is applied along the axis of the indenter; thus the load symmetry is the same as the geometric one. For these considerations, a three-dimensional model is defined only by one-third of the entire system. The 3D model setup is shown in Figure 4. In the simulations, the indenter is modeled as a rigid body. This is justified as the diamond indenter has a modulus of 1141 GPa. In this paper, the dimension of material in FEM model is 2 mm × 2 mm × 1 mm, which is much larger than maximum indentation displacement. As for the mesh section, size of mesh is generally a compromise between the computational cost and the solution accuracy. Based on various deformation levels,

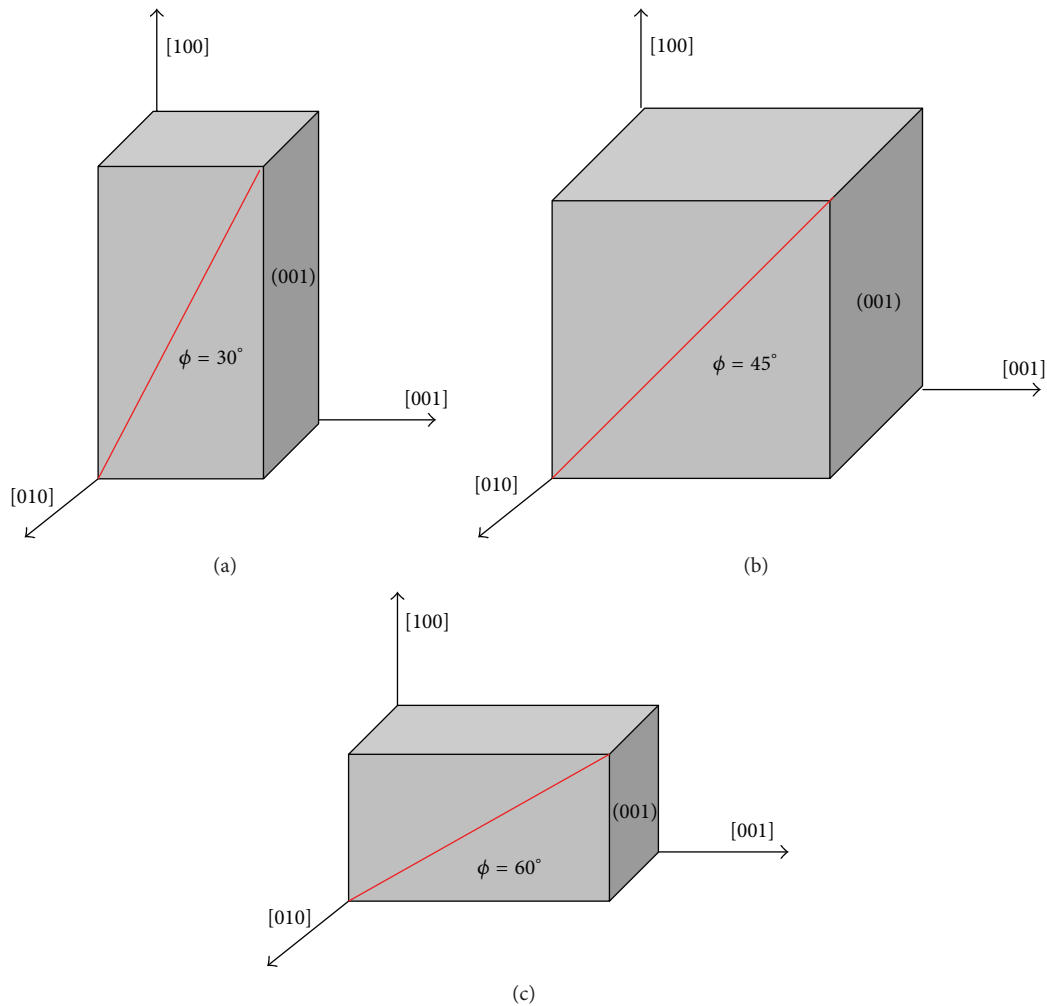


FIGURE 3: Schematic diagram of specimens with different cutting angles: (a) 30°; (b) 45°; (c) 60°.

TABLE 2: MIT condition.

Max load (mN)	500	1000	1500	2000	2500	3000	3500	4000	4500
Velocity (mN/s)		17.2842		34.5684		51.8527		103.7053	

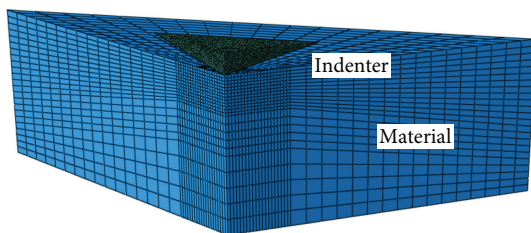


FIGURE 4: Microindentation model setup.

a finer mesh is used near the indenter tip and a coarser mesh for farther regions. And the element of material is C3D8R, while that of indenter is R3D3. The effect of friction coefficient on the nanoindentation behavior has been investigated by Liu et al. [47], illustrating that the friction does not change the load-displacement relationship. A lower friction contact

pair is defined by two contact surfaces with associated nodes between the indenter and the material. In addition, boundary conditions are defined as an element on two symmetry planes parallel to indenter movement direction constrained, only able to expand along radial and axial direction with the help of cylindrical coordinate. But the elements on the bottom of material were defined as having no displacement in any direction.

4. Experimental Results and Analysis

4.1. Microhardness and Tensile Strength. The load-displacement curves (P - h curves) of crystal plane (405) under loading velocity of 17.284 mN/s are shown in Figure 5. It can be found that curves of various loads show similar shape, which indicates a better repeatability of indentation tests. Different from the nanoindentation test, no “pop-in” size by the abrupt

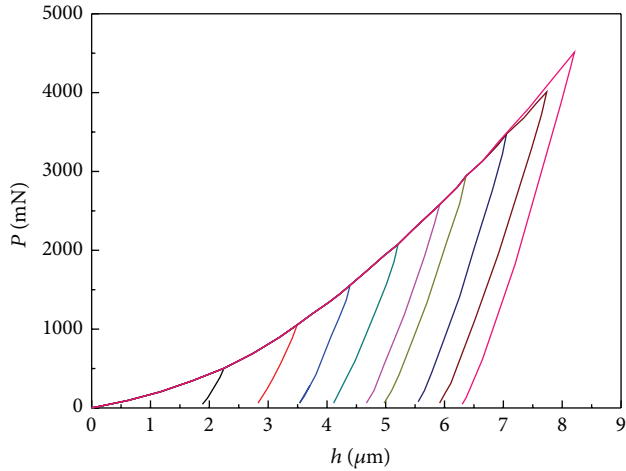


FIGURE 5: P - h curves of (405) under velocity of 17.284 mN/s.

plastic flow generated by the high density of dislocation nucleation and propagation is observed in microindentation [48]. Based on these curves, micromechanical parameters (H , E , σ_y , σ_b , and n) can be obtained according to equations mentioned in Section 2.

Based on (24), microhardness of four different crystal planes ((001), (215), (405), and (605)) has been calculated. The results are shown in Figure 6.

It can be seen from Figure 6 that H of each crystal plane under different velocities is almost the same although data of (001) with 51.8527 mN/s derives from others slightly, which indicates that microindentation loading velocities had little influence on the results of H . And the similar phenomenon was founded in Ti-6Al-4V alloy [49]. Therefore, loading velocity of 17.2842 mN/s was used in the following investigation. H of different crystal planes corresponding to 17.2842 mN/s was shown in Figure 7.

According to Figure 7, H of four crystal planes evidently decreases with the increase of maximum load. The phenomenon that indentation depth increases with increase of maximum load confirms the reduction of H . In addition, the apparent drop of H occurs when the loads are less than 2000 mN. When loads are above 2000 mN, their values reduce up to 8%. This phenomenon is attributed to indentation size effects (ISE) caused by geometrically necessary dislocations (GNDs). At the micro/nanoscales, GNDs are large enough and arranged periodically and regularly to cause strong obstacles to slip. GNDs have a strengthening effect on hardness and enhance indurations of material [50]. But values of GNDs have a decreasing tendency with the increase of h , which can be demonstrated by the equation of density of GNDs (ρ_G) for a Berkovich indenter:

$$\rho_G = \frac{3 \tan^2 \theta}{2bh}, \quad (25)$$

where θ is the angle between surface of the indenter and plane of the surface with the value of 19.7° for Berkovich indenter [27].

Moreover, Nix and Gao proposed a new model of H and h , based on Taylor dislocation and geometrically necessary dislocation model [43, 51]:

$$\frac{H}{H_0} = \sqrt{1 + \frac{h^*}{h}}, \quad (26)$$

where h^* is a length that characterizes the depth dependence of hardness:

$$H_0 = 3\sqrt{3}\alpha\mu b\sqrt{\rho_S}, \quad (27)$$

$$h^* = \frac{81}{2}b\alpha^2 \tan^2 \theta \left(\frac{\mu}{H_0} \right)^2, \quad (28)$$

where α is a constant, whose value is 0.3–0.5.

According to (26) and (27), one can find that when P is low, h is of small value correspondingly. Thus ρ_G of region under indenter is considerable and the measured values of H are large. When load is relatively higher, ρ_G is in a lower amount and its hardening effect is relatively small on H , when H remains almost stable.

As for each crystal plane, H of (001) is close to that of (405), while it is higher than those of (215) and (605). (405) has the largest values of H , followed by (001) and (215), which can be explained by dislocation hardening mechanism. It is well known that there are four mechanisms existing in metallic: solid solution hardening, dislocation hardening, boundary hardening, and precipitation hardening. In this paper, single crystal that has no crystal boundary was investigated and the solid solution and precipitation hardening can be ascribed to dislocation movement. Therefore, dislocation hardening is the dominant factor on H . In the literature, the density equation of dislocation (ρ) has been proposed:

$$\rho = \frac{3 \tan^2 \theta}{2b} \left(\frac{1}{h} + \frac{1}{h^*} \right). \quad (29)$$

The statistically stored dislocations density on four crystal planes can be calculated through (29), as shown in Figure 8. It can be seen that (001) has the largest dislocation density among these crystal planes, and second for (405), the lowest for (215). Compared with H of four crystal planes in Figure 7, it is reasonable that H of (605) and (215) is lower than those of other two planes. Because dislocation density is lower, hardening effect caused by dislocation is weaker. However, with regard to H of (001) and (405), H of (405) is larger than that of (001), although ρ of (001) is higher. This phenomenon can be explained by the following facts. For metallic materials with FCC crystal structure, slip easily takes place on the close-packed $\{111\}$ octahedral planes and in the $\langle 110 \rangle$ close-packed directions. Generally, for FCC lattice there are four slip planes and three corresponding slip directions, namely, posing twelve slip systems. But there are eight equivalent $\{111\}$ $\langle 110 \rangle$ slip systems on (001) planes, while there is only one equivalent slip system on (405), (605), and (215). Compared with (405), dislocation may extend through different slip systems and hardly pile up due to more slip systems on (001). Therefore, H of (001) is a little lower than that of (405).

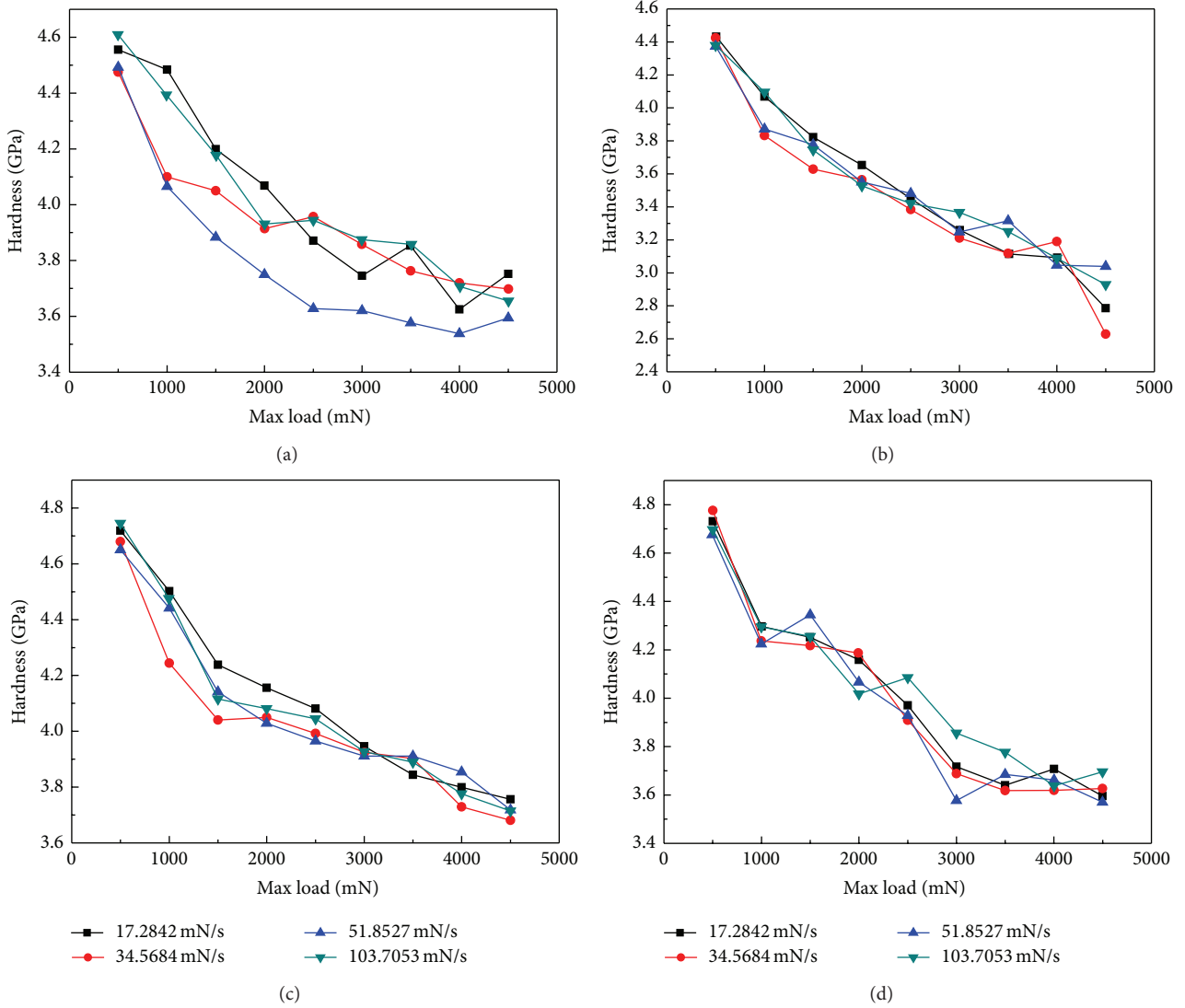


FIGURE 6: Microhardness H of different crystal planes under different velocities: (a) (001); (b) (215); (c) (405); (d) (605).

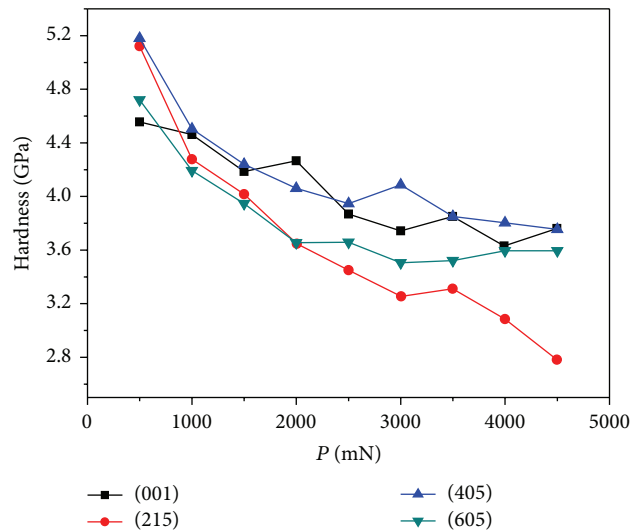


FIGURE 7: H of different crystal planes under 17.2842 mN/s.

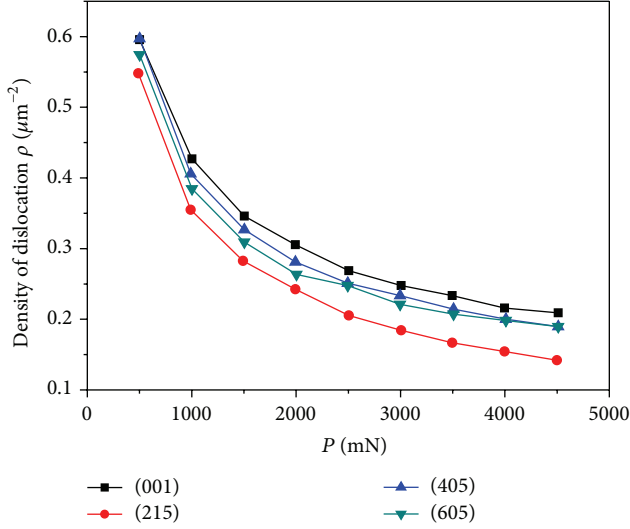


FIGURE 8: Density of dislocation density ρ of four crystal planes.

4.2. *Young's Modulus E.* Of the various unique mechanical properties of materials, Young's modulus, which is a measure of elasticity, has attracted particular attention. Figure 9 shows Young's modulus of four different crystal planes ((001), (215), (405), and (605)) calculated according to (6).

It can be seen from Figure 9 that the calculated E of each crystal plane under different velocities has similar values, illustrating that microindentation loading speeds had little influence on the results of E . And the similar phenomenon was also found in Ti-6Al-4V alloy [49]. Therefore, loading speed with value of 17.2842 mN/s was used for the following investigation.

Figure 10 gives the values of E from different crystal planes under the loading speed of 17.2842 mN/s. As shown in Figure 10, it can be concluded that E decreases with the increase of h on the whole.

Compared with H of the same planes, E also decreases rapidly with loads below 2000 mN. And its values remain almost the same when subjected to the higher loads. The induced damage is responsible for this phenomenon. The reduction of Young's modulus is typically regarded as a characterization of damage evolution and accumulation. When dislocations accumulate or pile up in a certain region, it is easy for stress to concentrate and eventually surpass its threshold. Thus, damage can be easily generated and extended under indentation load, resulting in elastic properties weakening and E decreasing. In addition, when loads are below 2000 mN, each of E curves falls quickly due to the high values of ρ (Figure 8) and the corresponding rapid damage accumulation. However, when the loads are around 4000 mN, fluctuation of ρ is steady and has no obvious effect on variation of E .

For each crystal plane, E of (001) is larger than others and (215) has the lowest value. Crystalline structure and theory of metallic plasticity contribute qualitatively to the explanation of diverse E from different crystal plane. For example, for

cubic system, the expression for the interplanar spacing (d) is as follows:

$$\frac{1}{d^2} = \frac{j^2 + k^2 + l^2}{a^2}, \quad (30)$$

where a is 0.358 nm for DD99.

According to (30), the interplanar spacing of (001), (215), (405), and (605) is 0.358 nm, 0.0703 nm, 0.06 nm, and 0.0493 nm, respectively. The greater the interplanar spacing is, the larger the density of atoms on this crystal plane is. The greater interplanar spacing is significantly efficient in driving the movement of atoms on the crystal plane, which poses a larger E . However, this explanation does not work for (405) in comparison with that of (215); this phenomenon needs further research.

According to theory of metallic plasticity, the crystal E can be also obtained through stiffness coefficient and crystal indices [52]. For cubic system, E can be calculated as the following equation:

$$\frac{1}{E} = S_{11} - 2S_A \frac{(jk)^2 + (jl)^2 + (kl)^2}{(j^2 + k^2 + l^2)}, \quad (31)$$

$$S_A = S_{11} - S_{12} - \frac{S_{44}}{2}.$$

For the same material, E with different crystal orientation and planes mainly depends on

$$\frac{[(jk)^2 + (jl)^2 + (kl)^2]}{(j^2 + k^2 + l^2)^2}. \quad (32)$$

For crystal nickel-based DD99, value of S_A is negative. According to (32), the value of (001) is 0, which is the smallest one among four crystal planes, while (605) is having the largest data of 0.24187. So (001) has the largest E , but E of (605) is relatively lower.

4.3. *Elastic-Plastic Constitutive Model.* According to equations in Section 2.1, the values of σ_y and n of (405) under different loads are shown in Figure 11. It is evident that they remain constant regardless of the different loads.

As shown in Figure 12, values of σ_y and n are shown in bar graph. It can be found that σ_y of (215) is the largest, followed successively by (605) and (001). However, the values of n show the opposite tendency. That is, n of (215) is the lowest, followed by (605), and that of (001) is the largest.

It is well known that σ_y is the strength assessing the ability to resist the plastic deformation. And for materials with power hardening law, n is used as a parameter evaluating a kind of ability that maintains homogeneous deformation. The higher n of certain material, the better compatibility of deformation of material. The differences of σ_y on four crystal planes can be explained by Schmid's law.

In Figure 13, a typical uniaxial tensile stress σ exerted on a metal cylinder is shown. A_0 is the area normal to the axial force F and A_1 is the area of the slip plane on which the resolved shear force F_r is acting. ϕ is the angle

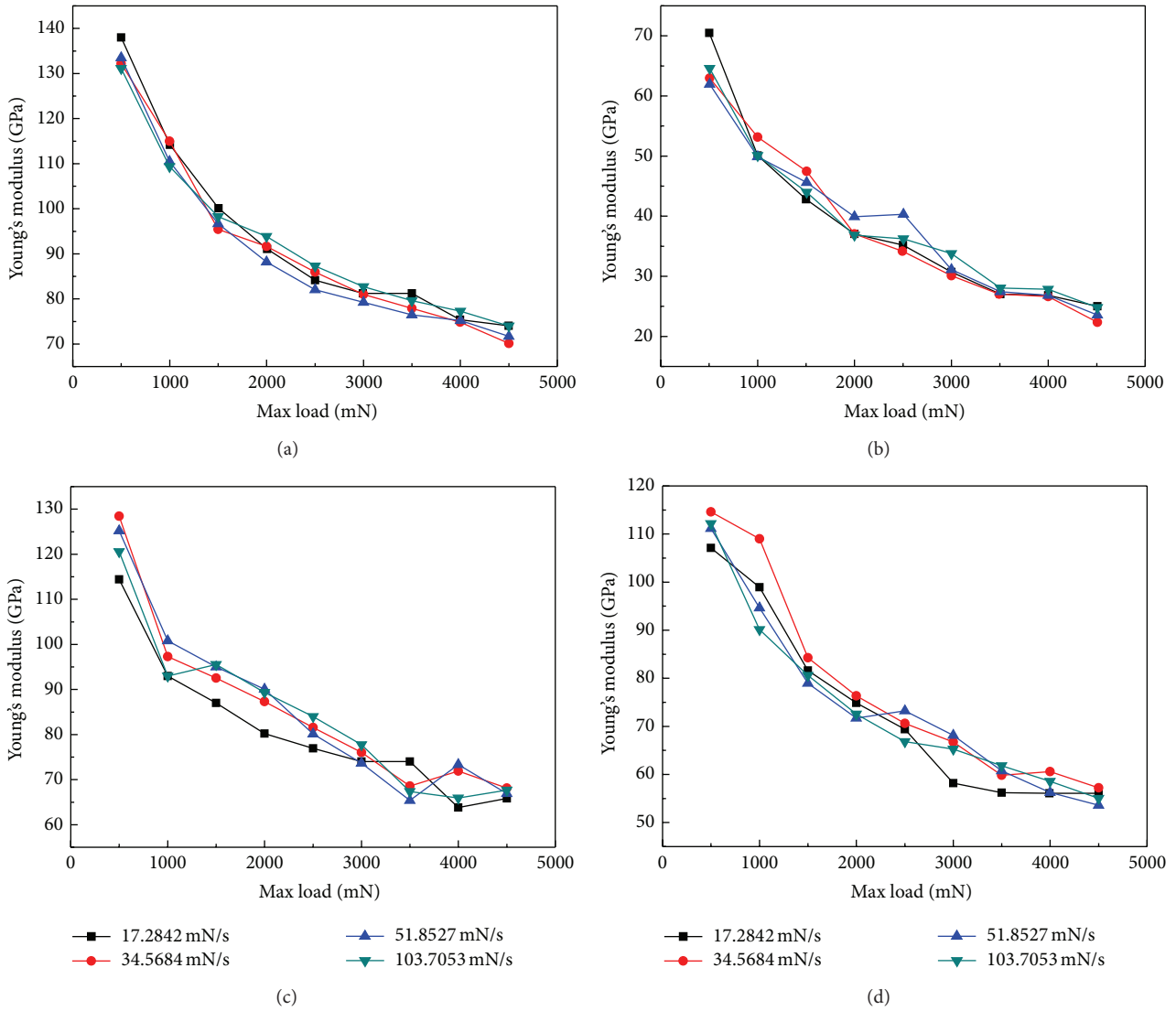


FIGURE 9: Young's modulus E of different crystal planes under different speeds: (a) (001); (b) (215); (c) (405); (d) (605).

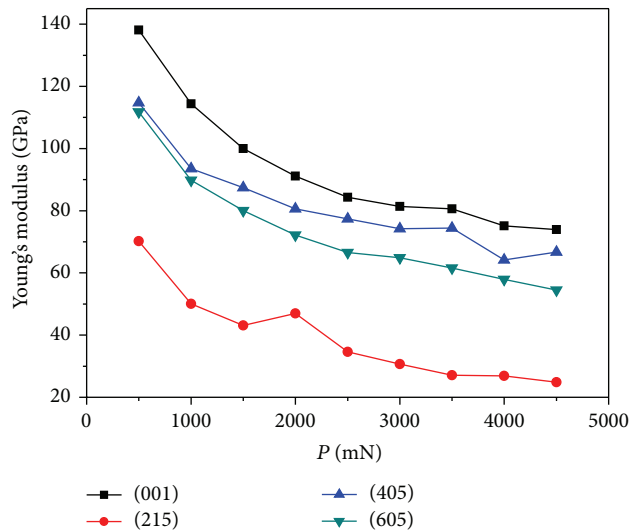


FIGURE 10: E of different crystal planes under 17.2842 mN/s.

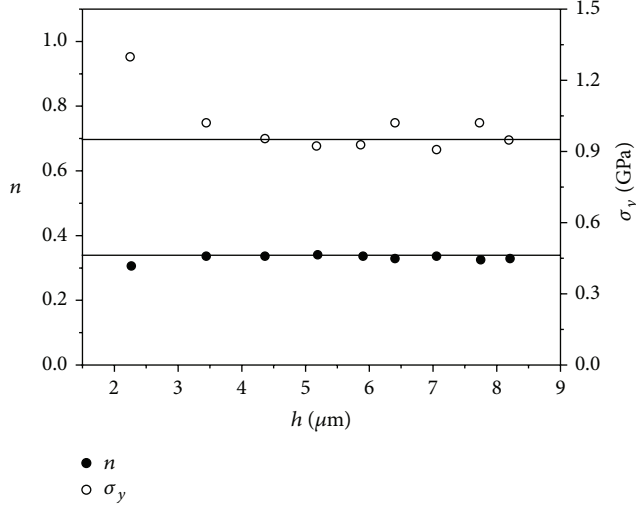


FIGURE 11: Values of σ_y and n at different indentation depths h of (405).

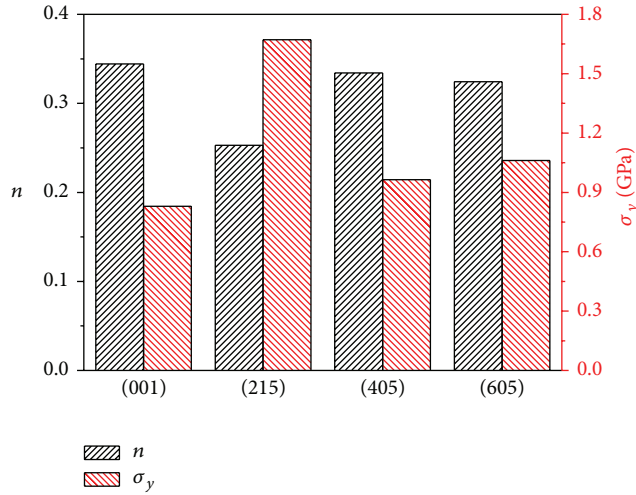


FIGURE 12: σ_y and n of four different crystal planes.

between F and the normal to the slip plane area A_1 , and λ is the angle between F and the slip direction. For activating dislocations to move in the slip system, a sufficient resolved shear stress (τ_r) in the slip direction must be produced, and τ_r is computed as

$$\tau_r = \frac{F_r}{A_1} = \frac{F \cos \lambda}{A_0 / \cos \phi} = \frac{F}{A_0} \cos \lambda \cos \phi = \sigma \cos \lambda \cos \phi. \quad (33)$$

This is called Schmid's law. m is called Schmid factor and defined as follows:

$$m = \cos \lambda \cos \phi. \quad (34)$$

m , σ_y , and n are shown in Table 3.

τ_r is a constant for a previous known lattice, and independent of the orientation of F , it can be inferred that σ is larger,

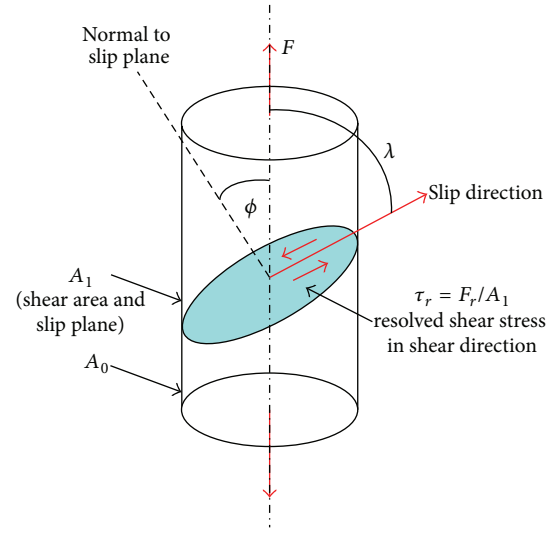


FIGURE 13: Schematic diagram of uniaxial tension model.

TABLE 3: m , σ_y , and n of different crystal planes.

Crystal indices	n	σ_y (GPa)	m
(001)	0.3449	0.8248	0.408
(215)	0.2529	1.6701	0.435
(405)	0.3338	0.9667	0.448
(605)	0.3242	1.0585	0.442

if m is smaller according to (33) and (34). Therefore, the fact that σ of (215) is larger than that of (605), which is followed by (405), can be understandable, because m of (215), (605), and (405) increases sequentially. With particular emphasis on m of (001) which is the lowest, it has eight equivalent $\{111\}$ $\langle 110 \rangle$ slip systems, while there is only one equivalent slip system on (405), (605), and (215). For FCC single-crystal structure, Schmid's law is no longer valid, regardless of potential slip systems. When value and orientation of F are appropriate, τ_r of two or more slip systems can be achieved, which makes the situation complicated, and Schmid law does not work anymore.

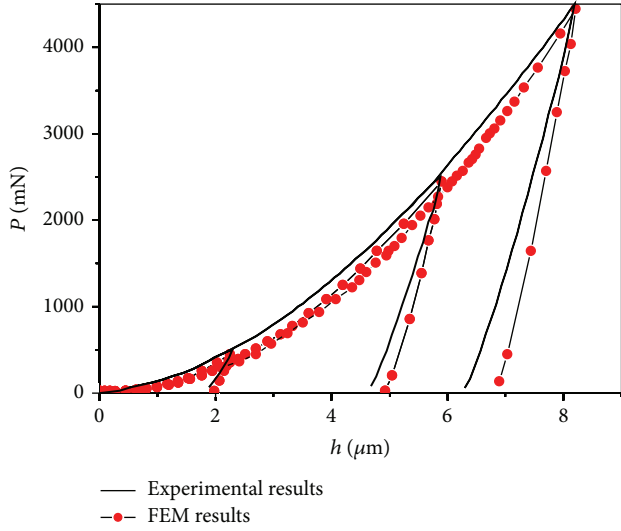
For (001) crystal having eight equivalent $\{111\}$ $\langle 110 \rangle$ slip systems and a relatively lower σ_y , the dislocations can extend easily and the deformation resistance is low, resulting in better compatibility of uniform deformation. So, it has the largest n . With regard to (215), (605) and (405) who yield only one equivalent slip system, the yield strength decrease in order, namely, compatibility of deformation of (405) is the best, followed by (605). And that of (215) is the worst of all. Therefore, n of (405) is larger than that of (605).

Based on (2) and (23), R and σ_b along with other parameters representing elastic-plastic properties can be obtained in Table 4.

Mechanical property parameters, E , R , n , and σ_y , were obtained from microindentation experimental data; thus the

TABLE 4: Elastic-plastic properties parameters.

Crystal indices	R	n	σ_y (GPa)	σ_b (GPa)
(001)	3.8941	0.3449	0.8248	1.9110
(215)	3.3090	0.2529	1.6701	1.8150
(405)	3.9661	0.3338	0.9667	1.9694
(605)	3.8123	0.3242	1.0585	1.9133

FIGURE 14: Experimental versus computed P - h curves of 500 mN, 2500 mN, and 4500 mN on (405).

elastic-plastic equations of DD99 on different crystal planes can be obtained as

$$\begin{aligned}
 \text{Crystal plane (001)} \quad \sigma &= \begin{cases} 137.9\varepsilon, & \sigma \leq 824.8 \\ 3.8941\varepsilon^{0.3449}, & \sigma \geq 824.8, \end{cases} \\
 \text{Crystal plane (215)} \quad \sigma &= \begin{cases} 70.332\varepsilon, & \sigma \leq 1670.1 \\ 3.309\varepsilon^{0.2529}, & \sigma \geq 1670.1, \end{cases} \\
 \text{Crystal plane (405)} \quad \sigma &= \begin{cases} 114.3465\varepsilon, & \sigma \leq 966.7 \\ 3.9661\varepsilon^{0.3338}, & \sigma \geq 966.7, \end{cases} \\
 \text{Crystal plane (605)} \quad \sigma &= \begin{cases} 112.414\varepsilon, & \sigma \leq 1058.5 \\ 3.8123\varepsilon^{0.3242}, & \sigma \geq 1058.5. \end{cases} \quad (35)
 \end{aligned}$$

5. Verification of Elastic-Plastic Model

Simulation calculations have been performed by using the commercial finite element software ABAQUS. The experimental and FEM results of 500 mN, 2500 mN, and 4500 mN on crystal plane (405) were shown in Figure 14. The experimental curves agreed well with computed P - h curves, which indicates that above elastic-plastic equations of DD99 obtained by MIT are valid and 3D FEM model of indentation can fully describe and simulate microindentation process.

Although FEM results deviate from experimental results slightly, it is of great importance to focus on their difference.

In order to illustrate cause of deviation to achieve better simulations in the future, experimental and FEM results of 2500 mN on different crystal planes were shown in Figure 15.

As shown in Figure 15, it can be concluded that FEM results seem like experimental data moving right. To be more specific, FEM results have various degrees of deviation from experimental results during the loading process, especially in the middle process of the loading. This phenomenon can be explained by Kick's law (Equation (4)) and decrease of E along with increase of h .

There is a relationship between H and σ_y , originally suggested by Tabor [53]:

$$H = C_\theta \sigma_y, \quad (36)$$

According to (9) and (24), P_m can be expressed as follows:

$$P_m = \omega \sigma_y h_m^2, \quad (37)$$

where ω is a constant.

Therefore, Kick's law seems to be reasonable. However, microindentation test is not an ideal plastic deformation process. ISE exists in the process of microindentation as discussed above, resulting in decrease of H . As H is the function of h shown in (26), σ_y is also a function of h according to (37). And the relationship between P_m and h is no longer quadratic function. When the load is low, ISE is obvious [54] and error of results from Kick's law is larger compared with those under high load. In order to prove it, the experimental and FEM results of (405) under 500 mN and 2500 mN were utilized, as shown in Figure 16. Besides, the lower load yields a poor accuracy between simulated and experimental results in comparison with the higher load, which may be due to the transition of contact modes from purely elastic under lower loads to elastic/plastic under higher loads. Jian et al. [22, 55, 56] have maintained that the behaviors during indentation can be roughly divided into two stages by the variation of microhardness. Namely, the hardness initially increases with the penetration depth due to the transition between purely elastic and elastic/plastic contact.

Also the decrease of E along with increase of h may also be blamed for the difference between experimental and FEM results. In FEM model, the selection of E is a complicated question. As shown in Figure 10, E of four crystal planes decreases with the increase of h due to damage, E actually changes a little with high load, and the value of E with high load is used in FEM model. In the preliminary stage of indentation, E of materials is higher than that used in FEM model. According to stress-strain relationship in the elastic stage, the higher ε is corresponding to the smaller E . So h of FEM is larger than that of experimental data.

With regard to unloading process, the slope of unloading curve is related with E according to (13). And it can be found that all the unloading curves of FEM results are parallel to that of experimental data (Figure 15), indicating that the difference of unloading process is attributed to the error of h in loading process and the selection of E in FEM model is reasonable.

In order to interpret the matching degree of P - h curves in FEM results and experimental data quantitatively, the predictability of the applied load is further quantified employing

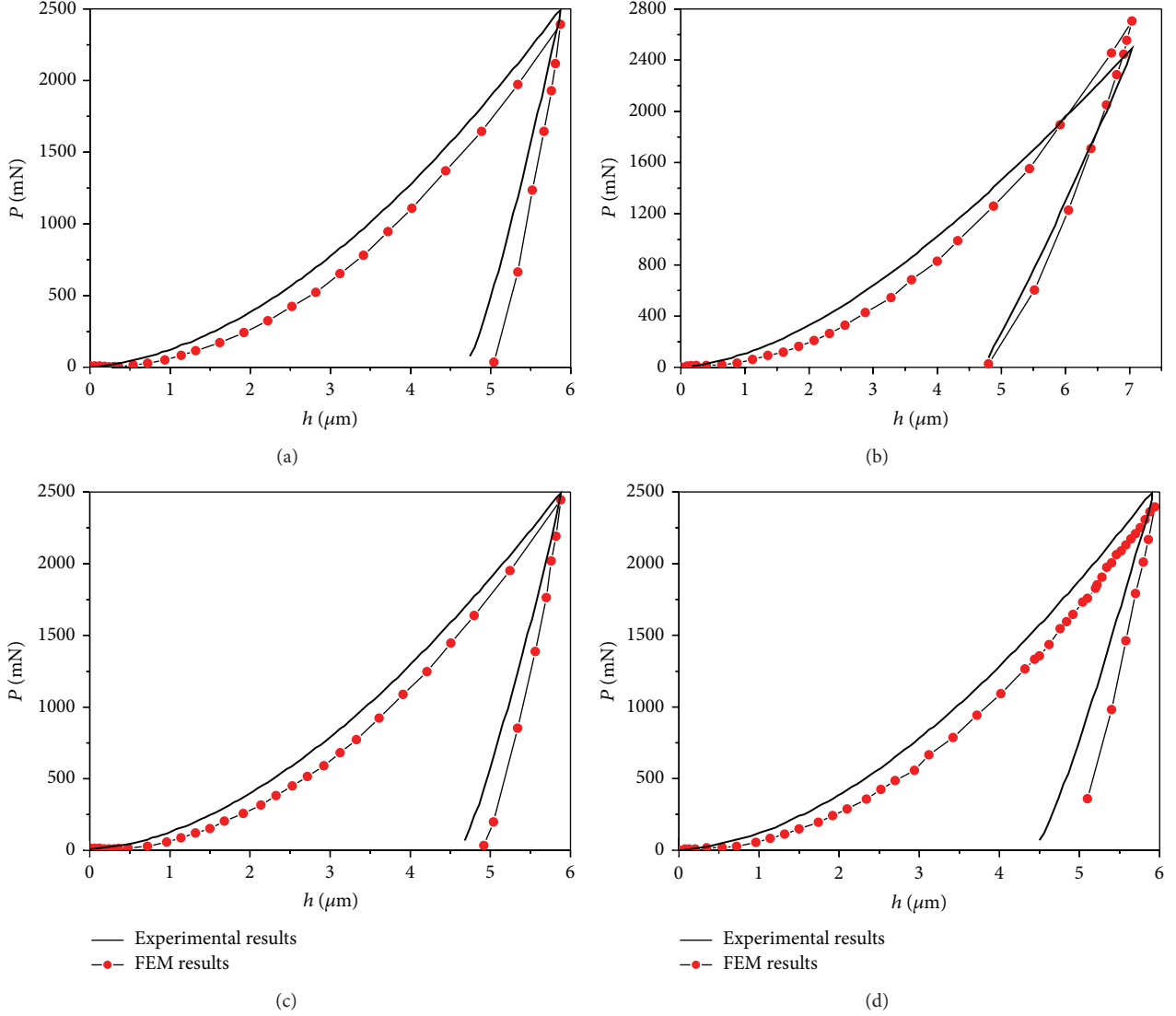


FIGURE 15: Experimental and FEM results of 2500 mN on different crystal planes: (a) (001); (b) (215); (c) (405); (d) (605).

standard statistical parameters correlation coefficient (U). U was a commonly used statistic and provides information on the dispersion between the experimental and the computed values. It was expressed as [57, 58]

$$U = \frac{\sum_{i=1}^N (P_{\text{exp}}^i - \bar{P}_{\text{exp}})(P_p^i - \bar{P}_p)}{\sqrt{\sum_{i=1}^N (P_{\text{exp}}^i - \bar{P}_{\text{exp}})^2 \sum_{i=1}^N (P_p^i - \bar{P}_p)^2}}, \quad (38)$$

where P_{exp} is the experimental indenter load, P_p is the predicted indenter load, and \bar{P}_{exp} and \bar{P}_p are the mean values of P_{exp} and P_p , respectively.

According to literature [59], the predictability of the matching degree of P - h curves can also be quantified by the

average absolute relative error (AARE) and the results of U and AARE are as shown in Table 5:

$$\text{AARE} (\%) = 100 \times \frac{1}{N} \sum_{i=1}^N \left| \frac{P_{\text{exp}}^i - P_p^i}{P_{\text{exp}}^i} \right|. \quad (39)$$

6. Conclusions

Microindentation measurements using a sharp Berkovich indenter on single-crystal nickel-based superalloy DD99 of four crystallographic orientations, that is, (001), (215), (405), and (605), were made to determine the load-displacement relations. Some material parameters reflecting the micromechanical behavior of DD99, such as microhardness H , Young's modulus E , yield stress σ_y , strain hardening component n , and tensile strength σ_b , can be obtained from load-displacement relations. Subsequently, the process of MIT is simulated using 3D FEM based on the above parameters.

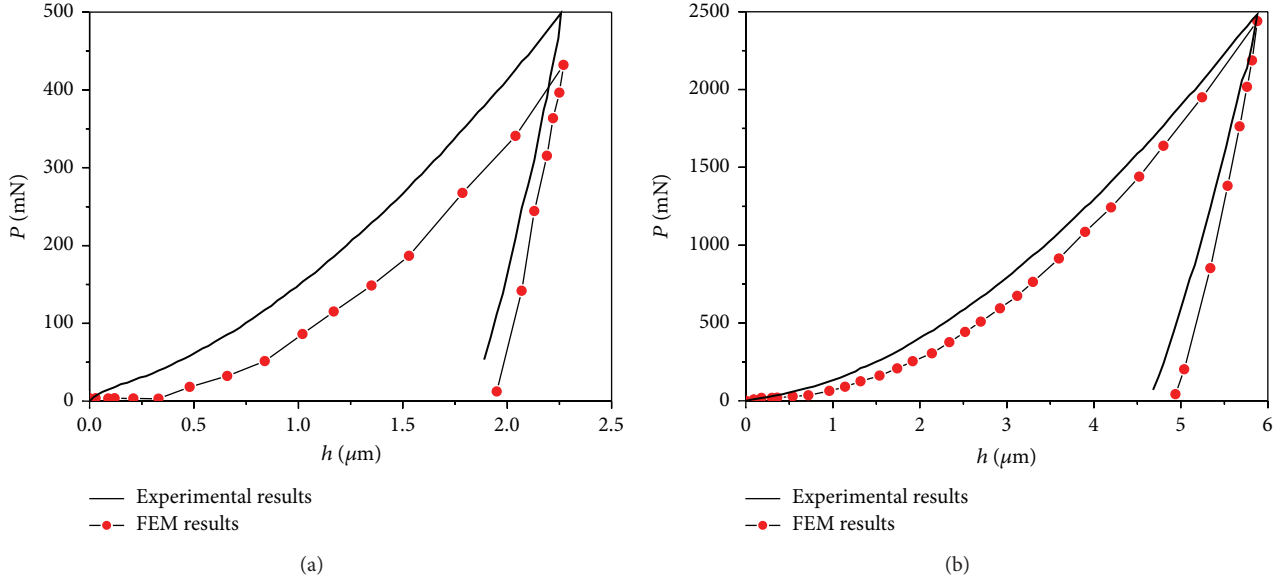


FIGURE 16: Experimental and FEM results of (405) with different loads: (a) 500 mN; (b) 2500 mN.

TABLE 5: Error analysis of four different crystal planes.

Crystal indices	Correlation coefficient U	Average absolute relative error (AARE %)
(001)	0.9884	15%
(215)	0.9914	14%
(405)	0.99024	14.3%
(605)	0.992515	12.8%

Eventually, the influence of crystal orientations on micromechanical properties can be concluded as follows.

- (1) H of four different crystal planes evidently decreases with the increase of h . The crystal plane (405) has the largest micro-hardness values, followed by (001). H of (215) is the lowest. This phenomenon is related to dislocation hardening.
- (2) E of these planes decreases with the increase of h . (001) has the largest E , followed by (405). And E of (215) is the lowest, which is attributed to the fact that (001) has the largest interplanar spacing and smallest crystal variable.
- (3) n is inversely correlated with σ_y on all these planes. σ_y of (215) is the largest among four crystal planes, followed by (605), and (001) has the lowest value. However, n of (215) is the lowest, followed by (605), and that of (001) is the largest. It can be explained by Schmid's factor (m) and the larger m crystal plane has and the lower σ_y it possesses. In addition, σ_b on four planes was calculated and it is similar except for (215).

Although FEM results deviate slightly from experimental results, they can be used as sufficient evidences indicating the

accuracy of 3D FEM model and material elastic-plastic model founded from MIT.

Nomenclature

A :	Cross-sectional area, mm^2
A_b :	Cross-sectional area corresponding to σ_b , mm^2
a :	Lattice constant
B and t :	Fitting coefficients
b :	Burgers vector
C :	A variable related to material properties as well as indenter geometry
C_θ :	Constraint factor
E :	Elastic modulus, MPa
E^* :	Effective elastic modulus of damaged material, MPa
H :	Microhardness, $\text{kg}\cdot\text{mm}^{-2}$
H_0 :	microhardness regardless of strain gradient plasticity, $\text{kg}\cdot\text{mm}^{-2}$
h :	Indenter displacement, μm
h_f :	Residual depth after unloading, μm
h, k , and l :	Miller indices
m :	Schmid factor
n :	Strain hardening exponent
P :	Indenter load, mN
R :	Strength coefficient
S_{11} , S_{12} , and S_{44} :	Independent elastic compliance constant.

Greek Letters

ε :	True strain
ε_y :	Corresponding strain to initial yield stress
ε_b :	Strain corresponding to σ_b

σ_y : Initial yield stress, MPa
 σ_c : Representative stress, MPa
 σ_b : Ultimate tensile strength, MPa
 $\bar{\sigma}$: Flow stress, MPa
 ν : Poisson's ratio
 μ : Shear modulus, MPa
 ρ_S : Density of statistically stored dislocations.

Conflict of Interests

The authors declare that there is no conflict of interests regarding the publication of this paper.

Acknowledgments

The authors would like to express their sincere thanks for the research grants supported by the National Natural Science Foundation of China (Grant no. 51275414), the Aeronautical Science Foundation of China (Grant no. 2011ZE53059), and the Graduate Starting Seed Fund of Northwestern Polytechnic University (Grant no. Z2014007).

References

- [1] G. L. Erickson, "Single crystal nickel-based superalloy," Google Patents, 1994.
- [2] A. Sato, Y.-L. Chiu, and R. C. Reed, "Oxidation of nickel-based single-crystal superalloys for industrial gas turbine applications," *Acta Materialia*, vol. 59, no. 1, pp. 225–240, 2011.
- [3] C. Lane, "Introduction," in *The Development of a 2D Ultrasonic Array Inspection for Single Crystal Turbine Blades*, Springer Theses, pp. 1–12, Springer, 2014.
- [4] J.-J. Yu, X.-F. Sun, N.-R. Zhao, T. Jin, H.-R. Guan, and Z.-Q. Hu, "Effect of carbon on microstructure and mechanical properties of DD99 single crystal superalloy," *Transactions of Nonferrous Metals Society of China*, vol. 16, pp. 1973–1977, 2006.
- [5] Z.-H. Yu, L. Liu, X.-B. Zhao, W.-G. Zhang, J. Zhang, and H.-Z. Fu, "Advance in research of carbon effect on single crystal Ni-base superalloy," *Foundry*, vol. 58, no. 9, p. 10, 2009.
- [6] T.-B. Wu, X.-F. Yu, Y.-L. Man et al., "Burning loss of carbon and influence factors of oxygen content during vacuum induction melting," *Foundry*, vol. 62, no. 1, pp. 1–3, 2013.
- [7] J. S. Wan and Z. F. Yue, "A low-cycle fatigue life model of nickel-based single crystal superalloys under multiaxial stress state," *Materials Science and Engineering A*, vol. 392, no. 1-2, pp. 145–149, 2005.
- [8] H. U. Hong, J. G. Yoon, B. G. Choi, I. S. Kim, and C. Y. Jo, "On the mechanism of secondary reaction zone formation in a coated nickel-based single-crystal superalloy containing ruthenium," *Scripta Materialia*, vol. 69, no. 1, pp. 33–36, 2013.
- [9] D. Shi, C. Dong, and X. Yang, "Constitutive modeling and failure mechanisms of anisotropic tensile and creep behaviors of nickel-base directionally solidified superalloy," *Materials & Design*, vol. 45, pp. 663–673, 2013.
- [10] P. Caron, T. Khan, Y. Ohta, and Y. Nakagawa, "Creep deformation anisotropy in single crystal superalloys," in *Superalloys 1988*, pp. 215–224, TMS, Warrendale, Pa, USA, 1988.
- [11] M. He, H. Li, and J. Nie, "An investigation on creep/fatigue damage characteristics of single-crystal DD6 at high temperature," *Gas Turbine Experiment and Research*, vol. 15, no. 2, pp. 24–27, 2002.
- [12] J. Z. Yi, C. J. Torbet, Q. Feng, T. M. Pollock, and J. W. Jones, "Ultrasonic fatigue of a single crystal Ni-base superalloy at 1000 °C," *Materials Science and Engineering A*, vol. 443, no. 1-2, pp. 142–149, 2007.
- [13] X. Wu, J. H. Zhang, J. L. Liu, T. Jin, Y. B. Xu, and Z. Q. Hu, "Plastic deformation inhomogeneity in a single crystal nickel-base superalloy," *Materials Science and Engineering A*, vol. 325, no. 1-2, pp. 478–483, 2002.
- [14] S. L. Semiatin and T. R. Bieler, "The effect of alpha platelet thickness on plastic flow during hot working of Ti-6Al-4V with a transformed microstructure," *Acta Materialia*, vol. 49, no. 17, pp. 3565–3573, 2001.
- [15] M. Jamal and M. Morgan, "Determination of the mechanical properties of thermally treated recycled glass based on nano-indentation measurement and FEM supported simulation," *Key Engineering Materials*, vol. 581, pp. 472–477, 2014.
- [16] W. B. Lee and Y. P. Chen, "Simulation of micro-indentation hardness of FCC single crystals by mechanism-based strain gradient crystal plasticity," *International Journal of Plasticity*, vol. 26, no. 10, pp. 1527–1540, 2010.
- [17] L. Wang, X. H. Zhong, J. S. Yang et al., "Finite element simulation of surface micro-indentation behavior of yttria stabilized zirconia thermal barrier coatings with microstructural characteristic of columnar grains and sub-grains based on a nonlinear contact model," *Computational Materials Science*, vol. 82, pp. 244–256, 2014.
- [18] W. Z. Yao, C. E. Krill III, B. Albinski, H.-C. Schneider, and J. H. You, "Plastic material parameters and plastic anisotropy of tungsten single crystal: a spherical micro-indentation study," *Journal of Materials Science*, vol. 49, no. 10, pp. 3705–3715, 2014.
- [19] Y. Y. Lim and M. Munawar Chaudhri, "The influence of grain size on the indentation hardness of high-purity copper and aluminium," *Philosophical Magazine A*, vol. 82, no. 10, pp. 2071–2080, 2002.
- [20] Y. Liu, S. Varghese, J. Ma, M. Yoshino, H. Lu, and R. Komanduri, "Orientation effects in nanoindentation of single crystal copper," *International Journal of Plasticity*, vol. 24, no. 11, pp. 1990–2015, 2008.
- [21] M. C. Fivel, C. F. Robertson, G. R. Canova, and L. Boulanger, "Three-dimensional modeling of indent-induced plastic zone at a mesoscale," *Acta Materialia*, vol. 46, no. 17, pp. 6183–6194, 1998.
- [22] S.-R. Jian, J.-Y. Juang, C.-W. Luo, S.-A. Ku, and K.-H. Wu, "Nanomechanical properties of GaSe thin films deposited on Si(1 1 1) substrates by pulsed laser deposition," *Journal of Alloys and Compounds*, vol. 542, pp. 124–127, 2012.
- [23] W. C. Oliver and G. M. Pharr, "Improved technique for determining hardness and elastic modulus using load and displacement sensing indentation experiments," *Journal of Materials Research*, vol. 7, no. 6, pp. 1564–1580, 1992.
- [24] G. M. Pharr, W. C. Oliver, and F. R. Brotzen, "On the generality of the relationship among contact stiffness, contact area, and elastic modulus during indentation," *Journal of Materials Research*, vol. 7, no. 3, pp. 613–617, 1992.
- [25] N. Janakiraman and F. Aldinger, "Indentation analysis of elastic and plastic deformation of precursor-derived Si-C-N ceramics," *Journal of the European Ceramic Society*, vol. 30, no. 3, pp. 775–785, 2010.
- [26] R. B. King, "Elastic analysis of some punch problems for a layered medium," *International Journal of Solids and Structures*, vol. 23, no. 12, pp. 1657–1664, 1987.
- [27] M. He, F. Li, J. Cai, and B. Chen, "An indentation technique for estimating the energy density as fracture toughness with

- Berkovich indenter for ductile bulk materials," *Theoretical and Applied Fracture Mechanics*, vol. 56, no. 2, pp. 104–111, 2011.
- [28] J. Li, F. Li, M. He, F. Xue, M. Zhang, and C. Wang, "Indentation technique for estimating the fracture toughness of 7050 aluminum alloy with the Berkovich indenter," *Materials and Design*, vol. 40, pp. 176–184, 2012.
- [29] Y.-T. Cheng and C.-M. Cheng, "Relationships between hardness, elastic modulus, and the work of indentation," *Applied Physics Letters*, vol. 73, no. 5, pp. 614–616, 1998.
- [30] Y.-T. Cheng and C.-M. Cheng, "Scaling approach to conical indentation in elastic-plastic solids with work hardening," *Journal of Applied Physics*, vol. 84, no. 3, pp. 1284–1291, 1998.
- [31] Y.-T. Cheng and C.-M. Cheng, "Can stress-strain relationships be obtained from indentation curves using conical and pyramidal indenters?" *Journal of Materials Research*, vol. 14, no. 9, pp. 3493–3496, 1999.
- [32] Y.-T. Cheng and C.-M. Cheng, "Relationships between initial unloading slope, contact depth, and mechanical properties for conical indentation in linear viscoelastic solids," *Journal of Materials Research*, vol. 20, no. 4, pp. 1046–1053, 2005.
- [33] K. Tunvisut, N. P. O'Dowd, and E. P. Busso, "Use of scaling functions to determine mechanical properties of thin coatings from microindentation tests," *International Journal of Solids and Structures*, vol. 38, no. 2, pp. 335–351, 2001.
- [34] M. Dao, N. Chollacoop, K. J. van Vliet, T. A. Venkatesh, and S. Suresh, "Computational modeling of the forward and reverse problems in instrumented sharp indentation," *Acta Materialia*, vol. 49, no. 19, pp. 3899–3918, 2001.
- [35] J.-Y. Kim, K.-W. Lee, J.-S. Lee, and D. Kwon, "Determination of tensile properties by instrumented indentation technique: representative stress and strain approach," *Surface and Coatings Technology*, vol. 201, no. 7, pp. 4278–4283, 2006.
- [36] X.-L. Gao, "New expanding cavity model for indentation hardness including strain-hardening and indentation size effects," *Journal of Materials Research*, vol. 21, no. 5, pp. 1317–1326, 2006.
- [37] H. Yuan and J. Chen, "Identification of the intrinsic material length in gradient plasticity theory from micro-indentation tests," *International Journal of Solids and Structures*, vol. 38, no. 46–47, pp. 8171–8187, 2001.
- [38] H. Yuan and J. Chen, "The role of intrinsic material length scales in micro-indentation simulations," *Computational Materials Science*, vol. 25, no. 1–2, pp. 253–263, 2002.
- [39] R. K. A. Al-Rub and G. Z. Voyiadjis, "Analytical and experimental determination of the material intrinsic length scale of strain gradient plasticity theory from micro- and nano-indentation experiments," *International Journal of Plasticity*, vol. 20, no. 6, pp. 1139–1182, 2004.
- [40] R. K. Abu Al-Rub and G. Voyiadjis, "Determination of the material intrinsic length scale of gradient plasticity theory," *International Journal for Multiscale Computational Engineering*, vol. 2, no. 3, 24 pages, 2004.
- [41] G. Z. Voyiadjis and R. A. Al-Rub, "Determination of the material intrinsic length scale of gradient plasticity theory," in *IUTAM Symposium on Multiscale Modeling and Characterization of Elastic-Inelastic Behavior of Engineering Materials*, vol. 114 of *Solid Mechanics and Its Applications*, pp. 167–174, Springer, Dordrecht, The Netherlands, 2004.
- [42] S. Shim, J.-I. Jang, and G. M. Pharr, "Extraction of flow properties of single-crystal silicon carbide by nanoindentation and finite-element simulation," *Acta Materialia*, vol. 56, no. 15, pp. 3824–3832, 2008.
- [43] W. D. Nix and H. Gao, "Indentation size effects in crystalline materials: a law for strain gradient plasticity," *Journal of the Mechanics and Physics of Solids*, vol. 46, no. 3, pp. 411–425, 1998.
- [44] J. Li, F. Li, M. He, F. Xue, M. Zhang, and C. Wang, "Indentation technique for estimating the fracture toughness of 7050 aluminum alloy with the Berkovich indenter," *Materials & Design*, vol. 40, pp. 176–184, 2012.
- [45] Z. Yuan, F. Li, P. Zhang, B. Chen, and F. Xue, "Mechanical properties study of particles reinforced aluminum matrix composites by micro-indentation experiments," *Chinese Journal of Aeronautics*, vol. 27, no. 2, pp. 397–406, 2014.
- [46] C. Walter and C. Mitterer, "3D versus 2D finite element simulation of the effect of surface roughness on nanoindentation of hard coatings," *Surface and Coatings Technology*, vol. 203, no. 20–21, pp. 3286–3290, 2009.
- [47] Y. Liu, B. Wang, M. Yoshino, S. Roy, H. Lu, and R. Komanduri, "Combined numerical simulation and nanoindentation for determining mechanical properties of single crystal copper at mesoscale," *Journal of the Mechanics and Physics of Solids*, vol. 53, no. 12, pp. 2718–2741, 2005.
- [48] S.-R. Jian, C.-H. Tasi, S.-Y. Huang, and C.-W. Luo, "Nanoindentation pop-in effects of Bi₂Te₃ thermoelectric thin films," *Journal of Alloys and Compounds*, vol. 622, pp. 601–605, 2015.
- [49] J. Cai, F. Li, T. Liu, and B. Chen, "Investigation of mechanical behavior of quenched Ti-6Al-4V alloy by microindentation," *Materials Characterization*, vol. 62, no. 3, pp. 287–293, 2011.
- [50] M. S. Park and Y. S. Suh, "Hardness estimation for pile-up materials by strain gradient plasticity incorporating the geometrically necessary dislocation density," *Journal of Mechanical Science and Technology*, vol. 27, no. 2, pp. 525–531, 2013.
- [51] K. Durst, B. Backes, and M. Göken, "Indentation size effect in metallic materials: correcting for the size of the plastic zone," *Scripta Materialia*, vol. 52, no. 11, pp. 1093–1097, 2005.
- [52] H. Ledbetter and A. Migliori, "A general elastic-anisotropy measure," *Journal of Applied Physics*, vol. 100, no. 6, Article ID 063516, 2006.
- [53] D. Tabor, *The Hardness of Metals*, Clarendon Press, Oxford, UK, 1951.
- [54] J. Dong, F. Li, and C. Wang, "Micromechanical behavior study of α phase with different morphologies of Ti-6Al-4V alloy by microindentation," *Materials Science and Engineering: A*, vol. 580, pp. 105–113, 2013.
- [55] S.-R. Jian and Y.-Y. Lin, "Berkovich nanoindentation-induced dislocation energetics and pop-in effects in ZnSe thin films," *Journal of Alloys and Compounds*, vol. 590, pp. 153–156, 2014.
- [56] C.-H. Tasi, Y.-C. Tseng, S.-R. Jian et al., "Nanomechanical properties of Bi₂Te₃ thin films by nanoindentation," *Journal of Alloys and Compounds*, vol. 619, pp. 834–838, 2015.
- [57] S. Mandal, V. Rakesh, P. V. Sivaprasad, S. Venugopal, and K. V. Kasiviswanathan, "Constitutive equations to predict high temperature flow stress in a Ti-modified austenitic stainless steel," *Materials Science and Engineering A*, vol. 500, no. 1–2, pp. 114–121, 2009.
- [58] M. He, F. Li, and N. Ali, "A normalized damage variable for ductile metals based on toughness performance," *Materials Science and Engineering A*, vol. 528, no. 3, pp. 832–837, 2011.
- [59] S. Mandal, P. V. Sivaprasad, S. Venugopal, and K. P. N. Murthy, "Artificial neural network modeling to evaluate and predict the deformation behavior of stainless steel type AISI 304L during hot torsion," *Applied Soft Computing Journal*, vol. 9, no. 1, pp. 237–244, 2009.

Research Article

Atomic Structure and Energy Distribution of Collapsed Carbon Nanotubes of Different Chiralities

Julia A. Baimova,^{1,2} Qin Fan,¹ Liangcai Zeng,¹ Zhigang Wang,¹ Sergey V. Dmitriev,^{2,3} Xiqiao Feng,⁴ and Kun Zhou⁵

¹The Key Laboratory of Metallurgical Equipment and Control of Ministry of Education, Wuhan University of Science and Technology, 947 Heping Avenue, Wuhan 430081, China

²Institute for Metals Superplasticity Problems, Russian Academy of Sciences, Ufa 450001, Russia

³National Research Tomsk State University, 36 Lenin Prospekt, Tomsk 634050, Russia

⁴Department of Engineering Mechanics, Tsinghua University, Beijing 100084, China

⁵School of Mechanical and Aerospace Engineering, Nanyang Technological University, 50 Nanyang Avenue, Singapore 639798

Correspondence should be addressed to Xiqiao Feng; fengxq@mail.tsinghua.edu.cn and Kun Zhou; kzhou@ntu.edu.sg

Received 10 September 2014; Accepted 17 December 2014

Academic Editor: Nay Ming Huang

Copyright © 2015 Julia A. Baimova et al. This is an open access article distributed under the Creative Commons Attribution License, which permits unrestricted use, distribution, and reproduction in any medium, provided the original work is properly cited.

For carbon nanotubes of sufficiently large diameter at sufficiently low temperature, due to the action of the van der Waals forces, the ground state is a bilayer graphene with closed edges, the so-called collapsed configuration. Molecular dynamics simulation of collapsed carbon nanotubes is performed. The effect of length, diameter, and chirality of the nanotubes on their properties is investigated. It is shown that collapsed nanotubes after relaxation have rippled structure which is strongly dependent on the nanotube chirality. The structural properties are studied by calculating the radial distribution function and energy distribution along various regions in the collapsed carbon nanotubes.

1. Introduction

Due to their extraordinary properties arising from the unique one-dimensional structure, carbon nanotubes (CNTs) have been the subject of intense theoretical and experimental studies since their discovery [1]. There have been numerous works on the mechanics of nanotubes and their properties in recent years because of their great potential for composites, sensors, electronic devices, and many other applications [2–6]. Calculation of the elastic properties of nanotubes confirms that they are extremely rigid in the axial direction and are most likely to distort perpendicular to the axis [7, 8].

Experimental investigations, as well as theoretical works ranging from full atomistic simulations to continuum modeling, have been used to study the existence of CNTs whose overall geometry differs radically from that of an ideal cylinder. Recent studies [9–17] have shown that a single-walled CNT with an appropriate diameter has two stable states, circular and collapsed, with different potential energy.

Such an energy difference is interesting because CNTs can be used as an energy source during the transformation between the two states. The nanotubes, which are collapsed along their length, energetically are more favorable than the form with a circular cross-section [11]. Nanotube collapse was called “domino process” and modeled by molecular dynamics (MD) both at zero and finite temperatures [9, 10]. It was also shown that collapse can significantly affect the electrical properties of CNTs [18–20].

The collapse of single-walled CNT studied via classical MD and molecular mechanics suggested that CNTs with a radius larger than 3 nm will collapse, since the energy of the collapsed state is lower than that of the circular, uncollapsed state. The energetics of the collapse of single- and multiwalled CNTs via MD was also studied in [21]. The formation of fully collapsed single-walled CNT with the atomic scale finite-element method was investigated in [22]. Interestingly, collapsed multiwalled CNTs may exist in different forms [23]. The elastic model shows that there exist

collapsed configurations of different orders, each involving a different number of collapsed layers [24].

In particular, the production of super-strong nanotube bundles and other three-dimensional carbon structures remains a challenge to the current materials science. Since then, many researches have been carried out to understand the behavior of bundles of carbon nanotubes under high pressures [25–32].

In this paper, the MD simulation aimed at the investigation of energy and structure of collapsed single-walled CNTs is presented. Phenomena of structural transformation are shown by the radial distribution functions. Various types of rippled collapsed structures are studied.

2. Simulation Details

The topography of CNT is denoted by a pair of integer numbers (n, m) . In this study, initial atomic configurations were obtained by creating a CNT with specified parameters. Four CNTs of various chirality are considered: zigzag (96,0), armchair (55,55), and two chiral CNTs (50,60) and (40,70). The chirality indices are chosen to maintain the number of atoms in the CNTs to be almost the same at the same length and nearly the same diameter. The number of carbon atoms in the largest CNTs is about 18500. Single-walled CNTs of various lengths from $L = 20$ to 200 nm are simulated to check the effect of length on its properties. It was shown that the length has no significant effect on some properties of collapsed structures, while it can slightly affect the other properties. The length $L = 100$ nm, as the average between considered values, is chosen as the example for further descriptions.

The simulations are carried out using the large-scale atomic/molecular massively parallel simulator (LAMMPS) package [33] with the adaptive intermolecular reactive empirical bond order (AIREBO) potential [34], which has been widely used to describe the short range bonding energies among carbon atoms in many studies on the behavior and properties of graphitic polymorphs [31, 32, 35–38]. Additionally, the van der Waals forces between two carbon atoms are modeled by the Lennard-Jones potential with the equilibrium distance of 3.4 Å and the bond energy of 0.024 eV. Relaxational dynamics is carried out to find the equilibrium configurations of the collapsed CNTs.

Stability of the collapsed configuration was shown in the previous studies [9, 10]. The main goal of this work was the investigation of the collapsed state and the properties of collapsed nanotubes; that is why the initial open state of the CNT is not presented here. Collapsed nanotubes were created by application of the lateral forces applied to the atoms. After the collapsed nanotube is created, the action of the external forces is removed and the self-folded structure is relaxed to a minimum potential energy state, as shown in Figure 1(a). The relaxation of the CNT strongly depends on the chirality, which will be discussed in the sequel.

Figure 1(b) shows the schematic of a collapsed CNT. To study the energy distribution, the atoms of the self-folded CNT with its total width H were divided into two groups:

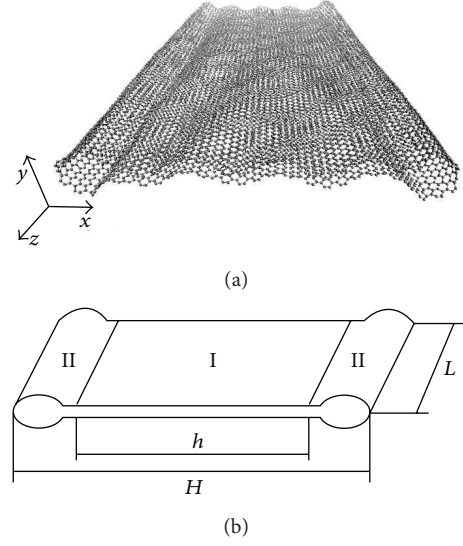


FIGURE 1: (a) Initial structure of collapsed CNT_(50,60). (b) Schematic of folded CNT. Bilayer graphene of width h is the region I and the two round edges constitute the region II.

the atoms in the central flat region where one has bilayer graphene of width h (region I) and the atoms in the two round edges (region II). Let N_1 denote the number of atoms in the bilayer graphene area ($h \times L$) and N the total number of atoms. Then the region II has $N_2 = N - N_1$ atoms. For the collapsed structure, the opposite walls in region I are within the van der Waals distance.

The studied energies are the energy per atom of bilayer graphene, E_1 (region I), and the energy per atom for round edges, E_2 (region II). The energy in region I is

$$E_1 = \frac{e}{N_1}, \quad (1)$$

where e is the potential energy of the area $h \times L$, and the energy in region II is

$$E_2 = \frac{(E - e)}{N_2}, \quad (2)$$

where E is the total potential energy of the area $H \times L$.

3. Results and Discussion

The effect of CNT diameter D on the potential energy is studied for the collapsed armchair CNTs with $L = 100$ Å. The nanotube chirality slightly affects the energies E_1 and E_2 but has no qualitative effect; that is why the results only for the armchair CNTs are presented as the example. In Figure 2, the potential energy as the function of CNT diameter is shown for E_1 (solid line) and E_2 (dashed line). It can be seen that for the small diameter the energy of collapsed edges of the nanotubes, E_2 , is higher and it rises nonlinearly with decrease in D , which is in consistence with the previous works [9, 10]. The competition of the van der Waals energy, providing attractive force to collapse the tube, and the elastic

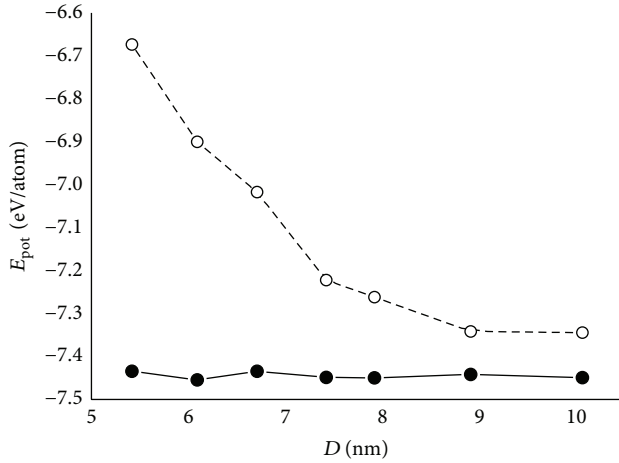


FIGURE 2: The potential energy per atom as the function of CNT diameter D for region I (E_1 , solid line) and region II (E_2 , dashed line).

energy, which always tends to keep the tube circular, leads to the mechanically bistable configuration of a single-walled CNT with the two competitive energies. For tubes of smaller diameter, the elastic energy is dominant (thus the circular structure of the tube is stable), while for tubes with larger diameter the van der Waals energy is dominant, meaning that the collapsed structure of the tube is stable whereas the circular structure is metastable [7]. In the following, the properties of collapsed nanotubes are reported for the CNT diameter of $D \sim 7.5$ nm.

The effect of the CNT length on the potential energy of the CNT in the relaxed state is investigated. The behavior of chiral CNTs is quite different from that of armchair and zigzag CNTs. For the whole range of lengths, E_1 stays almost constant for all CNTs, while the energy of round edges, E_2 , slowly decreases with the length increase for the armchair CNT and remains constant for other types of CNTs. The energy of chiral CNTs is found to be lower than that of the armchair and zigzag CNTs. No distinct effect of CNT length on the collapse and formation of final relaxed structures is observed since the considered CNTs have a relatively large length. The detailed analysis of the distribution of the potential energy showed that the highest energy concentrates on the ridges of the collapsed edges, while bilayer graphene (region I) has the lowest potential energy.

The relaxed states of four collapsed CNTs are shown in Figure 3 for (a) $\text{CNT}_{(40,70)}$, (b) $\text{CNT}_{(50,60)}$, (c) $\text{CNT}_{(55,55)}$, and (d) $\text{CNT}_{(96,0)}$. It can be seen that CNTs after relaxation become rippled, which is in consistency with graphene [39, 40]. In reality, the bilayer graphene region will not remain ideally flat and its shape will depend on the spatially distributed cohesive forces due to van der Waals interactions. As it can be seen from Figure 3, a set of ripples appear in the collapsed CNTs reflecting the (in)commensurate structures in the mutual arrangements of atoms in the two graphene sheets in contact. The ripples contribute to the total potential energy of the collapsed CNTs. According to the earlier studies [15, 21], the most energetically favorable mutual position

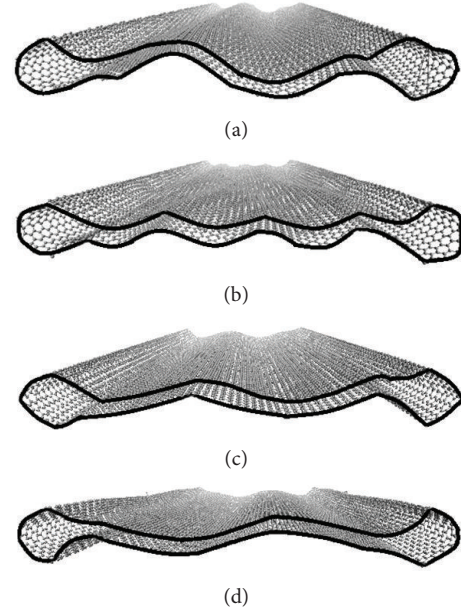


FIGURE 3: Relaxed structures of collapsed CNTs: (a) $\text{CNT}_{(40,70)}$, (b) $\text{CNT}_{(50,60)}$, (c) $\text{CNT}_{(55,55)}$, and (d) $\text{CNT}_{(96,0)}$.

of the two graphene sheets is when the C atoms of one sheet are above the centers of the 6-atom rings of another sheet. The ripples in bilayer graphene appear to minimize the contribution from the van der Waals bonds to the total potential energy of CNT. Only in the case of zigzag and armchair orientations the minimal energy position can be achieved by the mutual translation of the two sheets in contact. In other cases the mutual rotation of the sheets is required. In the case of collapsed CNT the mutual rotation is restricted by the closed ends of the graphene sheets. Only local atomic shifts and rotations can be realized resulting in the appearance of ripples. Not only rippling of the bilayer graphene region but also the shape of the edges is strongly dependent on the chirality of CNT. Physically, stretching of the C-C bonds is difficult because they are stiff and strong. Therefore, during collapse, the cross-section configuration of CNT will be such that the stretching of the C-C bonds is minimal. On the other hand, the bending rigidity of graphene sheet is known to be rather small. In some cases, the elastic energy of bending can be concentrated to create a sharp ridge. This happens, for example, for $\text{CNT}_{(55,55)}$, as can be seen in Figure 3(c). For CNTs with other chiralities the sharp ridges are not observed.

To further analyze the collapsed structures of CNTs, radial distribution functions (RDF), $g(r)$, are presented in Figure 4 for $\text{CNT}_{(96,0)}$ (thin solid line), $\text{CNT}_{(55,55)}$ (thick solid line), and $\text{CNT}_{(50,60)}$ and $\text{CNT}_{(40,70)}$ (dashed line). Note that the coordination shells for single-layer flat graphene have radii $\rho, \sqrt{3}\rho, 2\rho, \sqrt{7}\rho \dots$, where ρ is the C-C bond length. For $\rho = 1.42 \text{ \AA}$ the main peaks of RDF are expected at 1.42, 2.46, 2.84, 3.75... \AA , which is in good agreement with the results shown in Figure 4. The small and relatively broad peak near 3.4 \AA , also shown in the inset of Figure 4, can be attributed to

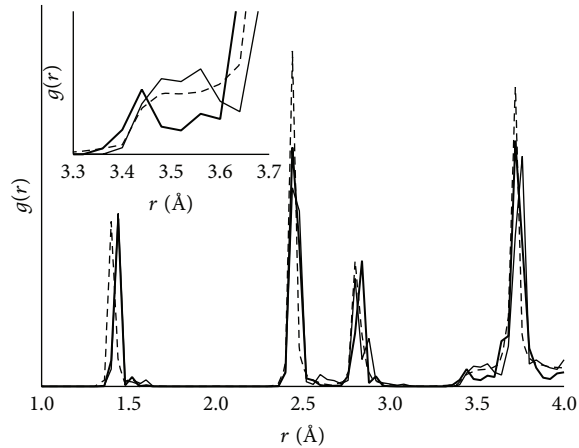


FIGURE 4: Radial distribution functions for $\text{CNT}_{(96,0)}$ (thin solid line), $\text{CNT}_{(55,55)}$ (thick solid line), and $\text{CNT}_{(50,60)}$ and $\text{CNT}_{(40,70)}$ (dashed line).

the van der Waals bonds between layers in bilayer graphene. It can be seen that for the zigzag and chiral CNTs this peak is broader than for the armchair nanotube, meaning that the coherency of layers in region I for the nanotubes of different chirality is different. For the nanotubes $\text{CNT}_{(50,60)}$ and $\text{CNT}_{(40,70)}$, RDF is almost the same, as shown by the dashed line in Figure 4.

4. Conclusions

The energy distribution and structure of collapsed carbon nanotubes of different diameter, length, and chirality have been investigated using molecular dynamics simulations. The obtained results revealed that the relaxed shape of the collapsed CNTs strongly depends on the chirality and other geometry parameters. For CNTs with different chiralities, we have observed different ripple configurations of the bilayer graphene region as well as different structures of the edges (see Figure 3). This is important because the ripples and cross-sectional profile can considerably change the mechanical and physical properties of CNTs.

The highest potential energy density in collapsed CNTs is observed along the ridges, which appear on the collapsed circled edges, while bilayer graphene has the lowest energy density. Taking into account the ability of collapsed CNT to return to the tubular metastable state through a reversible thermodynamic process explained in [10], it is possible to develop novel structures with anomalous thermal expansion and other anomalous properties in the temperature range where such transformation takes place. The results are therefore expected to provide new insights that will enhance the design of collapsed CNT-based devices and materials. The process of collapse and its effect on the properties as well as interplay between curvature energy and van der Waals energy may also be relevant to the collapse of larger graphitic structures such as carbon whiskers and are relevant to the description of the structure and properties of crumpled graphene [41, 42].

Conflict of Interests

The authors declare that there is no conflict of interests regarding the publication of this paper.

Acknowledgments

The authors acknowledge financial support by the National Natural Science Foundation of China (Grant no. 11472200) and the Open Fund of the Key Laboratory for Metallurgical Equipment and Control of Ministry of Education in Wuhan University of Science and Technology, China (Grant no. 2014C01). Julia A. Baimova and Sergey V. Dmitriev acknowledge financial support provided by the Russian Science Foundation through Grant no. 14-13-00982.

References

- [1] S. Iijima, "Helical microtubules of graphitic carbon," *Nature*, vol. 354, no. 6348, pp. 56–58, 1991.
- [2] O. Herranen, D. Talukdar, and M. Ahlskog, "Ultra-low noise multiwalled carbon nanotube transistors," *Carbon*, vol. 76, pp. 71–76, 2014.
- [3] L. Wang and L. Cheng, "Piezoresistive effect of a carbon nanotube silicone-matrix composite," *Carbon*, vol. 71, pp. 319–331, 2014.
- [4] A. Mathur, S. S. Roy, K. S. Hazra, D. S. Misra, and J. A. McLaughlin, "Growth of carbon nanotube arrays using nanosphere lithography and their application in field emission devices," *Diamond and Related Materials*, vol. 19, no. 7–9, pp. 914–917, 2010.
- [5] Q. Zhou, F. Meng, Z. Liu, and S. Shi, "The thermal conductivity of carbon nanotubes with defects and intramolecular junctions," *Journal of Nanomaterials*, vol. 2013, Article ID 842819, 7 pages, 2013.
- [6] K.-S. Lin, Y.-J. Mai, S.-R. Li, C.-W. Shu, and C.-H. Wang, "Characterization and hydrogen storage of surface-modified multiwalled carbon nanotubes for fuel cell application," *Journal of Nanomaterials*, vol. 2012, Article ID 939683, 12 pages, 2012.
- [7] G. Overney, W. Zhong, and D. Tománek, "Structural rigidity and low frequency vibrational modes of long carbon tubules," *Physica D*, vol. 27, no. 1, pp. 93–96, 1992.
- [8] J. Tersoff and R. S. Ruoff, "Structural properties of a carbon-nanotube crystal," *Physical Review Letters*, vol. 73, no. 5, pp. 676–679, 1994.
- [9] T. Chang, "Dominoes in carbon nanotubes," *Physical Review Letters*, vol. 101, no. 17, Article ID 175501, 4 pages, 2008.
- [10] T. Chang and Z. Guo, "Temperature-induced reversible dominoes in carbon nanotubes," *Nano Letters*, vol. 10, no. 9, pp. 3490–3493, 2010.
- [11] N. G. Chopra, L. X. Benedict, V. H. Crespi, M. L. Cohen, S. G. Louie, and A. Zettl, "Fully collapsed carbon nanotubes," *Nature*, vol. 377, no. 6545, pp. 135–138, 1995.
- [12] L. X. Benedict, N. G. Chopra, M. L. Cohen, A. Zettl, S. G. Louie, and V. H. Crespi, "Microscopic determination of the interlayer binding energy in graphite," *Chemical Physics Letters*, vol. 286, no. 5–6, pp. 490–496, 1998.
- [13] G. Gao, T. Çağın, and W. A. Goddard III, "Energetics, structure, mechanical and vibrational properties of single-walled carbon nanotubes," *Nanotechnology*, vol. 9, no. 3, pp. 184–191, 1998.

- [14] M.-F. Yu, M. J. Dyer, and R. S. Ruoff, "Structure and mechanical flexibility of carbon nanotube ribbons: an atomic-force microscopy study," *Journal of Applied Physics*, vol. 89, no. 8, pp. 4554–4557, 2001.
- [15] B. Liu, M. F. Yu, and Y. Huang, "Role of lattice registry in the full collapse and twist formation of carbon nanotubes," *Physical Review B—Condensed Matter and Materials Physics*, vol. 70, no. 16, Article ID 161402, 2004.
- [16] T. Tang, A. Jagota, C.-Y. Hui, and N. J. Glassmaker, "Collapse of single-walled carbon nanotubes," *Journal of Applied Physics*, vol. 97, no. 7, Article ID 074310, 2005.
- [17] T. Chang, J. Hou, and X. Guo, "Reversible mechanical bistability of single-walled carbon nanotubes under axial strain," *Applied Physics Letters*, vol. 88, no. 21, Article ID 211906, 2006.
- [18] R. Martel, T. Schmidt, H. R. Shea, T. Hertel, and Ph. Avouris, "Single- and multi-wall carbon nanotube field-effect transistors," *Applied Physics Letters*, vol. 73, no. 17, pp. 2447–2449, 1998.
- [19] C. J. Park, Y. H. Kim, and K. J. Chang, "Band-gap modification by radial deformation in carbon nanotubes," *Physical Review B—Condensed Matter and Materials Physics*, vol. 60, Article ID 10656, 1999.
- [20] J.-Q. Lu, J. Wu, W. Duan, F. Liu, B.-F. Zhu, and B.-L. Gu, "Metal-to-semiconductor transition in squashed armchair carbon nanotubes," *Physical Review Letters*, vol. 90, Article ID 156601, 2003.
- [21] J. Xiao, B. Liu, Y. Huang, J. Zuo, K.-C. Hwang, and M.-F. Yu, "Collapse and stability of single- and multi-wall carbon nanotubes," *Nanotechnology*, vol. 18, Article ID 395703, 2007.
- [22] B. Liu, Y. Huang, H. Jiang, S. Qu, and K. C. Hwang, "The atomic-scale finite element method," *Computer Methods in Applied Mechanics and Engineering*, vol. 193, no. 17–20, pp. 1849–1864, 2004.
- [23] M. F. Yu, M. J. Dyer, J. Chen, D. Qian, W. K. Liu, and R. S. Ruoff, "Locked twist in multiwalled carbon-nanotube ribbons," *Physical Review B—Condensed Matter and Materials Physics*, vol. 64, Article ID 241403(R), 2001.
- [24] T. Tang and N. J. Glassmaker, "On the inextensible elastica model for the collapse of nanotubes," *Mathematics and Mechanics of Solids*, vol. 15, no. 5, pp. 591–606, 2010.
- [25] K. V. Shanavas and S. M. Sharma, "Molecular dynamics simulations of phase transitions in argon-filled single-walled carbon nanotube bundles under high pressure," *Physical Review B*, vol. 79, no. 15, Article ID 155425, 2009.
- [26] A. Liao, R. Alizadegan, Z.-Y. Ong et al., "Thermal dissipation and variability in electrical breakdown of carbon nanotube devices," *Physical Review B*, vol. 82, Article ID 205406, 2010.
- [27] X. Yang and G. Wu, "The study of structural, electronic and optical properties of double-walled carbon nanotube bundles under hydrostatic pressure," *Europhysics Letters*, vol. 81, no. 4, Article ID 47003, 2008.
- [28] J. Sandler, M. S. P. Shaffer, A. H. Windle et al., "Variations in the Raman peak shift as a function of hydrostatic pressure for various carbon nanostructures: a simple geometric effect," *Physical Review B*, vol. 67, Article ID 035417, 2003.
- [29] J. Tang, L.-C. Qin, T. Sasaki, M. Yudasaka, A. Matsushita, and S. Iijima, "Compressibility and polygonization of single-walled carbon nanotubes under hydrostatic pressure," *Physical Review Letters*, vol. 85, no. 9, Article ID 1887, 2000.
- [30] S. Karmakar, S. M. Sharma, P. V. Teredesai et al., "Structural changes in single-walled carbon nanotubes under non-hydrostatic pressures: X-ray and Raman studies," *New Journal of Physics*, vol. 5, article 143, 2003.
- [31] J. A. Baimova, B. Liu, S. V. Dmitriev, and K. Zhou, "Mechanical properties and structures of bulk nanomaterials based on carbon nanopolymorphs," *Physica Status Solidi—Rapid Research Letters*, vol. 8, no. 4, pp. 336–340, 2014.
- [32] J. A. Baimova, B. Liu, S. V. Dmitriev, N. Srikanth, and K. Zhou, "Mechanical properties of bulk carbon nanostructures: effect of loading and temperature," *Physical Chemistry Chemical Physics*, vol. 16, no. 36, pp. 19505–19513, 2014.
- [33] S. Plimpton, "Fast parallel algorithms for short-range molecular dynamics," *Journal of Computational Physics*, vol. 117, no. 1, pp. 1–19, 1995.
- [34] S. J. Stuart, A. B. Tutein, and J. A. Harrison, "A reactive potential for hydrocarbons with intermolecular interactions," *The Journal of Chemical Physics*, vol. 112, no. 14, pp. 6472–6486, 2000.
- [35] B. Liu, C. D. Reddy, J. Jiang et al., "Morphology and in-plane thermal conductivity of hybrid graphene sheets," *Applied Physics Letters*, vol. 101, no. 21, Article ID 211909, 2012.
- [36] B. Liu, C. D. Reddy, J. Jiang et al., "Thermal conductivity of silicene nanosheets and the effect of isotopic doping," *Journal of Physics D: Applied Physics*, vol. 47, no. 16, Article ID 165301, 2014.
- [37] B. Liu, J. A. Baimova, S. V. Dmitriev, X. Wang, H. Zhu, and K. Zhou, "Discrete breathers in hydrogenated graphene," *Journal of Physics D: Applied Physics*, vol. 46, no. 30, Article ID 305302, 2013.
- [38] J. A. Baimova, B. Liu, and K. Zhou, "Folding and crumpling of graphene under biaxial compression," *Letters on Materials*, vol. 4, no. 2, pp. 96–99, 2014.
- [39] J. A. Baimova, S. V. Dmitriev, K. Zhou, and A. V. Savin, "Unidirectional ripples in strained graphene nanoribbons with clamped edges at zero and finite temperatures," *Physical Review B: Condensed Matter and Materials Physics*, vol. 86, no. 3, Article ID 035427, 2012.
- [40] J. A. Baimova, S. V. Dmitriev, and K. Zhou, "Strain-induced ripples in graphene nanoribbons with clamped edges," *Physica Status Solidi B*, vol. 249, no. 7, pp. 1393–1398, 2012.
- [41] E. A. Korznikova, J. A. Baimova, S. V. Dmitriev, A. V. Korznikova, and R. R. Mulyukov, "Mechanical behavior of crumpled sheet materials subjected to uniaxial compression," *Reviews on Advanced Materials Science*, vol. 39, pp. 92–98, 2014.
- [42] J. A. Baimova, E. A. Korznikova, S. V. Dmitriev, B. Liu, and K. Zhou, "Review on crumpled graphene: unique mechanical properties," *Reviews on Advanced Materials Science*, vol. 39, pp. 69–83, 2014.

Research Article

Mechanisms of Hydrogen Transport in Flexible-Wall Narrow Carbon Nanotubes

Bin-Hao Chen,¹ Chieh Kung,² and I-Peng Chu³

¹Department of Energy Application Engineering, Far East University, No. 49, Zhonghua Road, Xinshi District, Tainan City 74448, Taiwan

²Department of Industrial Design, Far East University, No. 49, Zhonghua Road, Xinshi District, Tainan City 74448, Taiwan

³Department of Mechanical Engineering, Far East University, No. 49, Zhonghua Road, Xinshi District, Tainan City 74448, Taiwan

Correspondence should be addressed to Bin-Hao Chen; binhao17@gmail.com

Received 29 April 2014; Revised 9 July 2014; Accepted 12 August 2014

Academic Editor: Xi-Qiao Feng

Copyright © 2015 Bin-Hao Chen et al. This is an open access article distributed under the Creative Commons Attribution License, which permits unrestricted use, distribution, and reproduction in any medium, provided the original work is properly cited.

Understanding the interaction between hydrogen and carbon nanotubes is crucial to enhancing the performance of hydrogen storage and nanofluidic carbon-adsorbent systems. Accordingly, this study performs a series of molecular dynamics simulations to investigate the transport properties of hydrogen molecules confined within a flexible narrow carbon nanotube. The tube's diameter is 10.8 Å at temperatures in the range of 100~800 K. The particle loadings inside carbon nanotubes are ranging from 0.01~1 No/Å. The results show that the hydrogen molecules exhibit three distinct diffusion regimes, namely, single-file, Fickian, and ballistic, depending on the value of the Knudsen number. In addition, it is shown that with the Knudsen number of less than 1, the tube-wall long wavelength acoustic phonons induced Rayleigh traveling wave prompts a longitudinal wave slip and compression-expansion of the hydrogen molecule crowds within the CNT, which leads to a significant increase in the mean square displacement of the molecules.

1. Introduction

A hydrogen-based energy economy, properly integrated with the use of renewable energy resources, provides the potential to satisfy the energy requirements of vehicles, buildings, portable electronic devices, and so on [1, 2]. However, in practice, the feasibility of a hydrogen economy is constrained by the difficulties involved in designing suitable hydrogen storage and delivery systems. Previous studies have shown that hydrogen gas condenses to a high density state when confined within a narrow, single-wall nanotube (SWNT) [3]. The actual mechanisms of hydrogen diffusion within SWNTs and carbon nanotubes (CNTs) are still unclear. Many researchers [1–9] have demonstrated that the structure and properties of nanometer scale materials can be quite different from those of bulk materials due to the presence of surface effects. Accordingly, lightweight carbon adsorbent materials have become interesting for possible use in a hydrogen storage system. The exceptional physical properties of CNTs, including high thermal conductivity, strong mechanical properties, excellent electrical conductivity, and

so forth, render them highly promising candidates for a range of hydrogen storage and delivery applications. Consequently, the nanofluidic adsorption properties and transport mechanisms of hydrogen molecules within SWNTs and CNTs have attracted great interest in the energy industry [4–7]. According to conventional physisorption principles, the gas-adsorption performance of a porous solid is maximized when the pores are no larger than a few molecular diameters [8]. Zuo et al. had conducted a series simulation and suggested an interesting result that MWCNT can be separated into SWCNT in appropriate solvents [9]. Under these conditions, the potential fields produced at the wall overlap to produce a stronger interaction force than that observed in adsorption on a simple plane. However, the mechanisms responsible for the adsorption and transportation of hydrogen in nanoporous solids or nanopores are not easily observed using experimental methods. As a result, the use of computational methods such as molecular dynamics (MD) or Monte Carlo (MC) simulations have emerged as the method of choice for examining the nanofluidic properties of liquids and gases within nanoporous materials [10]. Several groups have

performed numerical simulations to study the adsorption of water in CNTs [11–16], while others have investigated the diffusion of pure hydrocarbon gases and their mixtures through various SWNTs with diameters ranging from 2~8 nm [6, 17, 18]. These studies focus on self- and transport diffusion coefficients of inert gases, hydrogen, and methane in infinitely long SWNTs [19, 20]. In general, the results show that the transport rates in nanotubes are in orders of magnitude higher than those measured experimentally in zeolites or other microporous crystalline solids. In addition, it has been shown that the dynamic flow of helium and argon atoms through SWNTs is highly dependent on the surface temperature of the nanotube wall [21]. Specifically, the flow rate of the helium and argon atoms, as quantified in terms of their self-diffusion coefficients, increased with temperature due to the greater thermal activation effect.

Previous MD simulations of the nanofluidic properties of liquids and gases generally assumed the nanoporous material to have a rigid structure. However, if the nanoporous material is not in fact rigid, the simulation results may deviate from the true values by several orders of magnitude. Several researchers had investigated the conditions under which the assumption of a rigid lattice is, or is not, reasonable [22, 23]. In general, the results showed that while the use of a rigid lattice was permissible in modeling the nanofluidic properties of a gas or liquid in an unconfined condition, a flexible lattice assumption was required when simulating the properties of a fluid within a constrained channel. Moreover, in real-world conditions, the thermal fluctuations of the atoms on a CNT wall impact the diffusive behavior of the adsorbed molecules, and must therefore be taken into account. Jakobtorweihen et al. have reported careful simulations of molecular diffusion considering nanotube flexibility [24]. The reproduction of the results of a flexible carbon nanotube in a rigid nanotube simulation was excellent. Ayappa had examined the influence of nanotube flexibility on the transport diffusion of CH_4 in nanotubes [25]. The inclusion of nanotube flexibility reduces the transport diffusion relative to the rigid nanotube by roughly an order of magnitude close to zero pressure. At the pressure over 1 bar the transport diffusivities for flexible and rigid nanotubes are very similar. Interestingly, whether or not it is reasonable to assume a rigid lattice in diffusion studies is far from being understood [23]. An obvious hypothesis would be that only in the case of narrow passages is flexibility very important. For the cases of gas molecules in carbon nanotubes, or other nanoporous materials, a rigid lattice is a very reasonable assumption [24]. That is to say, if one has a material in which the flexibility cannot be ignored, such as diffusion in confined space, the mechanism will be dominated by surface effect. To prove this opinion, we present herein simulations to track the MSD behavior of hydrogen diffusion inside narrow SWCNT. The simulations show that until the carbon nanotubes are filled with hydrogen molecules up to a specific cutoff density, the molecules diffuse through the nanotubes will transit to a wave manner induced by long wavelength acoustic phonons. For comparison purpose, we conduct a rigid-lattice model to provide the evidence between flexible and rigid lattice model. Results of rigid-lattice model agree with A. I. Skolulidas' results. However,

the MSD curves of rigid-lattice model do not reveal the jump behavior. Rigid-lattice model simulations are shown in the Appendix [Animation A1, A2; Supporting Information].

This study performs a series of MD simulations to investigate the transport properties of hydrogen molecules confined within a narrow CNT with a diameter of 10.8 Å (~1 nm) in temperatures ranging from 100~800 K and particle loadings of 0.01~1 No/Å. To ensure the validity of the simulation results, the MD model assumes the tube to have a flexible wall. Hydrogen molecules are treated as spherical particles. In performing the simulations, the hydrogen molecules are assumed to have a perfectly spherical shape. In addition, the interactions between the molecule and the atoms on the CNT wall and the interactions between the carbon atoms within the CNT wall are modeled using the Lennard-Jones potential [26, 27]. The simulations focus on the hydrogen adsorption within the SWNT instead of in the interstices or the external surface of nanotube bundles. As described above, the simulations performed in this study consider a CNT with a pore size (diameter) of 10.8 Å. In such a small-pore regime [28], the interactions between the pore wall and the hydrogen molecules have a significant effect on the diffusion behavior of the molecules as they migrate along the CNT. The simulations performed in this study consider Knudsen numbers in the range of $0.1 < \text{Kn} < 10$ [29]. In this particular flow regime, the local transport mechanism depends on a number of interfacial parameters, including the strength of the liquid-solid coupling, the thermal roughness of the interface, and the commensurability of the wall and liquid densities, respectively [30]. The diffusivity of the hydrogen molecules is quantified in terms of the mean square displacement (MSD) and self-diffusion coefficient under particle loadings ranging from 0.01~1 No/Å. In diffusion studies, it is a common practice to integrate the equations of motion for hydrogen molecules confined within infinitely long nanotubes. The self-diffusion coefficient is obtained from the average MSD of the hydrogen molecules as a function of time. General Fickian-type diffusion is described by the seminal relation

$$\langle X^2 \rangle = 2Dt^\gamma \quad \text{with } \gamma = 1. \quad (1)$$

However, for more complicated random driving forces, the diffusive behavior may be slower ($\gamma < 1$, subdiffusion) or faster ($\gamma > 1$, superdiffusion) than normal diffusion [29]. In the present simulations, the results obtained for the mean free path are used to compute the Knudsen number, and the diffusion regime is inferred by comparing the time-based variation of the MSD profile with the predicted time-dependent MSD profiles for single-file, Fickian and ballistic diffusion, respectively. In addition to analyzing the change in the diffusion regime over time, the simulations also find out an unexpected “jump phenomenon” on MSD curves. Simulations are conducted to investigate the “slip” of the hydrogen molecules caused by long wavelength acoustic phonons. Tube wall peristaltic movement activates a compression-relaxation diffusion mechanism at very low values of the Knudsen number.

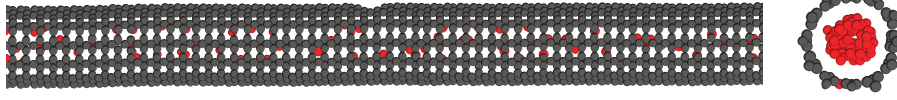


FIGURE 1: Simulation model of hydrogen molecules within SWCNT.

2. Simulation Model

In the simulations, the hydrogen molecules are initially dispersed with a random distribution within the CNT. Figure 1 presents a snapshot of the simulation model for the case in which the CNT contains 70 hydrogen molecules. The current simulations are performed using the methodology presented in [24], which closely mimics the actual interfacial interactions between the hydrogen molecules and the tube wall. In the simulations, the hydrogen molecules are assumed to be “free” (i.e., they can migrate freely from their initial positions) and are heated to an equilibrium state ($\sim 10^4$ fs) via their interaction with the heated CNT wall. The CNT temperature is maintained at the specified value using the Nosé-Hoover thermostat method. In performing the simulations, two different tube-diffuser interactions take place. The interactions can be divided into two types: (1) the carbon atoms vibrate as a result of the applied temperature and collide with the hydrogen molecules near the wall, thereby imparting a transfer of thermal and mechanical energy from the wall to the hydrogen molecules, and (2) the tube is flexible; long wavelength acoustic phonons will be induced and therefore apply a peristaltic driving force to the hydrogen molecules. Since the nanotube is flexible, the lattice vibrational modes are critical. Thus, flexibility can change the morphology of nanotube following the mode of nature vibration. We use a nanotube of length ~ 30 nm to sample the vibration modes accurately and avoid the size effects.

In order to accurately model the interaction between the tube wall and the hydrogen molecules, the simulations consider the case where just one hydrogen molecule exists within the tube such that the effects of inter-diffusant collisions can be ignored. As a result, the diffusion of the hydrogen molecules through the CNT is consistent with the thermal transpiration phenomenon identified by Reynolds [30–34], in which the molecules have more impact on the CNT wall than on one another. In the simulations, the diffusion of the hydrogen molecules is governed by two transient processes. In the first process, the hydrogen molecules are activated by the heated tube surface toward a thermal equilibrium state and start to diffuse within the CNT, while in the second process, the activated molecules interact with the stagnant molecules and cause these molecules to diffuse also. Thus, the moving behavior tends to become a specified diffusion type.

In Figure 1 we show a right view which is parallel with and a left view perpendicular to the pore axis. Note that carbon atoms are shown in black while hydrogen molecules are shown in red. Pore diameter is 10.8 Å.

TABLE 1: Parameters for the carbon interaction potential used in the simulation.

$K_{Cr} = 478.9 \text{ kJ mol}^{-1} \text{Å}^{-2}$	$r_C = 1.418 \text{ Å}$
$K_{C\theta} = 562.2 \text{ kJ mol}^{-1}$	$\theta_C = 120.00^\circ$
$\epsilon_{cc} = 0.4396 \text{ kJ mol}^{-1}$	$\sigma_{cc} = 3.851 \text{ Å}$

TABLE 2: Morse potential dimensionless units used in the simulation.

Unit		Dimensionless unit
Length	r (Å)	$r^* = r/r_0$
Time step	dt (s)	$dt^* = dt \cdot \sqrt{D/(m \cdot r_0^2)}$
Temperature	T (K)	$T^* = T \cdot (k/D)$
Energy	E (eV)	$E^* = E/D$

2.1. Potential Functions. The carbon nanotube is modeled by terms describing the Morse bond and harmonic cosine of the bonding angle as [35, 36]

$$U(r_{ij}, \theta_{ijk}) = K_{cr}(\xi_{ij} - 1)^2 + \frac{1}{2}K_{c\theta}(\cos \theta_{ijk} - \cos \theta_c)^2, \quad (2)$$

where

$$\xi_{ij} = \exp[-\gamma(r_{ij} - r_c)], \quad (3)$$

θ_{ijk} represents all possible bending angles, and r_{ij} represents all distances between bonded atoms. K_{cr} , $K_{c\theta}$ are the force constants of stretch, bend potentials, respectively. r_c , θ_c are the corresponding reference geometry parameters. The Morse stretch and angle bending parameters were first given by Guo et al. [36]. These parameters, listed in Table 1, originally derived to describe the geometry and phonon structure of graphite and fullerene crystals. A Lennard-Jones term is added to the nanotube potential to account for the steric and van der Waals carbon-carbon interaction

$$U(r_{ij}) = 4\epsilon_{cc} \left[\left(\frac{\sigma_{cc}}{r_{ij}} \right)^{12} - \left(\frac{\sigma_{cc}}{r_{ij}} \right)^6 \right]. \quad (4)$$

Excluding 1-2 and 1-3 pairs, the parameters ϵ_{cc} and σ_{cc} are taken from the so-called Universal Force Field (UFF) [31–37].

The physical model scale lying at the microscopic level necessitates introducing some dimensionless units into the simulation activity. These dimensionless parameters are presented in Table 2.

3. Results and Discussions

3.1. Boundary Slip due to Compression-Expansion Process. Before discussion, a key nondimensional parameter for gas micro flows is the *Knudsen number* (Kn), which is defined as the ratio of the mean free path over a characteristic geometry length. A classification of the different flow regimes is given by Schaaf and Chambre [38]. We can observe that, after thermal equilibrium regime, cases with $Kn < 1$ represent a sharp vertical jump simultaneously in MSD curve. Next, we investigate the physical origin of the interaction behavior observed at the moment when “slip” phenomena happened.

To clarify the effect of the initial hydrogen density on the transport properties within the CNT, simulations were performed with various numbers of hydrogen molecules in the range of 0.01–1 No/Å. In each case, the simulation results were used to compute the MSD curves over the duration of the simulation as a function of the system temperature. Figures 2(a)–2(d) present the MSD curves for temperatures of 100 K, 300 K, 500 K, and 800 K, respectively. For clarity, each figure shows the MSD curves only for loadings of 10, 30, 50, 70, and 90 molecules, respectively. (Note, however, that these curves are representative of the curves obtained for all values of the particle loading.) In each figure, it can be seen that the MSD curves exhibit an increase of five to seven orders of magnitude at periodic intervals in the simulation procedure. The jumps in the MSD curves correspond to a “slip” of the hydrogen molecules along the pore axis. Previous studies have concluded that the exceptionally high transport rates observed in nanotubes are the result of the inherent smoothness of the nanotube wall surface [39, 40]. However, the present simulation results suggest that the “slip flow” phenomenon is caused not only by the virtually frictionless interface at the CNT wall, but also by the effects of the compression-relaxation process with $Kn < 1$. The results presented in Figure 2 indicate that following the slip events, the hydrogen molecules diffuse in a ballistic mode until the end of the simulation. Previous studies have reported that boundary slips at the nanoscale occur in both the positive and the negative directions [41–43]. The present simulation results suggest that the occurrence of positive and negative slip in gas flows within a confined space may be a result of a compression-expansion effect.

3.2. Mechanisms of Hydrogen Diffusion. The hydrogen diffusion mechanism within the CNT can be inferred from the scaling behavior of the MSD curves over time. The present simulation results indicate that hydrogen diffusion occurs after 10^4 picoseconds and tends toward an anomalous diffusion mode in either the subdiffusion regime ($\gamma < 1$) or the superdiffusion regime ($\gamma > 1$) as the simulation time approaches 50 ns. In this study, the diffusion mode of the hydrogen molecules is quantified using the following formulation:

$$\langle X^2 \rangle = 2Ct^\gamma, \quad (5)$$

where C is the diffusion mobility and γ is a coefficient whose value depends on both the pore diameter and the particle loading. In other words, the index γ reflects the easiness with

which the molecules can (or cannot) pass one another within the CNT.

The MSD profiles presented in Figure 4 show that the hydrogen molecules experience three distinct diffusion regimes, namely, a short ballistic regime, followed by a subdiffusive regime due to a thermal equilibrium process, and finally an anomalous-diffusion regime or a return to a ballistic-diffusion regime, depending on the value of Kn . Similar distinct diffusion regions have been observed for the diffusion of colloids and certain lightweight molecules [24, 25, 44, 45].

To better understand the hydrogen diffusion mechanism within the present CNT, the following discussions consider the extreme case in which the nanotube contains only one molecule (i.e., free-molecular flow). Under this condition, Kn is larger than 100 ($\lambda \gg d; \sim \infty$); that is, the mean free path is much larger than the pore size. As a result, the migration behavior of the hydrogen atom is dominated by its interaction with the pore wall. The MD results suggest that in free molecular flow condition hydrogen molecule would be exerted a resistance force by the tube wall. The MSD curves represent a quasihorizontal trend toward the end of simulation. This coordinated motion mechanism is observed in a temperature range from 100 K to 800 K. Observing the MSD profiles in Figure 4, it can be seen that the curves exhibit a quasihorizontal trend toward the end of the simulations. This characteristic is particularly pronounced at a temperature lower than 300 K. The relatively constant value of the MSD implies that the wall exerts a resistive effect which opposes the motion of the hydrogen molecule. In practice, it is thought that this resistive force originates from the thermally-induced peristaltic motion of the CNT wall, which gives rise to a nonuniform potential field. With temperatures lower than 300 K, the hydrogen molecule has insufficient kinetic energy to overcome this “surface roughness” effect, and thus its diffusion coefficient saturates to a constant value as the simulation proceeds. The thermally-induced roughness of the CNT surface provides an interesting new insight into the stick-slip phenomena observed in many boundary lubrication problems [40].

The present results indicate that the hydrogen molecules diffuse in a single-file mode for Knudsen numbers in the range of $2 < Kn < 4$. In such a condition, the hydrogen molecules are so rare, and the kinetic energy of each molecule becomes so low, that the molecules cannot overtake one another as they migrate along the CNT. When the temperature is increased to 800 K, the hydrogen molecules exhibit an anomalous diffusion mode for $0.5 < \gamma < 1$. In this regime, the MSD curves are characterized by a greater fluctuation due to the enhanced thermal roughness of the CNT wall. The confined hydrogen molecules diffuse in accordance with a Fickian-type mechanism in the range of $1 < Kn < 2$ since in this particular regime, the molecules are able to pass one another easily as they travel along the CNT. However, as the value of the *Knudsen Number* is reduced, the diffusion mechanism transits to either superanomalous diffusion ($\gamma > 1$) or ballistic diffusion ($\gamma = 2$), depending on the particular value of Kn . For the values of Kn less than 1, the diffusion mechanism

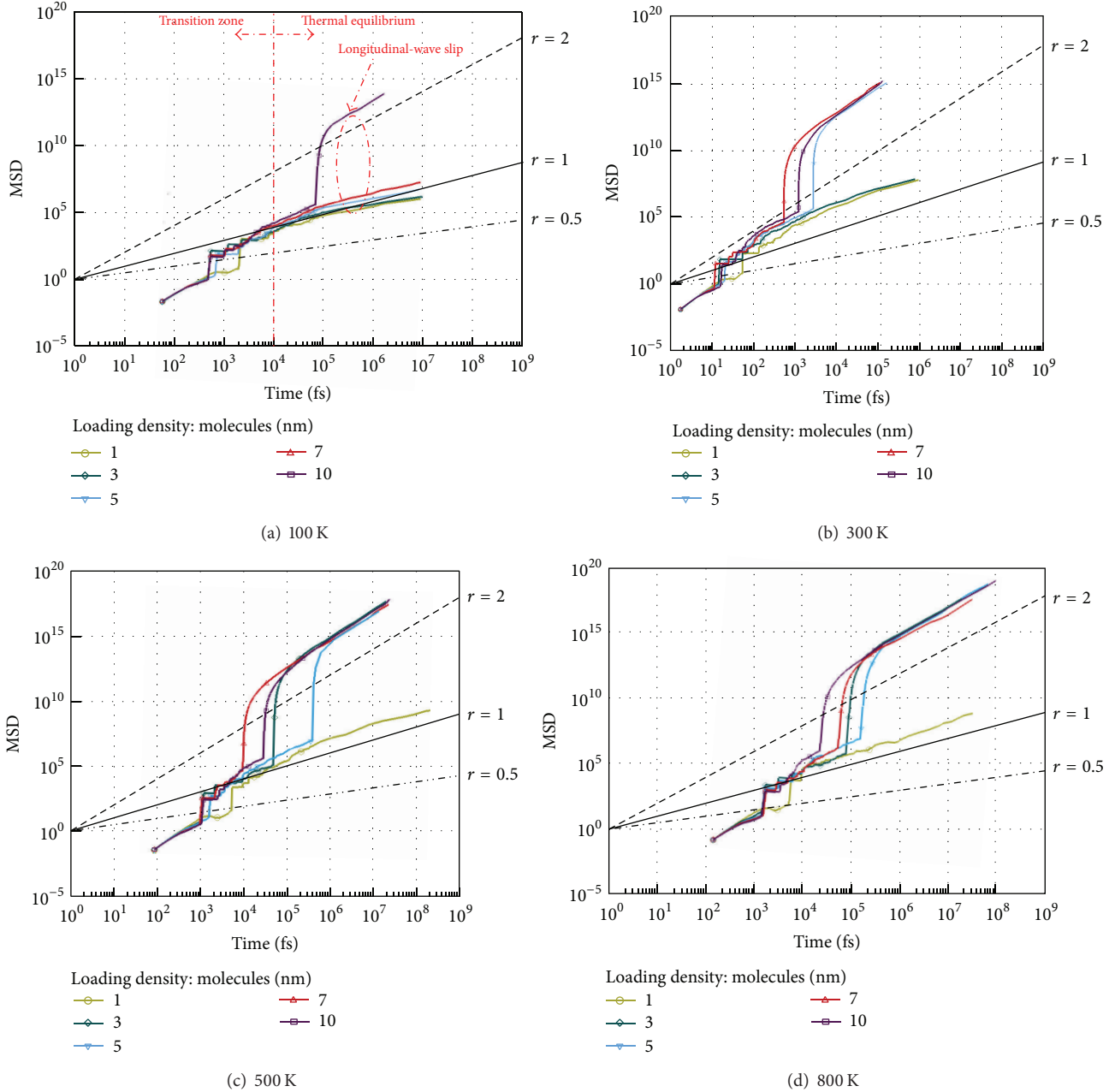


FIGURE 2: (a)–(d): mean square displacement curves, that is, mean square displacement curves of hydrogen molecules along the pore axis ($dz^2 \sim \text{\AA}^2$) as function of time for simulation temperatures of $T = 100$ K, 300 K, 500 K, and 800 K, respectively. Note that the green, turquoise, blue, red, and violet lines correspond to particle loadings of 10, 30, 50, 70, and 90 adsorbed hydrogen molecules, respectively. In addition, the three black lines represent the scaling behavior expected for the ballistic diffusion mechanism (dashed), the Fickian mechanism (solid), and the single-file diffusion mechanism (dashed-dotted), respectively.

transits to a ballistic mode as a result of the compression-expansion process discussed in the previous section.

To understand how the transport properties of confined hydrogen molecules vary as the degree of particle loadings changes, we conducted simulations for several degree of filling ranging from 10 to 120 No/ \AA and the corresponding Knudsen numbers are located in transition flow regime. We repeat the simulation procedure up to 50 ns of production time. In Figure 3, we report the MSD obtained for hydrogen

in partially filled SWNTs. At longer time (above 100 ps) the diffusion mechanism tends to become slower or faster than the Fickian-type which is dependent on Kn. In current simulation results, MSD curves indicate that after the transition zone flow mechanism becomes highly dependent on Kn. This means that the dominating effect on the flow either will still be wall interaction or change to particle collisions. If Kn is greater than 1, flow mechanism performs an anomalous type with $0.5 < \gamma < 1$ dominated by wall thermal

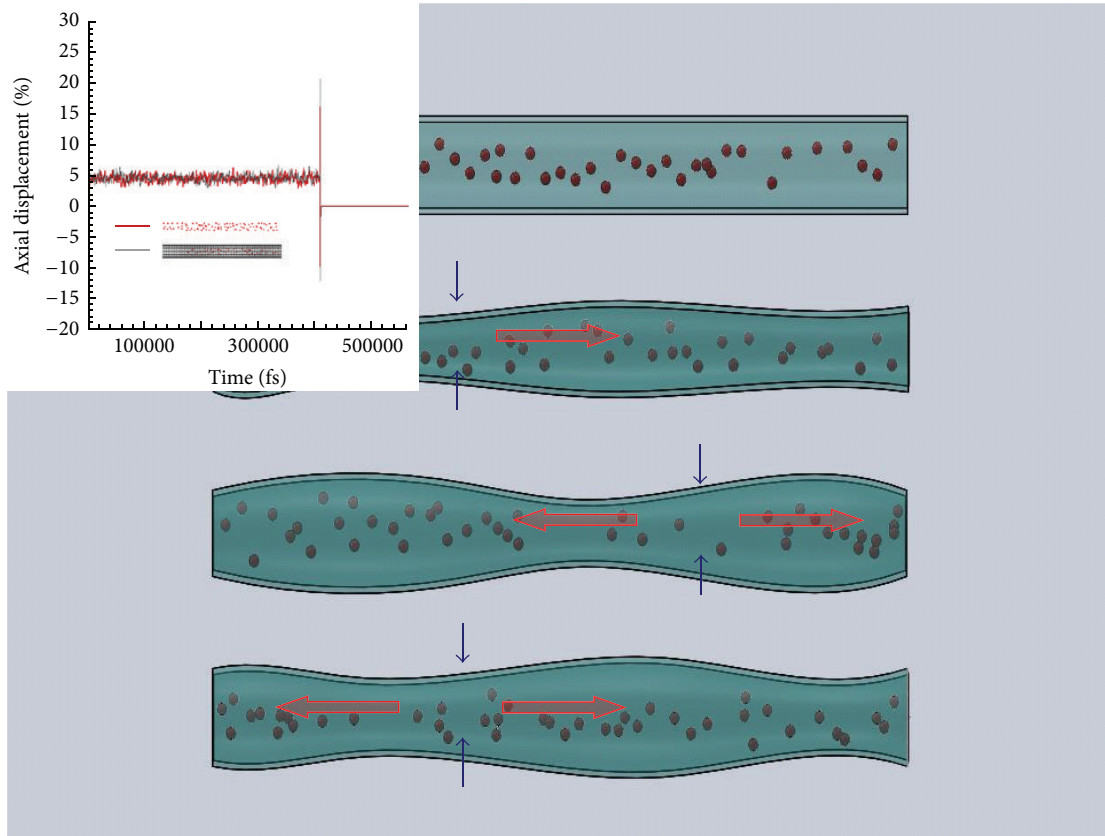


FIGURE 3: Sequence of simulation snapshots. Sequence of simulation snapshots obtained for 50 hydrogen molecules confined within SWCNT at 500 K. The results show the formation of two neighboring molecule crowds which subsequently interact with each other via a compression-relaxation process. Note that the inset shows the tube-wall and diffuser axial vibration displacements at 500 K; load density = 10 molecules/nm. According to the results, both the radial vibration displacements of hydrogen and tube wall present a resonance profile and the radial breathing mode is the most relevant effect in current case.

roughness. Wall fluctuation affects the hydrogen flow. When Kn is smaller than 1, it is clear from visual observation of Animation 2 that particle collisions are responsible for the formation of piecewise crowd distribution of hydrogen molecules within the SWCNTs. The concerted motion of compression-relaxation transport determines the ballistic-type diffusion mechanism evident from the analysis of MSD for up to 106~108 fs (see Figure 3).

3.3. Molecular Origin of Diffusion Mechanism. To understand this jump behavior by molecular origin and appreciate the molecular mechanism of hydrogen diffusion, a simulation model is proposed. Figure 3 presents a sequence of four consecutive snapshots of the simulation model for the case where the CNT contains 50 hydrogen molecules and the system temperature is equal to 500 K ($Kn = 0.48$). It can be seen that the hydrogen molecules have a uniform density distribution initially. However, as the thermal energy is transferred through the tube wall, the hydrogen molecules are transported in the radial direction (i.e., toward the center of the tube). The resulting collisions between the activated molecules and the stagnant molecules, together with the long wavelength acoustic phonons effect exerted by the flexible CNT wall, cause a piecewise increase in the hydrogen density

along the pore axis. The piecewise molecular density distribution produces a concentration gradient across the pore and creates a driving force parallel to the pore axis. After a certain elapsed time, the peristaltic effects and the concentration gradient prompt neighboring crowds of hydrogen molecules to approach one another (i.e., to compress) in the direction indicated by the gray arrow. Interestingly, if the compression gets higher the crowd of hydrogen molecules reacts against the wall compression and moves rapidly along with the tube axis in the direction opposite to the neighbor crowd moves. As the compression effect increases, the resistive force between the hydrogen molecules within neighboring crowds also increases and eventually prompts a separation (i.e., a relaxation) of the two crowds. Therefore, a sudden increase (jump) in the MSD of the hydrogen molecules occurs. Due to the periodic boundary conditions imposed in the simulations, this compression-resistance-relaxation process is repeated periodically along the length of the CNT. And then, this piecewise density distribution performs longitudinal wave propagation. Using this model we can approach the real state of the hydrogen molecules inside SWNTs [Animation 1 (a), (b); Supporting Information]. It is worth mentioning that there exists a singular phenomenon “molecular escape through the CNT interstitial” which also

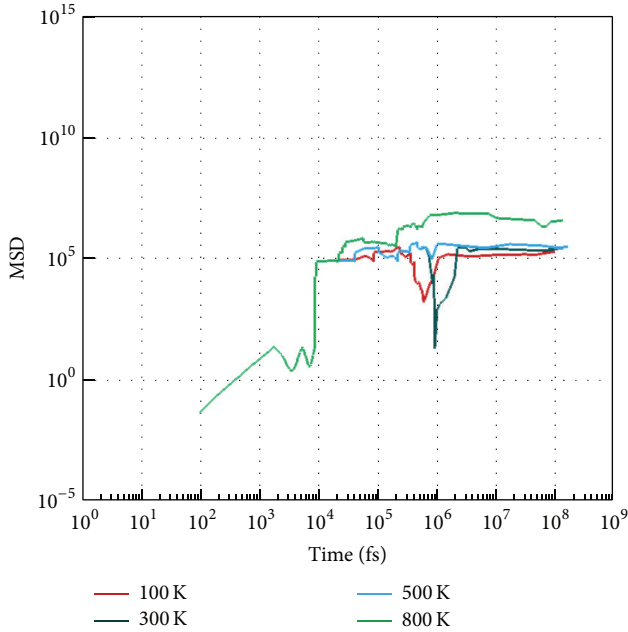


FIGURE 4: Mean square displacement associate with only one hydrogen molecule.

TABLE 3: Kn and γ under different temperatures and particle loading.

T	100 K		300 K		500 K		800 K	
$Kn; \gamma$	Kn	γ	Kn	γ	Kn	γ	Kn	γ
Number								
1	∞		∞		∞		∞	
10	3.75	0.5	1.575	1	2.5	0.85	1.25	1.16
30	2.125	0.5	1.023	0.8	0.537	2	0.525	2
50	1.0627	1	0.613	2	0.48	2	0.4625	2
70	1.023	1	0.5	2	0.45	2	0.3	2
90	0.43	2	0.53	2	0.48	2	0.338	2

can release this compression pressure. This interesting behavior occurred randomly with $Kn < 1$ [Animation 2; Supporting Information].

3.4. Dependence of Hydrogen Diffusion Mode on Particle Loading. Table 3 summarizes the correlation between the value of Kn and the diffusion behavior of the hydrogen molecules. It can be seen that the diffusion mode of the hydrogen molecules changes from anomalous diffusion to ballistic diffusion as the value of Kn decreases.

Figure 5 shows the variation of the hydrogen self-diffusion coefficient with the particle loading in the range of 10~120 No/Å as a function of the simulation temperature. The results show that the diffusion coefficient increases exponentially with an increasing particle loading. (Note that the loading is plotted in logarithmic scale.) For a loading of less than approximately 30 molecules, the diffusion coefficient is independent of the number of molecules within the CNT and is determined primarily by the effects of the interactions between the molecules and the tube wall. By contrast, for

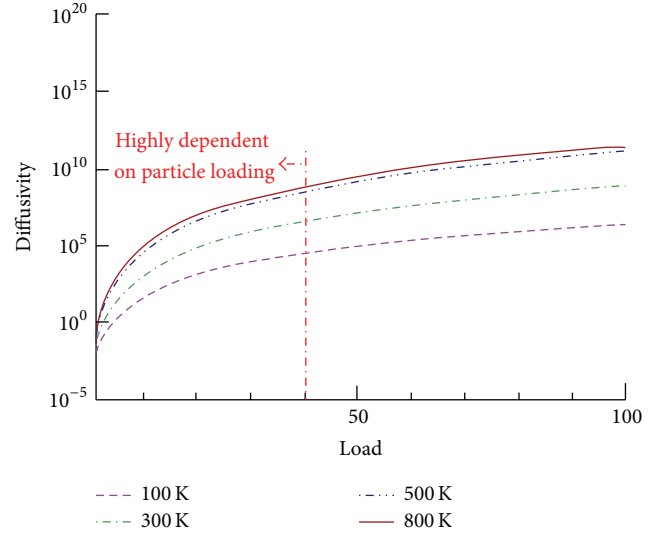


FIGURE 5: Self-diffusion coefficients. Note that the lines represent the best-fitting approximation for each set of simulation results.

loadings greater than 30 molecules, the diffusion coefficient increases rapidly as the number of molecules is increased. As the loading increases, the mean free path decreases as a result of the greater collision frequency. Consequently, at higher particle loadings, the coefficient diffusion is dominated by the interdiffusant collision frequency rather than the interaction effects of the nanotube wall. As shown in Figure 5, each curve tends to approach toward a limiting value of diffusion coefficient at temperature of 100 K, 300 K, 500 K, and 800 K respectively. In Figure 5, simulation results also show that the diffusion coefficient of hydrogen inside SWCNT exists as a limiting value of $3.04 \times 10^{-3} \text{ m}^2 \text{ s}^{-1}$ with $Kn < 1$.

4. Conclusions

This study has performed a series of MD simulations to investigate the diffusion behavior of hydrogen molecules within a CNT of infinite length and a diameter of 10.8 Å. The simulations have considered temperatures in the range 100~800 K and particle loadings ranging from 1~120 molecules/nm. The diffusion of the hydrogen molecules under each of the considered simulation conditions has been quantified by computing the variation of the mean square displacement and the self-diffusion coefficient over time. In general, the results have shown the existence of three distinct diffusion regimes, depending on the value of the Knudsen number (Kn). For values of Kn greater than 1, the hydrogen molecules exhibit an anomalous diffusion mechanism (i.e., single-file or Fickian), whereas for values of Kn less than 1, the hydrogen molecules exhibit a ballistic behavior as a result of a thermally induced compression-relaxation of the hydrogen molecule crowds within the CNT. A concerted cluster-type motion was also observed for polymers [46, 47] and LJ fluid [19, 48] in SWCNTs. However, the present simulation results differ from the results presented in these studies in that the hydrogen bonds form crowds rather than clusters due to their low

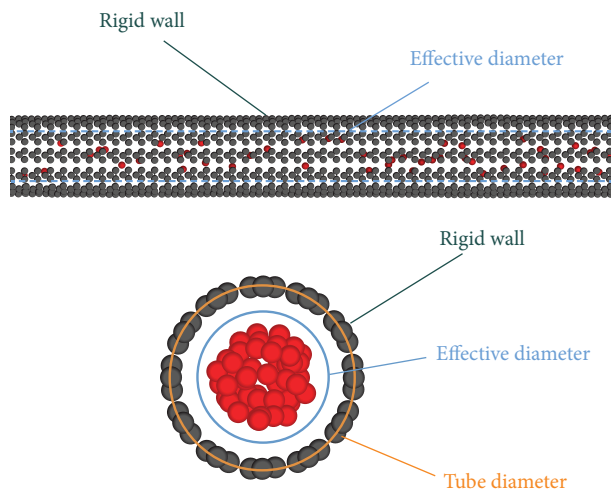


FIGURE 6: Hydrogen diffusion in rigid-lattice model (see also Animation A1, A2, in Supplementary Material available online at <http://dx.doi.org/10.1155/2014/959402>).

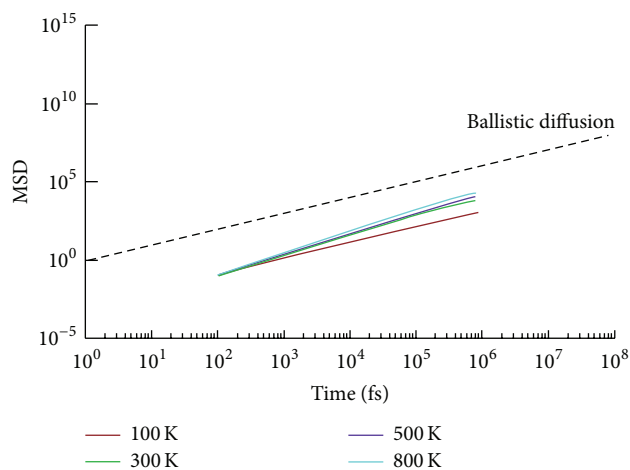


FIGURE 7: Mean square displacement curves of hydrogen molecules in the rigid-lattice SWNT as function of time for simulation temperatures of $T = 100$ K (red), 300 K (green), 500 K (blue), and 800 K (light blue), respectively. Note that particle loadings 70 adsorbed hydrogen molecules.

self-interaction potential. Furthermore, the ballistic motion of the hydrogen molecules prompted by the compression-relaxation process persists for a relatively long time (i.e., ~ 50 ps) compared to that of the clusters reported in [19, 43, 44]. Consequently, it is inferred that simulation time in the order of tens of nanoseconds is required to reliably estimate the self-diffusion coefficients of molecules confined within a narrow CNT. Recently, Sisan and Lichter proposed that the solitons can transport water in narrow CNTs [49]. This result may give the connection between quantum sieving and hydrogen storage in adsorbents.

Appendix

To provide the evidence to support the opinion of the influences between flexible and fixed lattice model, we conduct a rigid-lattice model to simulate the hydrogen diffusion inside SWNT for comparison purpose. The nanotubes considered here are described with carbon atoms fixed during the simulations. The self-diffusion coefficients predicted for simple fluids through rigid SWCNTs can be faster than those predicted through flexible SWCNTs [35]. This effect is important at low loadings and becomes less important as the loading density increases. For the scope of the present work, which is to investigate the mechanism of hydrogen molecules diffusion within narrow SWCNTs, it is unreasonable to consider rigid SWCNTs for saving computation effort since two types of carbon atom vibrations are expected to affect the tendency of adsorbed hydrogen molecules. This study performs a series of molecular dynamics simulations to investigate the transport properties of hydrogen molecules confined within a rigid carbon nanotube with a diameter of 10.8 \AA at temperatures in the range of $100\text{--}800 \text{ K}$ and high particle loadings 1 No/\AA . We never observe the MSD curves jump behavior on rigid-lattice model. To assess the reliability of our results, we repeat selected simulation runs with different initial conditions. No significant difference was noticed on the conclusions here reported (see Figures 6 and 7).

Conflict of Interests

The authors declare that there is no conflict of interests regarding the publication of this paper.

Acknowledgment

The authors gratefully acknowledge the financial support provided to this study by Ministry of Science and Technology under no. 102-2221-E-269-019 -.

References

- [1] L. Schlapbach and A. Züttel, "Hydrogen-storage materials for mobile applications," *Nature*, vol. 414, no. 6861, pp. 353–358, 2001.
- [2] H.-H. Rogner, "Hydrogen technologies and the technology learning curve," *International Journal of Hydrogen Energy*, vol. 23, no. 9, pp. 833–840, 1998.
- [3] A. C. Dillon, K. M. Jones, T. A. Bekkedahl, C. H. Kiang, D. S. Bethune, and M. J. Heben, "Storage of hydrogen in single-walled carbon nanotubes," *Nature*, vol. 386, no. 6623, pp. 377–379, 1997.
- [4] R. M. de Vos and H. Verweij, "High-selectivity, high-flux silica membranes for gas separation," *Science*, vol. 279, no. 5357, pp. 1710–1711, 1998.
- [5] L. N. Gergidis and D. N. Theodorou, "Molecular dynamics simulation of n-butane-methane mixtures in silicalite," *Journal of Physical Chemistry B*, vol. 103, no. 17, pp. 3380–3390, 1999.
- [6] Z. Mao and S. B. Sinnott, "Separation of organic molecular mixtures in carbon nanotubes and bundles: molecular dynamics

- simulations,” *Journal of Physical Chemistry B*, vol. 105, no. 29, pp. 6916–6924, 2001.
- [7] K. T. Thomson and R. M. Wentzcovitch, “A density functional study of the electronic structure of sodalite,” *The Journal of Chemical Physics*, vol. 108, no. 20, pp. 8584–8588, 1998.
- [8] S. J. Gregg and K. S. W. Sing, *Adsorption, Surface Area and Porosity*, Academic Press, London, UK, 2nd edition, 1982.
- [9] J. Zou, B. Ji, X.-Q. Feng, and H. Gao, “Self-assembly of single-walled carbon nanotubes into multi walled carbon nanotubes in water: molecular dynamics simulations,” *Nano Letters*, vol. 6, no. 3, pp. 430–434, 2006.
- [10] I. A. Khan and K. G. Ayappa, “Density distributions of diatoms in carbon nanotubes: a grand canonical Monte Carlo study,” *Journal of Chemical Physics*, vol. 109, no. 11, pp. 4576–4586, 1998.
- [11] I. Brovchenko, A. Geiger, and A. Oleinikova, “Phase equilibria of water in cylindrical nanopores,” *Physical Chemistry Chemical Physics*, vol. 3, no. 9, pp. 1567–1569, 2001.
- [12] A. Giaya and R. W. Thompson, “Water confined in cylindrical micropores,” *The Journal of Chemical Physics*, vol. 117, no. 7, pp. 3464–3475, 2002.
- [13] W. H. Noon, K. D. Ausman, R. E. Smalley, and M. Jianpeng, “Helical ice-sheets inside carbon nanotubes in the physiological condition,” *Chemical Physics Letters*, vol. 355, no. 5-6, pp. 445–448, 2002.
- [14] A. Striolo, A. A. Chialvo, K. E. Gubbins, and P. T. Cummings, “Water in carbon nanotubes: adsorption isotherms and thermodynamic properties from molecular simulation,” *Journal of Chemical Physics*, vol. 122, no. 23, Article ID 234712, 2005.
- [15] A. Striolo, K. E. Gubbins, M. S. Gruszkiewicz et al., “Effect of temperature on the adsorption of water in porous carbons,” *Langmuir*, vol. 21, no. 21, pp. 9457–9467, 2005.
- [16] A. Striolo, A. A. Chialvo, P. T. Cummings, and K. E. Gubbins, “Simulated water adsorption in chemically heterogeneous carbon nanotubes,” *Journal of Chemical Physics*, vol. 124, no. 7, Article ID 074710, 2006.
- [17] Z. Mao and S. B. Sinnott, “A computational study of molecular diffusion and dynamic flow through carbon nanotubes,” *Journal of Physical Chemistry B*, vol. 104, no. 19, pp. 4618–4624, 2000.
- [18] Z. Mao, A. Garg, and S. B. Sinnott, “Molecular dynamics simulations of the filling and decorating of carbon nanotubes,” *Nanotechnology*, vol. 10, article 273, 1999.
- [19] D. M. Ackerman, A. I. Skoulidas, D. S. Sholl, and J. K. Johnson, “Diffusivities of Ar and Ne in carbon nanotubes,” *Molecular Simulation*, vol. 29, no. 10-11, pp. 677–684, 2003.
- [20] A. I. Skoulidas, D. M. Ackerman, J. K. Johnson, and D. S. Sholl, “Rapid transport of gases in carbon nanotubes,” *Physical Review Letters*, vol. 89, no. 18, 2002.
- [21] R. E. Tuzun, D. W. Noid, B. G. Sumpter, and R. C. Merkle, “Dynamics of He/C60 flow inside carbon nanotubes,” *Nanotechnology*, vol. 8, no. 3, pp. 112–118, 1997.
- [22] T. J. H. Vlugt and M. Schenk, “Influence of framework flexibility on the adsorption properties of hydrocarbons in the zeolite silicalit,” *Journal of Physical Chemistry B*, vol. 106, no. 49, pp. 12757–12763, 2002.
- [23] P. Demontis and G. B. Suffritti, “Structure and dynamics of zeolites investigated by molecular dynamics,” *Chemical Reviews*, vol. 97, no. 8, pp. 2845–2878, 1997.
- [24] S. Jakobtorweihen, M. G. Verbeek, C. P. Lowe, F. J. Keil, and B. Smit, “Understanding the loading dependence of self-diffusion in carbon nanotubes,” *Physical Review Letters*, vol. 95, no. 4, Article ID 044501, 2005.
- [25] K. G. Ayappa, “Simulations of binary mixture adsorption in carbon nanotubes: transitions in adsorbed fluid composition,” *Langmuir*, vol. 14, no. 4, pp. 880–890, 1998.
- [26] Y. Guo, N. Karasawa, and W. A. Goddard III, “Prediction of fullerene packing in C₆₀ and C₇₀ crystals,” *Nature*, vol. 351, no. 6326, pp. 464–467, 1991.
- [27] W. A. Steele, *The Interaction of Gas with Solid Surfaces*, Pergamon Press, Oxford, UK, 1974.
- [28] J. Kärger and D. M. Ruthven, *Diffusion in Zeolites and Other Microporous Solids*, John Wiley & Sons, New York, NY, USA, 1992.
- [29] G. Karniadakis, A. Beskok, and N. Aluru, *Micro Flows: Fundamentals and Simulation*, Springer, 2001.
- [30] R. C. Reid, J. M. Prausnitz, and B. E. Poling, *Properties of Gases and Liquids*, McGraw-Hill, New York, NY, USA, 1987.
- [31] O. Reynolds, “On certain dimensional properties of matter in the gaseous state. Part I. Experimental researches on thermal transpiration of gases through porous plates and on the laws of transpiration and impulsion, including an experimental proof that gas is not a continuous plenum. Part II. On an extension of the dynamical theory of gas, which includes the stresses, tangential and normal, caused by a varying condition of gas, and affords an explanation of the phenomena of transpiration and impulsion,” *Philosophical Transactions of the Royal Society of London*, vol. 170, pp. 727–845, 1879.
- [32] M. Knudsen, “Eine Revision der Gleichgewichtsbedingung der Gase. Thermische Molekularströmung,” *Annals of Physics*, vol. 31, pp. 205–229, 1910.
- [33] M. Knudsen, “Thermischer Molekulardruck der Gase in Röhren,” *Annals of Physics*, vol. 338, pp. 1435–1448, 1910.
- [34] L. B. Loeb, “Kinetic theory of gases,” *Journal of the American Chemical Society*, vol. 81, no. 5, pp. 1267–1267, 1959.
- [35] R. E. Tuzun, D. W. Noid, B. G. Sumpter, and R. C. Merkle, “Dynamics of He/C60 flow inside carbon nanotubes,” *Nanotechnology*, vol. 7, p. 241, 1996.
- [36] Y. Guo, N. Karasawa, and W. A. Goddard III, “Prediction of fullerene packing in C60 and C70 crystals,” *Nature*, vol. 351, no. 6326, pp. 464–467, 1991.
- [37] A. K. Rappé, C. J. Casewit, K. S. Colwell, W. A. Goddard III, and W. M. Skiff, “UFF, a full periodic table force field for molecular mechanics and molecular dynamics simulations,” *Journal of the American Chemical Society*, vol. 114, no. 25, pp. 10024–10035, 1992.
- [38] S. Schaaf and P. Chambre, *Flow of Rarefied Gases*, Princeton University Press, Princeton, NJ, USA, 1961.
- [39] M. Majumder, N. Chopra, R. Andrews, and B. J. Hinds, “Nanoscale hydrodynamics: enhanced flow in carbon nanotubes,” *Nature*, vol. 438, no. 7064, p. 44, 2005.
- [40] G. Hummer, J. C. Rasaiah, and J. P. Noworyta, “Water conduction through the hydrophobic channel of a carbon nanotube,” *Nature*, vol. 414, no. 6860, pp. 188–190, 2001.
- [41] P. A. Thompson and S. M. Troian, “A general boundary condition for liquid flow at solid surfaces,” *Nature*, vol. 389, no. 6649, pp. 360–362, 1997.
- [42] K. P. Travis, B. D. Todd, and D. J. Evans, “Departure from Navier-Stokes hydrodynamics in confined liquids,” *Physical Review E: Statistical Physics, Plasmas, Fluids, and Related Interdisciplinary Topics*, vol. 55, no. 4, pp. 4288–4295, 1997.
- [43] K. P. Travis and K. E. Gubbins, “Poiseuille flow of Lennard-Jones fluids in narrow slit pores,” *Journal of Chemical Physics*, vol. 112, no. 4, pp. 1984–1994, 2000.

- [44] H. Ebert and K. R. Albrand, "The applicability of gas flows in the molecular range," *Vacuum*, vol. 13, no. 12, pp. 563–568, 1963.
- [45] T. R. Cuthbert, N. J. Wagner, M. E. Paulaitis, G. Murgia, and B. D'Aguanno, "Molecular dynamics simulation of penetrant diffusion in amorphous polypropylene: diffusion mechanisms and simulation size effects," *Macromolecules*, vol. 32, no. 15, pp. 5017–5028, 1999.
- [46] A. Striolo, "The mechanism of water diffusion in narrow carbon nanotubes," *Nano Letters*, vol. 6, no. 4, pp. 633–639, 2006.
- [47] C. Wei and D. Strivastava, "Theory of transport of long polymer molecules through carbon nanotube channels," *Physical Review Letters*, vol. 91, Article ID 235901, pp. 1–4, 2003.
- [48] H. Chen, J. K. Johnson, and D. S. Sholl, "Transport diffusion of gases is rapid in flexible carbon nanotubes," *Journal of Physical Chemistry B*, vol. 110, no. 5, pp. 1971–1975, 2006.
- [49] T. B. Sisan and S. Lichter, "Solitons transport water through narrow carbon nanotubes," *Physical Review Letters*, vol. 112, no. 4, Article ID 044501, 2014.

Research Article

Preparation and Flame Retardant and Smoke Suppression Properties of Bamboo-Wood Hybrid Scrimber Filled with Calcium and Magnesium Nanoparticles

Bin Fu, Xingong Li, Guangming Yuan, Weimin Chen, and Yage Pan

Central South University of Forestry and Technology, Institute of Materials Science and Engineering, Changsha, Hunan 410004, China

Correspondence should be addressed to Xingong Li; lxgwood@163.com

Received 22 April 2014; Revised 22 June 2014; Accepted 2 July 2014; Published 16 July 2014

Academic Editor: Jihua Gou

Copyright © 2014 Bin Fu et al. This is an open access article distributed under the Creative Commons Attribution License, which permits unrestricted use, distribution, and reproduction in any medium, provided the original work is properly cited.

The physical and mechanical properties of bamboo-wood hybrid scrimber filled with different loadings of nanoparticles were studied. The effects of nanoparticles on flame retardant and smoke suppression properties of bamboo-wood hybrid scrimber were studied by means of thermogravimetric analysis (TGA), cone calorimeter (CONE), and scanning electron microscope (SEM). The results showed that the physical and mechanical properties of bamboo-wood hybrid scrimber were improved by adding a moderate loading of nanoparticles; the optimal loading of nanoparticles was 10%. The heat transfer in bamboo-wood hybrid scrimber was prevented and the escaping channel of combustible gas was blocked by the uniformly filling effect of nanoparticles. The gas concentration was diluted by the noncombustible gas produced by pyrolysis of nanoparticles; the combustion chain reaction was suppressed by highly reactive free radicals produced by pyrolysis of nanoparticles. The residual mass of bamboo-wood hybrid scrimber filled with nanoparticles in thermogravimetric (TG) curve at 900 s and burned by method of cone calorimeter (CONE) at 600 s was increased compared to that of untreated one, which showed that inorganic mineral powder has the effect of catalytic charring.

1. Introduction

The process of production of traditional wood particle board and fiber board deteriorated the natural wood texture and influenced the properties of raw materials. As for the bamboo based panels, there are a number of shortcomings including being hard to glue, difficult machining, and a low utilization rate of raw material [1, 2]. The bamboo-wood hybrid scrimber which is prepared by different bamboo-wood hybrid ratio has high specific modulus and specific strength. Furthermore, it can not only keep the texture direction of raw material in a great extent, fully showing their respective advantages, but also reduce the production cost, increasing the value of the fast-growing timber [3, 4]. Bamboo-wood hybrid scrimber can be widely used in furniture, flooring, and building materials industries; all these areas require products which are flame retardant. In recent years China has seen the frequency of fires increase. The resulting damages, in both life and

property, has meant that research on the flame retardant and smoke suppression nature of bamboo-wood hybrid scrimber has become more and more important. Natural inorganic mineral powder has the advantages of being nontoxic, being noncorrosive, and being of cheap price. The channels which used for water absorption and free formaldehyde release can be blocked by a small amount of nanoparticles that filled in bamboo-wood hybrid scrimber, the physical and mechanical properties and environmental property of bamboo-wood hybrid scrimber can be improved as well [5, 6]. Nanoparticles have the property of flame retardant; some nanoparticles also can be decomposed to produce noncombustible gases to block the smoke release channel in bamboo-wood hybrid scrimber at high temperature, that makes it have the function of flame retardant and smoke suppression. In recent years, reports of inorganic mineral powder research are mainly focused on the effect on physical and mechanical properties of materials, while this paper is about the preparation of

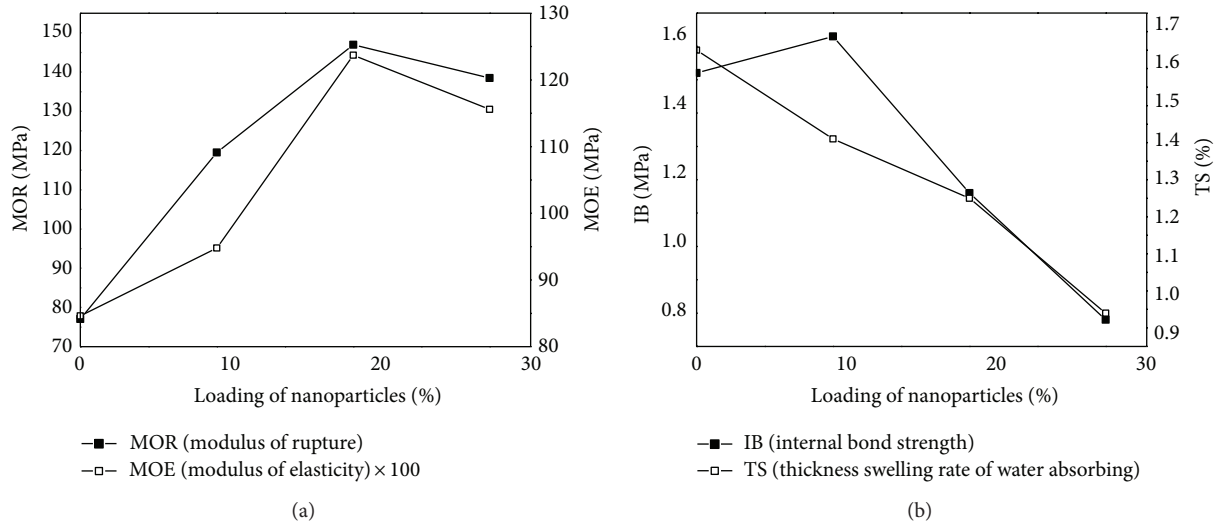


FIGURE 1: The physical and mechanical properties of bamboo-wood hybrid scrimber filled with different loadings of nanoparticles.

bamboo-wood hybrid scrimber made by bamboo, wood, and phenol formaldehyde resin (PF) and the effect of nanoparticles on the flame retardant and smoke suppression properties of bamboo-wood hybrid scrimber.

2. Materials and Methods

2.1. Raw Materials

Bamboo. From Taohuajiang bamboo industry Co., Ltd. in Yiyang Hunan province. Age of bamboo is 4-5 years old, diameter at breast height (DBH) is 60–80 mm, thickness of bamboo wall is 3–5 mm, and moisture content is around 12%.

Eucalyptus. From Taohuajiang bamboo industry Co., Ltd. in Yiyang Hunan province. Moisture content is around 12%.

Water-Soluble Phenolic-Formaldehyde Resin (PF). From Taohuajiang bamboo industry Co., Ltd. in Yiyang Hunan province. Appearance is brown red liquid, solid content is 51.2%, viscosity is 280–360 mPa·s (20°C), and PH is 10.53.

Nanoparticles. Diameter is 5–50 nm and main ingredients are CaCO_3 , CaO , MgCO_3 , and MgO .

2.2. The Preparation and Performance Test of Bamboo-Wood Hybrid Scrimber. The bamboo-wood hybrid ratio was 3:2, solid content of adhesive was 25%. Adding a certain amount of nanoparticles into the PF, stir evenly, put the bamboo strips and wood strips into the PF and completely soak it for 10 min, then take them out, and put them into the drying oven for 3 hours under 60°C after there is no drop of glue liquid dropping out. Assembly pattern is achieved by “Bamboo layer-wood layer-bamboo layer” in a longitudinal uniform arranged way [7], the slab design density was 1.1 g/cm^3 , size is $400 \times 250 \times 16 \text{ mm}$, using hot pressing process in which

the hot board comes in and the cold board goes out. Hot process temperature is 150°C, hot process time is 1.5 min/mm, and unloading the plates temperature is 50°C. For cone test, 5 specimens were tested for each sample and took the average.

Detection method on physical and mechanical properties of bamboo-wood hybrid scrimber was according to GB/T 7657.4-2003.

2.3. Thermogravimetric Analysis (TGA). Thermogravimetric (TG) and differential scanning calorimetry (DSC) analysis of the specimen were researched by STA449C thermobalance from NETZSCH Company in Germany. 10–15 mg samples powder was weighed in Al_2O_3 crucible; test temperature scope is 40°C–1000°C; heating rate (β) is 10°C/min, using N_2 as shielding gas.

2.4. Cone Calorimeter (CONE). The specimen was researched by cone calorimeter (Stanton Redcroft), radiant heat flux is 50 KW/m^2 which was close to the actual fire intensity 780°C, specimen size is $100 \times 100 \times 10 \text{ mm}$, and time to ignition (TTI) was recorded by man, using origin software for data processing.

2.5. SEM Analysis. The specimen was analyzed by scanning electron microscope quanta 450, and the specimen section was fixed and on the specimen stage by conducting carbon cloth rubber, flattened, and then dried on the heating plate; specimen surface was plated with 3 nm platinum by ion sputtering apparatus. Working voltage is 20 kV, accelerating current is 15 mA, and working distance is 15 mm.

3. Results and Discussion

3.1. The Effect on Physical and Mechanical Properties of Bamboo-Wood Hybrid Scrimber Filled with Different Loadings of Nanoparticles. Figure 1 is the physical and mechanical

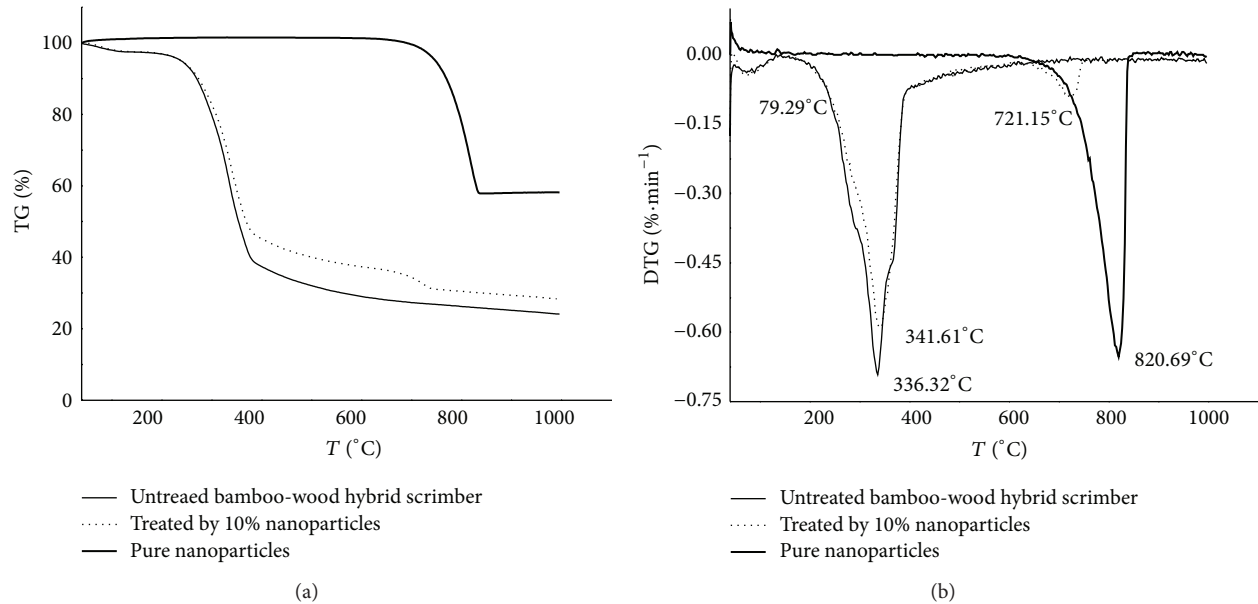


FIGURE 2: The TG, DTG curves of bamboo-wood hybrid scrimber and nanoparticles.

properties of bamboo-wood hybrid scrimber filled with different loadings of nanoparticles; it shows that each mechanical property of bamboo-wood hybrid scrimber was improved by the treatment of 10% nanoparticles; Modulus of Rupture (MOR), Modulus of Elasticity (MOE), and Internal Bond (IB) strength were increased. Thickness Swelling (TS) rate of water absorbing was decreased. This is because nanoparticles were in a fine powder shape, nanoparticles can fill into the porosity of the bamboo-wood hybrid scrimber with the glue, then fix the glue into the porosity of the bamboo-wood hybrid scrimber. The whole plate becomes more close-grained, and organizational units junction increases; the local stress concentration was decreased, bonding strength becomes stronger, and moisture absorption channels can also be blocked by nanoparticles; this will improve the dimension stability of bamboo-wood hybrid scrimber [8, 9]. Internal Bond strength of bamboo-wood hybrid scrimber will be decreased if the loading of nanoparticles was over 10%; this is because nanoparticles have bad compatibility with the base. It is easy to de-bond the connection between rigid particles and base if the bamboo-wood hybrid scrimber was under external force because of the bad compatibility. Adhesives' unit effective components in the surface area of bamboo strip and eucalyptus strip are reduced owing to the excess nanometer inorganic mineral powder added in, and as a consequence of the weak boundary layer was formed between bamboo strip and adjacent bamboo strip, bamboo strip and adjacent wood strip, and wood strip and adjacent wood strip [10, 11]. Based on the analysis above, the optimal loading of nanoparticles was 10%.

3.2. Thermogravimetric Analysis (TGA). Figure 2 is the thermogravimetric (TG) and derivative thermogravimetric analysis (DTG) curve of bamboo-wood hybrid scrimber filled with 10% nanoparticles, untreated bamboo-wood hybrid

scrimber, and pure inorganic mineral powder. The figure showed that the pyrolysis processing of bamboo-wood hybrid scrimber has experienced three stages of the loss of free water, pyrolysis, and the end of thermal decomposition of coke [12], while the pyrolysis processing of bamboo-wood hybrid scrimber filled with nanoparticles has experienced four stages of the loss of free water, pyrolysis, pyrolysis of nanoparticles, and the end of thermal decomposition of coke and pure nanoparticles have experienced just one stage of pyrolysis processing. Figure 2(b) showed that in the main pyrolysis stage, the DTG peak temperature of bamboo-wood hybrid scrimber filled with nanoparticles moves to slightly higher temperature compared to untreated one and the size of DTG peak was reduced by 13.6% compared to the untreated one; all of these proved that nanoparticles can restrain the pyrolysis of bamboo-wood hybrid scrimber. The residual quantity of bamboo-wood hybrid scrimber filled with nanoparticles (remove 10% mineral powder quality after pyrolysis) was increased by 3.09% compared to untreated one at 900°C, and this shows that bamboo-wood hybrid scrimber has the function of catalytic charring.

3.3. Cone Calorimeter (CONE). Table 1 is the main combustion characteristic data of bamboo-wood hybrid scrimber filled with nanoparticles and untreated one. Table 1 showed that time to ignition (TTI) of bamboo-wood hybrid scrimber filled with nanoparticles was lengthened compared to the untreated one. This is because the incombustibility nanoparticles distributed on the surface of bamboo-wood hybrid scrimber delayed the time to burn. The residual quality of bamboo-wood hybrid scrimber filled with nanoparticles increased by 30.07% compared to untreated one after 600 s of combustion. This showed that bamboo-wood hybrid scrimber has the function of catalytic charring. This result is in line with the TG results.

TABLE 1: The main combustion characteristic data of bamboo-wood hybrid scrimber (radiant heat flux 50 kW/m^2).

Sample	TTI (s)	M_{600} (%)	pk-HRR1 (t_1) ($\text{kW}\cdot\text{m}^{-2}$)	pk-HRR2 (t_2) ($\text{kW}\cdot\text{m}^{-2}$)	a-SEA ($\text{m}^2\cdot\text{kg}^{-1}$)	pk-SEA1 (t_1) ($\text{m}^2\cdot\text{kg}^{-1}$)
Untreated one	30	29.40	198.23 (75 s)	272.11 (555 s)	83.07	519.54 (25)
Treated by 10% nanoparticles	37	38.24	178.46 (65 s)	184.41 (585 s)	55.62	398.89 (20)

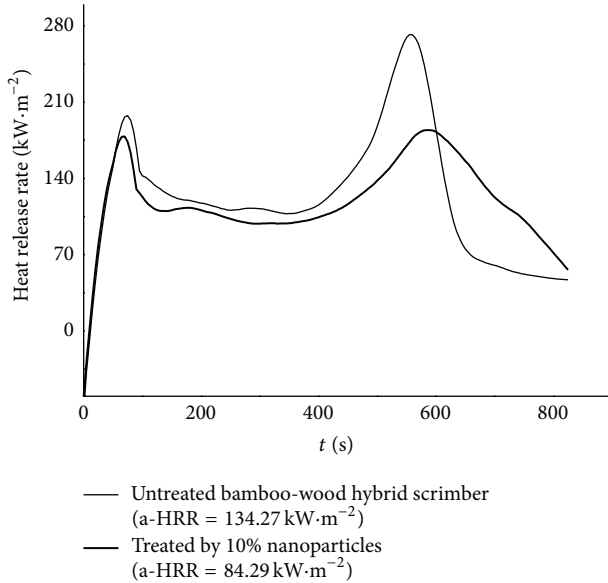


FIGURE 3: The HRR curves of bamboo-wood hybrid scrimber.

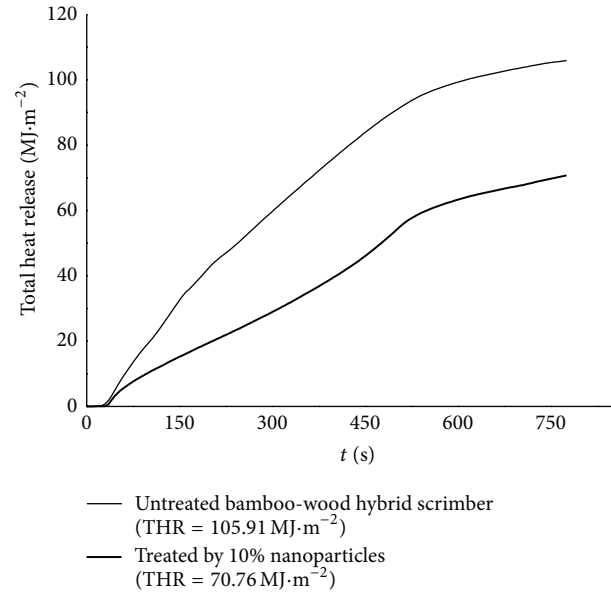


FIGURE 4: The THR curves of bamboo-wood hybrid scrimber.

Figures 3 and 4 are heat release rate (HRR) curve and total heat release (THR) curve of bamboo-wood hybrid scrimber filled with nanoparticles and untreated one. From Figure 3, Figure 4, and Table 1 we can know that the average heat release rate (a-HRR) and the quantity of total heat release (THR) of bamboo-wood hybrid scrimber filled with nanoparticles were decreased by 37.22% and 33.19% compared to untreated one, and two peaks of heat release rate of bamboo-wood hybrid scrimber filled with nanoparticles were decreased by 9.97% and 32.23%; this showed that combustion exothermic reaction in bamboo-wood hybrid scrimber can be restrained by nanoparticles, and that is because nanoparticle has the flame retardant property and a low heat transfer coefficient, uniformly distributed in the bamboo-wood hybrid scrimber to prevent heat from transferring and block the escape channel of combustible volatiles produced by the process of bamboo-wood hybrid scrimber pyrolysis. Nanoparticles contain a large amount of CaCO_3 and MgCO_3 , decomposition reaction is endothermic reaction at high temperature, so they will absorb the heat around to decrease the temperature of the surface and burned area, and carbon dioxide produced by decomposition can dilute the concentration of combustible gas and oxygen around to suppress the combustion. A large amount of highly reactive free radicals HO^\bullet and H^\bullet produced by the combustion of bamboo-wood hybrid scrimber are closely related to the speed of combustion, nanoparticles decomposed at high temperature, and free radicals were

produced by chemical bond rupture. These free radicals reacted with highly reactive free radicals HO^\bullet and H^\bullet , so the combustion chain reaction was suppressed by highly reactive free radicals [13].

Figure 5 is the total smoke rate (TSR) curve of bamboo-wood hybrid scrimber filled with nanoparticles and untreated one. Figure 5 and Table 1 show that TSP of bamboo-wood hybrid scrimber filled with nanoparticles was decreased by 29.47% compared to untreated bamboo-wood hybrid scrimber after 900 s of combustion, the values of average extinction area (a-SEA) was decreased by 33.04%, this proved that bamboo-wood hybrid scrimber filled with nanoparticles has the function of smoke suppression, and that is because nanoparticles blocked the escape channel of smoke in bamboo-wood hybrid scrimber.

3.4. SEM Analysis (SEM). Figures 6 and 7 are the carbon residue SEM figure of untreated bamboo-wood hybrid scrimber and bamboo-wood hybrid scrimber filled with nanoparticles. Figure 6 showed that the charcoal layer of the untreated bamboo-wood hybrid scrimber after combustion was cracked and was in a loose shape. This is because a large sum of the smoke produced by combustion inside has impact to the material itself; after charcoal layer cracked, heat and oxygen are easy to enter inside with the combustible gas coming out, and it is a threat for the material used for retarding fire. Figure 7 showed that nanoparticles are

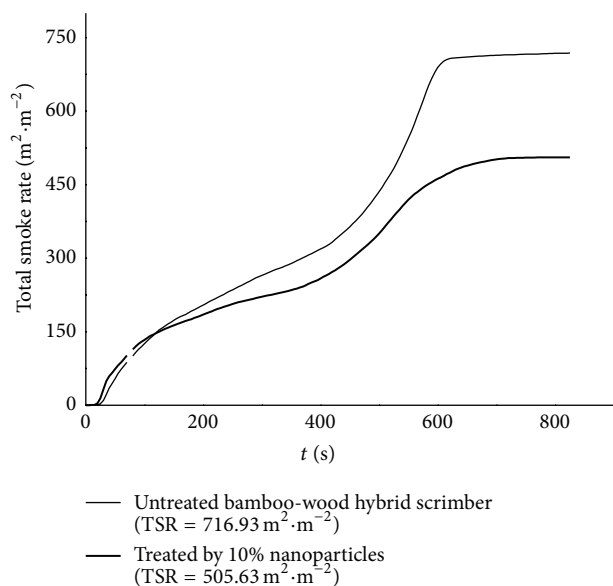


FIGURE 5: The TSR curves of bamboo-wood hybrid scrimber.

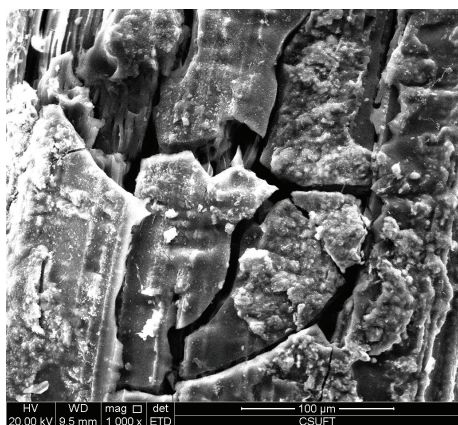


FIGURE 6: The carbon residue SEM figure of untreated bamboo-wood hybrid scrimber.

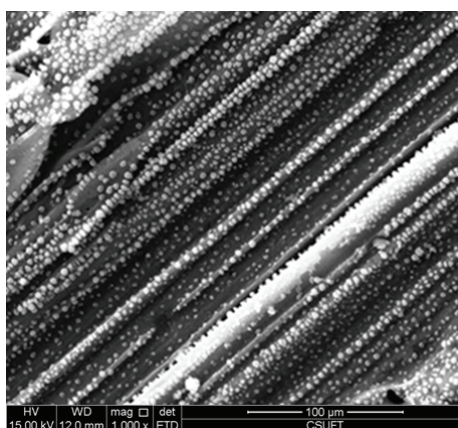


FIGURE 7: The carbon residue SEM figure of bamboo-wood hybrid scrimber filled with nanoparticles.

uniformly distributed in the charcoal layer of bamboo-wood hybrid scrimber, residual coal surface of bamboo-wood hybrid scrimber filled with nanoparticles was dense and was regularly arranged after combustion; that is because the hard CaO and MgO produced by decomposition of CaCO_3 and MgCO_3 formed a coating on the surface of material to inhibit the release of combustible gas and smoke and isolate oxygen from outside [14], as well as preventing the heat transfer. CaO and MgO have flame retardant properties, uniformly distributing in the bamboo-wood hybrid scrimber to prevent the heat from transferring and block the escape channel of the combustible gas.

4. Conclusions

- (1) The physical and mechanical properties of bamboo-wood hybrid scrimber were improved by adding a moderate loading of nanoparticles; the optimal loading of nanoparticles was 10%.
- (2) Bamboo-wood hybrid scrimber thermal weight loss maximum rate's temperature can be improved by the nanoparticles, the numerical of thermal weight loss maximum rate was decreased as well, and it has the function of restraining the pyrolysis of bamboo-wood hybrid scrimber. The residual quantity of bamboo-wood hybrid scrimber filled with nanoparticles was increased, and it has the function of flame retardant and catalytic charring. Residual coal surface of bamboo-wood hybrid scrimber filled with nanoparticles was dense and was regularly arranged after combustion; this kind of construction inhibited the release of combustible gas and smoke and isolated oxygen from outside, as well as preventing bamboo-wood hybrid scrimber to burn.
- (3) The heat transfer in bamboo-wood hybrid scrimber was prevented and the escaping channel of combustible gas was blocked by the uniformly filling effect of nanoparticles. The gas concentration was diluted by the noncombustible gas produced by pyrolysis of nanometer inorganic mineral powder, and the combustion chain reaction was suppressed by highly reactive free radicals produced by pyrolysis of nanometer inorganic mineral powder.

Conflict of Interests

The authors declare that there is no conflict of interests regarding the publication of this paper.

Acknowledgments

Xingong Li would like to thank and appreciate all authors for their valued contributions and to all potential reviewers for sparing their valuable time, efforts, and constructive comments for this special issue. This work is supported by the following foundation items: the National Natural Science Foundation (31370569), the Hunan major science and technology projects (2011FJ1006), and the major scientific

research projects of Public Welfare Profession of national forestry (201204702).

References

- [1] N. Nugroho and N. Ando, "Development of structural composite products made from bamboo I: Fundamental properties of bamboo zephyr board," *Journal of Wood Science*, vol. 46, no. 1, pp. 68–74, 2000.
- [2] L. Qin and H. Xiqi, "The development and prospect ion of reconsolidated bamboo," *Journal of Bamboo Research*, vol. 20, no. 1, pp. 76–80, 2001.
- [3] Z. Jiang, G. Wang, B. Fei, and W. Yu, "The research and development on bamboo-wood composite materials," *Forest Research*, vol. 15, no. 6, pp. 712–718, 2002.
- [4] M. Ahmad and F. A. Kamke, "Analysis of Calcutta bamboo for structural composite materials: physical and mechanical properties," *Wood Science and Technology*, vol. 39, no. 6, pp. 448–459, 2005.
- [5] P. Jie, L. Bin, and W. Zhaobo, "The study on flame retardant performance of composite," *Function Materials*, vol. 16, no. 9, pp. 9–11, 2012.
- [6] B. Li, "Influence of polymer additives on thermal decomposition and smoke emission of poly(vinyl chloride)," *Polymer Degradation and Stability*, vol. 82, no. 3, pp. 467–476, 2003.
- [7] G. Donglan, *The Study on Key Technology and Performance of Bamboo-Wood Hybrid Scrimber*, Nanjing University, Nanjing, China, 2008.
- [8] N. Nugroho and N. Ando, "Development of structural composite products made from bamboo I: fundamental properties of bamboo zephyr board," *Journal of Wood Science*, vol. 46, no. 1, pp. 68–74, 2000.
- [9] M. Ahmad and F. A. Kamke, "Analysis of Calcutta bamboo for structural composite materials: surface characteristics," *Wood Science and Technology*, vol. 37, no. 3-4, pp. 233–240, 2003.
- [10] K. Ghavami, "Bamboo as reinforcement in structural concrete elements," *Cement and Concrete Composites*, vol. 27, no. 6, pp. 637–649, 2005.
- [11] A. W. C. Lee, X. Bai, and A. P. Bangi, "Selected properties of laboratory-made laminated-bamboo lumber," *Holzforschung*, vol. 52, no. 2, pp. 207–210, 1998.
- [12] W. Lihua, W. Shurong, and L. Zhongyang, "Biomass multicomponent pyrolysis kinetics of model," *Journal of Zhejiang University (Engineering Science)*, vol. 2, no. 39, pp. 247–251, 2005.
- [13] Z. Jianjun, Z. Jinzong, and J. Quan, "The study on Burning performance and flame retardant mechanism of the MWNTs-OH/PET nanocomposites," *Function Materials*, vol. 1, no. 24, pp. 2–3, 2010.
- [14] Z. Weiping, Z. Guangzhong, and Z. Zejun, "The effect on combustion smoke of PVC with acid radical ion," *Chinese Plastics*, vol. 14, no. 6, pp. 59–62, 2010.

Research Article

The Nanomechanical and Tribological Properties of Restorative Dental Composites after Exposure in Different Types of Media

Hong-Yi Fan, Xue-Qi Gan, Yang Liu, Zhuo-Li Zhu, and Hai-Yang Yu

State Key Laboratory of Oral Diseases, West China Hospital of Stomatology, Sichuan University, Chengdu 610041, China

Correspondence should be addressed to Hai-Yang Yu; yhyang6812@scu.edu.cn

Received 24 April 2014; Accepted 23 June 2014; Published 8 July 2014

Academic Editor: Guang-Ping Zhang

Copyright © 2014 Hong-Yi Fan et al. This is an open access article distributed under the Creative Commons Attribution License, which permits unrestricted use, distribution, and reproduction in any medium, provided the original work is properly cited.

The aim of this study was to evaluate the effects of various acidic solutions on the surface mechanical properties of commercial resin composites with different microstructures (Filtek Z350 XT, TPH³, Durafill, and Superlux). Specimens were immersed in orange juice, cola, and distilled water for 5 days and the nanohardness, elastic modulus, and wear behavior of the samples were determined via the nanoindentation test and a reciprocating nanoscratch test. The nanoscratch morphology was observed using scanning electron microscopy (SEM) and the wear depth was recorded by scanning probe microscopy (SPM). The results indicate that the nanofilled resin composites had the greatest hardest and highest elastic modulus, whereas the microfilled composites exhibited the lowest nanohardness and elastic modulus values. SEM observations showed that all resin composites underwent erosion and surface degradation after immersion in acidic solutions. Furthermore, the wear resistance was influenced by the composition of the acidic solution and was correlated with the nanohardness and elastic modulus. The dominant wear mechanism changed from plastic deformation to delamination after immersion in acidic solutions.

1. Introduction

Nowadays, restorative resin composites are widely used for the direct restoration of teeth because of their durability and better aesthetic, biological, and mechanical properties [1]. These composites are subjected to a wide range of physical and chemical conditions in the mouth, including temperature variation, masticatory forces, and chemicals from food. These factors greatly influence the in vivo degradation or failure of resin composites. One important chemical factor is exposure to acidic solutions. In vivo studies indicate that the exposure of resin composites to low-pH liquids can negatively affect their mechanical properties [2, 3]. Several mechanisms have been proposed to explain the degradation and failure of these restorative materials. Acidic molecules may cause surface erosion that weakens the matrix-filler bonding and/or softens the matrix, resulting in bond failures in the outer layer of the filler [4].

The weakening of the matrix-filler bonding or the matrix itself might be reflected by the wear processes that occur

during mastication. Many researchers have studied the influence of low pH on the wear behavior of resin composites using microscopic and visual methods to measure wear [5–7]. Acidic solutions have been shown to reduce the wear resistance of resin composites [8]. These studies focused on the microtribology; the actual wear mechanism and its effect on the microstructure are very difficult to determine. Micromechanics research can sufficiently explain the damage caused by acidic solutions and their specific mechanisms of wear.

The nanomechanics of resin composites exposed to acid have not been thoroughly studied, and nanoindentation and nanoscratch methods have not been applied to this field. Nanoindentation technology is ideal for testing the material properties of composites at the micron and submicron scales. This method can be used to determine the local mechanical properties of a resin composite by measuring the indentation load-displacement response. This technology differs from others because there is no need to image the indentation area to confirm the mechanical properties [9]. Nanoscratch

experiments are performed in conjunction with indentation tests, and the nanotribological properties of resin-based composites are tested by scratching the surface, which can reveal damage and further clarify the wear mechanism of resin composites. The objective of this study was to use the nanoindentation and nanoscratch techniques to characterize the effects of acidic solutions on the surface degradation of resin composites.

2. Materials and Methods

2.1. Samples Preparation. Four commercially available dental resin composites with different matrix compositions and filler types were used (Table 1), including Filtek Z350 XT, TPH³, Durafill, and Superlux. A total of 15 specimens were prepared for each type of resin composite. A silicone rubber mold (a ring with a hole of diameter 15 mm and depth 2 mm) was placed on a piece of transparent film and Vaseline was used to avoid adhesion to the filled composites. The mold was placed on a glass slide, manually filled with a slight excess of resin composite (with care taken to minimize entrapped air), and covered with another glass slide. A light-curing unit (Translux Power Blue, LED-powered lamp, Heraeus Kulzer, Hanau, Germany) was used to harden the composites. The output light intensity was greater than 1100 mW/cm² and the spectral range was 410–500 nm. Both the upper and lower surfaces were cured for 40 s.

The hardened samples were removed from the mold and their test surfaces were wet-polished with 400-grit to 1,200-grit SiC papers to remove the resin-rich layer and obtain a standard surface finish for the test.

2.2. Immersion Solution Preparation. Three different immersion media, which are common beverages consumed by people worldwide, in which children and adolescents are the majority group consuming the drinks were used in this study (Table 2): (1) distilled water, (2) orange juice, and (3) Coca-Cola. Prior to the experiment, specimens were cleaned in distilled water using an ultrasonic bath and then placed in the immersion solutions.

2.3. Characterization of Mechanical Properties and Wear Behavior. The hardness and elastic modulus were determined by the nanoindentation test using a Hysitron TriboSCOPE nanoindenter with a Berkovich diamond tip. The functional area of the tip was calibrated using a silicon standard. The angle of the tip was 142° and the radius was approximately 100–200 nm. Nanoindentation was performed in air under ambient conditions and temperature was in the range of 28–32°C. Loading was performed by following a triangular profile with a maximum load of 6 mN. The loading and unloading rates were all 0.6 mN/s. Five indentations were made on the top of each specimen with a 5- μ m spacing between indentations.

The reciprocating nanoscratch tests were performed on the sample surface with a constant load of 5 mN and scratch length of 15 μ m [10]. The tip scratch velocity was 30 μ m/s.

The wear scars were observed by scanning probe microscopy (SPM).

2.4. SEM Observations. Representative samples from each group were selected for qualitative scanning electron microscopy (INSPECTE, Czech Republic) observations. The samples were immersed in different media and the wear damage caused by the nanoscratch test was observed by SEM.

2.5. Statistical Analysis. All data were statistically analyzed (SPSS Statistics 17) by using one-way ANOVA test, followed by a LSD *t*-test ($P \leq 0.05$) for multiple comparisons between means to determine significant differences, which was used at a significance level set at $P \leq 0.05$.

3. Results and Discussion

The representative images of initial microstructures of the four composites before immersion in solutions are shown in the SEM micrograph in Figure 1. Resin composites are exposed to complex and varying intraoral conditions. Some substances with low pH values, such as beverages, may influence the chemical degradation of the composites. Degradation over time is inevitable and can be predicted by observing the decrease in wear resistance and loss of substance that occur under acidic conditions [11–13]. In this study, changes in the nanohardness, elastic modulus, and wear depth were measured to evaluate the degradation of dental materials exposed to different pH solutions.

The use of nanoindentation to measure the elastic modulus and nanohardness has several advantages. The tests are simple, reproducible, and relatively nondestructive. Nanohardness is obtained from the plastic depth rather than the final depth, similar to the permanent deformation used in microhardness calculations.

Figure 2 shows the means and standard deviations of nanohardness of nanoindentation between the diamond tip and the specimens that were immersed in distilled water, cola, or orange juice. The highest nanohardness was exhibited by specimen Z350 immersed in cola (0.58 ± 0.08 GPa) and the lowest value was found for Durafill immersed in orange juice (0.23 ± 0.02 GPa).

For resin Z350 treated with orange juice, the surface hardness was significantly higher ($P < 0.05$) compared to the distilled water treatment, although there was no significant difference in the nanohardness between the cola and orange juice treatments ($P = 0.213$).

The TPH³ composite resin showed a pattern similar to Z350; that is, it had significantly higher surface hardness after immersion in orange juice or cola compared to distilled water ($P < 0.05$). In addition, the nanohardness values were significantly different between the cola and orange juice treatments ($P < 0.05$).

For the Superlux material, there was a significant decrease in the surface hardness after treatment with cola. The hardness was lower than that obtained with distilled water, although it was greater than the value obtained for the orange

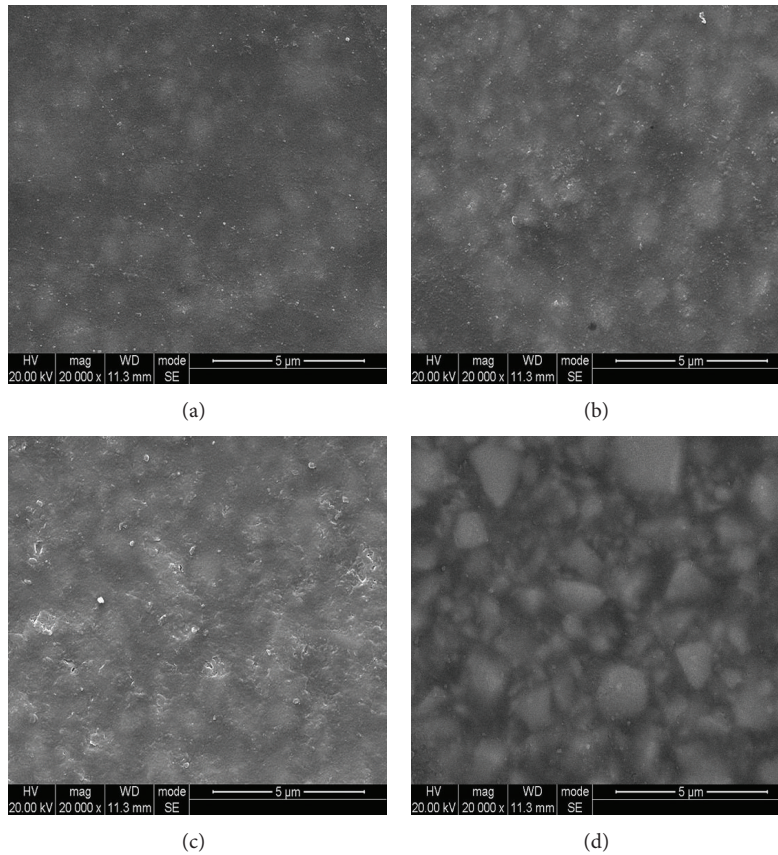


FIGURE 1: Representative SEM micrographs of resin-based composites before immersion in solutions. (a) Z350, (b) Superlux, (c) Durafill, and (d) TPH³.

TABLE 1: Specification of dental composites investigated in the present study.

Material	Manufacturer	Classification	Resin	Filler content	Filler type and size
FiltekTMZ350	3M ESPE, St. Paul, MN, USA	Nanofilled	BisGMA BisEMA TEGDMA UDMA	78.5 wt%	Zirconia and silica clusters: 0.6–1.4 μm
TPH ³	Dentsply Caulk, Milford, DE, USA	Nanohybrid	BisGMA BisEMA TEGDMA	75–77 wt%	BABS: <1 μm ; BAFG: <1 μm ; Silica: 10–20 nm
Durafill	VS Heraeus Kulzer, Hanau, Germany	Microfilled	UDMA	50.5 wt%	Prepolymerized silica: 10–20 μm ; silica: 0.02–2 μm
Superlux	DMG Germany	Microhybrid	TEGDMA BisGMA UDMA	66 wt%	SiO ₂ < 20 μm

juice treatment. For Durafill, the nanohardness was greater when treated with distilled water and the hardness values for orange juice and cola treatment were different from those obtained for the Superlux resin composite.

The elastic modulus describes the relative stiffness of a material. In stress-bearing occlusal contact areas, materials with a low modulus deform more under masticatory stresses and may cause a catastrophic failure (Figure 3). A high elastic

modulus is required to withstand deformation and cuspal fracture [14, 15].

Durafill exhibited the lowest elastic modulus values of the tested composites regardless of the treatment solution. The Durafill elastic modulus values were different for the various treatments ($P < 0.05$). For Z350, the elastic modulus was higher when treated with orange juice or cola than when treated with distilled water. However, for TPH³, the value for

TABLE 2: Immersion media used in the present study.

Material	Brand	Manufacture	pH	Ingredients
Distilled water	—	Laboratory	6.8	Water
Cola drink (coke)	Coca-Cola	Roppongi area of 6-2-31, Tokyo	2.9	High fructose corn syrup, sugar, food additive (caramel color, caffeine, and phosphoric acid), flavors agent, and carbonated water
Orange juice	Joos	470moo1, Sukhumvit Road, Bangpoomal, Muang, THAILAND	3.9	Water, sugar, orange pulp, orange juice concentrate, citric acid, pectin, and vitamin c

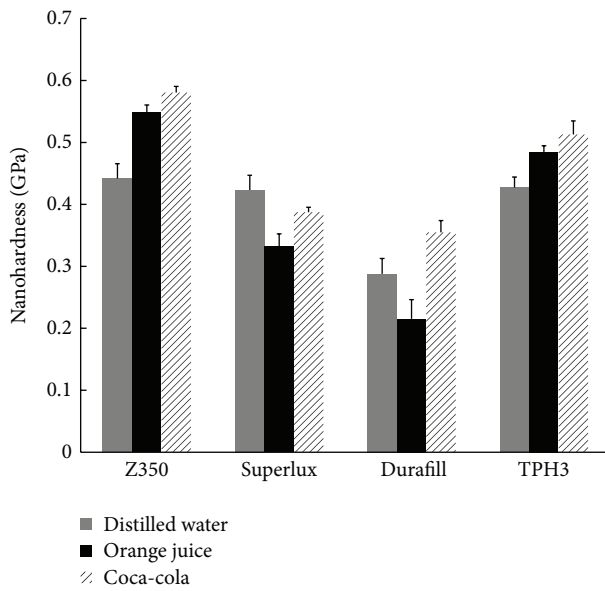


FIGURE 2: Mean values and standard deviations (vertical bar) for nanohardness of four composites tested under different storage media.

orange juice was higher than with distilled water but lower than with cola immersion. For the two resin composites, the modulus with orange juice immersion was significantly higher than that with the cola treatment ($P < 0.05$).

Conditioning of the Superlux with TEGDMA, Bis-GMA, and urethane dimethacrylate (UDMA) resulted in greater nanohardness deterioration in orange juice or cola than in water. The Z350 and TPH³ composites are BisGMA-based. The nanohardness deterioration in distilled water was significantly greater than in acid solution. In acid, an increase in the nanohardness was observed. The resin matrix of composites is known to absorb a small amount of water, which alters certain physical properties. For example, the surface hardness has been reported to be affected by water sorption and the resin matrices of Z350 and TPH³ are more susceptible to the softening effects of water.

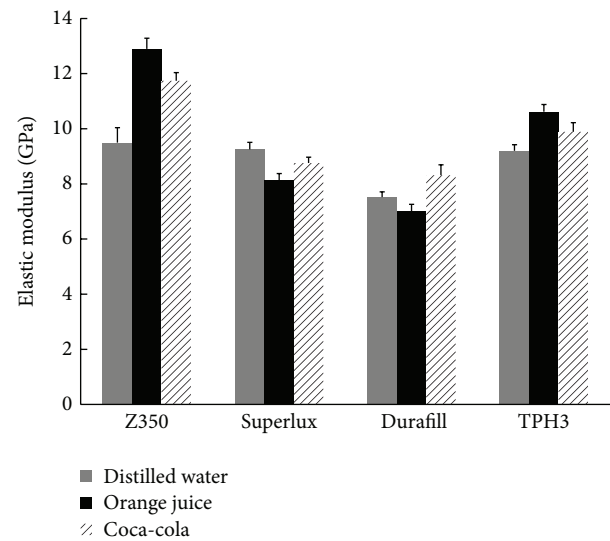


FIGURE 3: Mean values and standard deviations (vertical bar) for elastic modulus of four composites tested under different storage media.

In addition to the effect of the matrix, the particulate filler also plays an important role in determining mechanical properties.

An increase in the filler content is expected to increase the hardness to some extent. The filler content of any two materials is similar, although the distribution of the particles in nanohybrid resins is less homogeneous. Additionally, the range of fillers for nanohybrid resins is larger than for nanofillers. However, a less homogeneous distribution of filler and matrix is less susceptible to acid attack. An increased nanoparticle content might increase the hardness to some extent [16, 17]. The filler contents are shown in Table 1. The percentages of filler in the microfilled and universal hybrid composites are lower than those of the other tested materials. Thus, our results are in agreement with these previous findings.

The ingredients of acids also influence the surface nanohardness of specimens [18–20]. Orange juice contains citric acid, whereas Coca-Cola contains phosphoric acid [21].

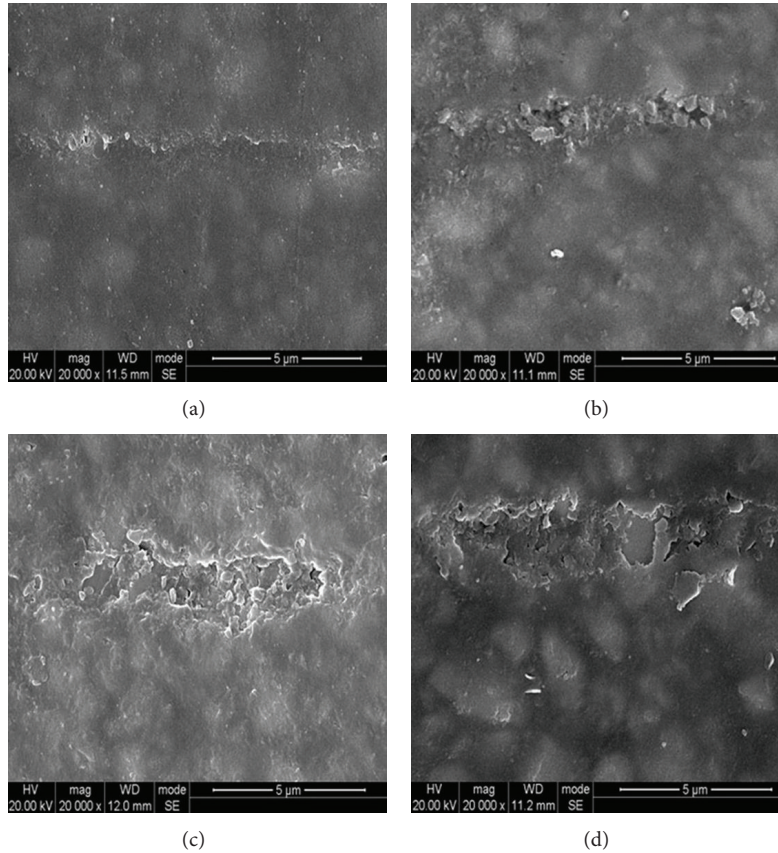


FIGURE 4: Representative SEM micrographs of the nanoscratch mark morphology of resin-based composites after immersion in Orange juice. (a) Z350, (b) Superlux, (c) Durafill, and (d) TPH³.

Citric acid is a carboxylic acid that is capable of chelating ions such as calcium to form complexes with a moderate solubility in water. Phosphoric acid is capable of chelating calcium but forms an essentially insoluble complex [22]. Phosphate ions could slow the dissolution of calcium phosphate; that is, the organic acids were found to induce softening of bis-GMA polymers [8, 23] and the softening was strongly affected by the acidity. Specific carboxylic acids are responsible for the damage caused by orange juice, and a low pH is not the sole factor, since an acidic solution should decrease the rate of such hydrolysis [24].

SEM analysis showed that all composite resins experienced surface changes after the nanoscratch test. The changes could be considered to be part of a process of degradation and erosion of the matrix. The surface features of the specimens aged in orange juice were more affected than those of the specimens aged in distilled water or cola. Several protruding particles, voids, and cracks were observed in all of the analyzed specimens. These findings are consistent with those of a previous study [25]. As shown in Figures 4(b), 5(b), and 6(b), the morphology of Superlux between each other are quite different. The composites also displayed a poor bond at the interfacial region between the matrix and the reinforcement particles. Superlux presented some gaps in the interface where particles and fibers contact the matrix. More

obviously, pieces of the mixture, components, and matrix were disrupted and moved from the basement of the matrix under the scratch mark under the orange juice and cola treatments (Figure 5(b)). The fractures between the matrix and fillers were still present, but the desquamation of the mixture components has been slightly reduced. There were many visible porous cracks in or on the surface of the specimens (Figure 4(b)).

In terms of the nanoscratch mark morphology, Durafill presented a uniform thin tribolayer, and there were some cracking and segmentation of the fillers. There was also consistent wear of the matrix and particles. However, there were also some fragments distributed around the scratch. Figures 5(c), 6(c) illustrates the poor wear resistance in samples treated with orange juice or cola. There were few particles that broke or were removed from the matrix. The layer detached from the matrix and some particles remained in the scratch on the specimen surface (Figure 5(c)).

The acid-treated Z350 samples that only showed a small amount of debris had a tribolayer with a smaller portion of contact on the resin composite surface.

TPH³ presented a tribolayer, although the layer was broken by detached particles and fibers from the matrix that remained in contact with the specimen surface after

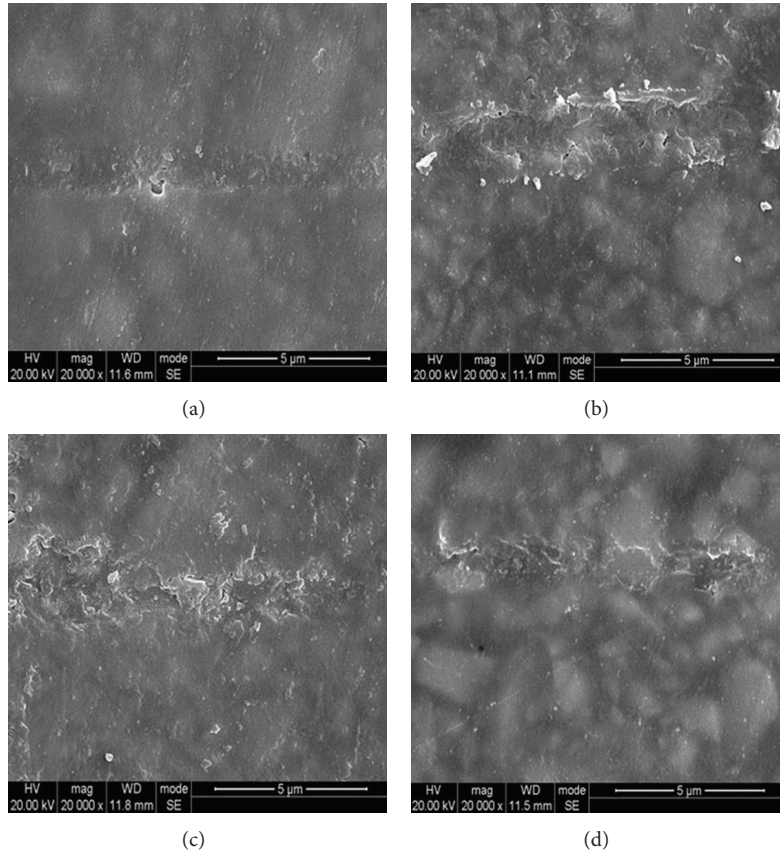


FIGURE 5: Representative SEM micrographs of the nanoscratch mark morphology of resin-based composites after immersion in Coca-Cola. (a) Z350, (b) Superlux, (c) Durafill, and (d) TPH³.

immersion in orange juice (Figure 5(d)). Similar results were observed with cola (Figure 6(d)).

According to previously published results and our experimental observations, the wear behavior of both composites could be attributed to the delamination/pull-out or cracking/fracture mechanisms. Delamination is generally defined as the desquamation of reinforcement particles in the form of sheets or flakes caused by subsurface crack propagation along the sliding direction [26]. Such cracks occur in deformed areas, thus, it is probable that plastic flow occurred in the resin matrix after filler displacement during the wear process.

Generally, TPH³ and Z350 experience less degradation than Superlux and Durafill. This may be attributed to the lower polymer matrix content in the composites. Because TPH³ and Z350 have less polymer matrix than Superlux and Durafill, the nanofiller composites showed a lower reduction in nanohardness after immersion in acidic drinks compared to a universal hybrid and microfilled composite. This difference can be attributed to the lower organic matrix content of Superlux relative to TPH³. For example, the microfilled composite showed a greater reduction in hardness when compared to a universal hybrid composite. The reasoning presented in a previous study that the nanosize of the hard phase in biological materials will enhance the interface strength that might be used to explain this result [4, 27].

It is suggested that as the diamond tip slides on the composite surface, differences in the stress concentration between the filler and matrix interfaces may exist due to differences in the size of fillers. This implies that the stress and degradation associated with larger filler particles were greater than those with smaller particles which is consistent with the present study [28].

As shown in Table 3, the One-way ANOVA analysis and LSD *t*-test indicated a significant difference for the tested immersion media and resin composites. The nanoscratch depths for all materials indicate that a higher inorganic content corresponded to a lower the scratch depth. The depth of nanoscratch of among composites followed by the decreasing order Durafill > Superlux > TPH³ > Z350. The orange juice significantly increased the depth of nanoscratch more than the distilled water and cola. There was also significant difference in depth changes between distilled water, orange juice, and cola in all specimens under the same test condition. ($P < 0.05$). As can be observed, increase in inorganic content can decrease scratch depth, in scratching process compact and hard inorganic network can resist penetration of indenter and in this manner restricts deformation of the surface.

It is generally understood that highly filled composites are more resistant to degradation [29, 30] because of the limited spaces and pathways available for acid molecules to

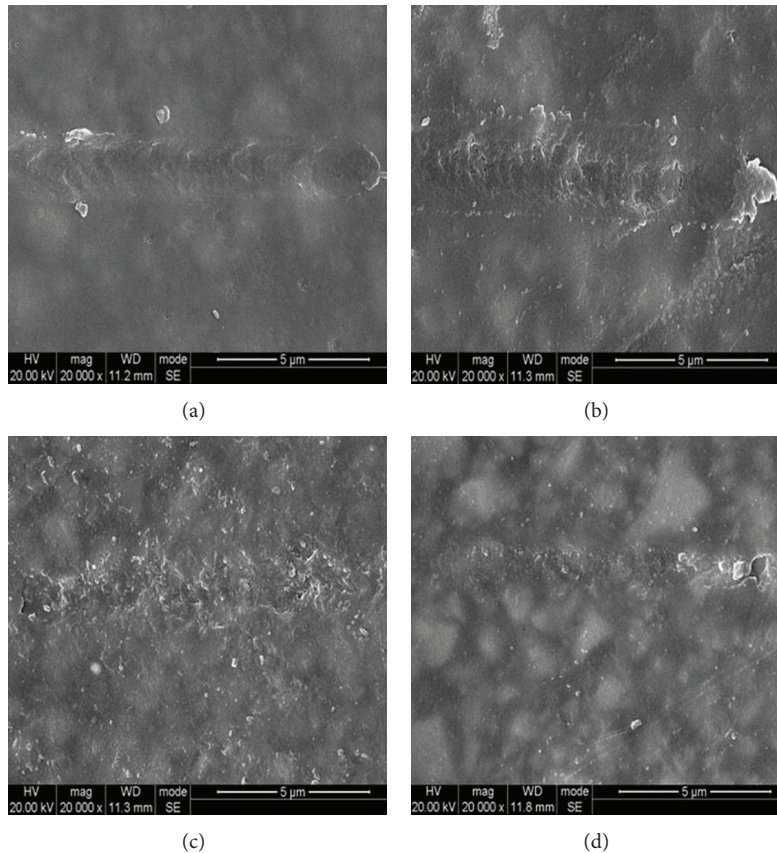


FIGURE 6: Representative SEM micrographs of the nanoscratch mark morphology of resin-based composites after immersion in distilled water. (a) Z350, (b) Superlux, (c) Durafill, and (d) TPH³.

TABLE 3: Mean and standard deviation (S.D.) of depth parameters from nanoscratch test (nm).

Sample	Distilled water 1 cycle	Orange juice 1 cycle	Cola 1 cycle
Z350	91.47 (0.23) ^{aA}	95.83 (0.45) ^{bB}	93.45 (0.47) ^{dC}
TPH ³	101.44 (1.23) ^{bA}	105.41 (1.31) ^{cB}	102.82 (0.92) ^{aC}
Superlux	111.30 (1.64) ^{cA}	119.14 (1.43) ^{dB}	115.10 (2.24) ^{bC}
Durafill	122.27 (2.12) ^{dA}	130.94 (2.45) ^{aB}	127.31 (1.99) ^{cC}

Different uppercase letters in the same line indicate differences for storage media; different lowercase letters in the same column indicate differences for materials ($P < 0.05$).

diffuse within the polymer network. Thus, when a composite is subjected to scratching, the compact and hard inorganic network can resist the penetration of the indenter, which limits the deformation.

In this study, it has been confirmed that all of the tested factors can affect the resin performance. The behavior of each material was influenced by its components but was not entirely determined by one or more factors. Manufacturers should consider these factors when producing materials with a homogeneous body.

4. Conclusions

We can draw the following conclusions from this study. Modern dental restorative materials have been shown to

behave differently when stored in different types of media. The microfilled and universal hybrid resin composites were significantly affected by exposure to cola and orange juice. The nanofilled resin composites showed greater wear resistance. In addition, other factors were found to play an important role in determining the resin surface stability characteristics, such as the filler loading, filler type, and the proportion of filler/matrix.

Currently, the filler particles of resin composites can be classified according to size as microfilled hybrid, nanohybrid, and nanofilled. Hybrids have different incorporation particles sizes (15–20 μm and 0.01–0.05 μm) and fillers offer excellent mechanical properties. Microfill composites have excellent aesthetic effects and include colloidal silica and particles (0.01–0.05 μm). As the dental market improves,

nanocomposites are increasingly used in clinical settings. These materials combine the good mechanical strength of the hybrids [31] with the aesthetic performance, surface smoothness, and superior polish of the microfills [32]. Several types of nanocomposites are available, including nanohybrids, which can contain glass fillers and nanoparticles, as well as nanofills, which contain many different sizes of nanofill particles [33].

Conflict of Interests

The authors declare that there is no conflict of interests regarding the publication of this paper.

Acknowledgments

The authors acknowledge the support of the National Natural Science Foundation of China (nos. 81170996, 81070867, and 81100777), Sichuan Province Science and Technology Innovation Team Program (2011JTD0006), and declare any industrial links or affiliations.

References

- [1] P. Senawongse and P. Pongprueksa, "Surface roughness of nanofill and nanohybrid resin composites after polishing and brushing," *Journal of Esthetic and Restorative Dentistry*, vol. 19, no. 5, pp. 265–273, 2007.
- [2] H. Oysaed and I. E. Ruyter, "Composites for use in posterior teeth: mechanical properties tested under dry and wet conditions," *Journal of Biomedical Materials Research*, vol. 20, no. 2, pp. 261–271, 1986.
- [3] J. G. Calais and K. J. Soderholm, "Influence of filler type and water exposure on flexural strength of experimental composite resins," *Journal of Dental Research*, vol. 67, no. 5, pp. 836–840, 1988.
- [4] S. Wongkhantee, V. Patanapiradej, C. Maneenut, and D. Tantbirojn, "Effect of acidic food and drinks on surface hardness of enamel, dentine, and tooth-coloured filling materials," *Journal of Dentistry*, vol. 34, no. 3, pp. 214–220, 2006.
- [5] L. Gonçalves, J. D. N. Filho, J. G. A. Guimarães, L. T. Poskus, and E. M. da Silva, "Solubility, salivary sorption and degree of conversion of dimethacrylate-based polymeric matrixes," *Journal of Biomedical Materials Research B: Applied Biomaterials*, vol. 85, no. 2, pp. 320–325, 2008.
- [6] S. Kalachandra and T. W. Wilson, "Water sorption and mechanical properties of light-cured proprietary composite tooth restorative materials," *Biomaterials*, vol. 13, no. 2, pp. 105–109, 1992.
- [7] A. R. Curtis, A. C. Shortall, P. M. Marquis, and W. M. Palin, "Water uptake and strength characteristics of a nanofilled resin-based composite," *Journal of Dentistry*, vol. 36, no. 3, pp. 186–193, 2008.
- [8] R. G. Chadwick, J. F. McCabe, A. W. G. Walls, and R. Storer, "The effect of storage media upon the surface microhardness and abrasion resistance of three composites," *Dental Materials*, vol. 6, no. 2, pp. 123–128, 1990.
- [9] S. El-Safty, R. Akhtar, N. Silikas, and D. C. Watts, "Nanomechanical properties of dental resin-composites," *Dental Materials*, vol. 28, no. 12, pp. 1292–1300, 2012.
- [10] J. Cayer-Barrioz, D. Mazuyer, A. Tonck, P. Kapsa, and A. Chateauminois, "Nanoscratch and friction: an innovative approach to understand the tribological behaviour of poly(amide) fibres," *Tribology International*, vol. 39, no. 2, pp. 62–69, 2006.
- [11] F. Gao, S. Matsuya, M. Ohta, and J. Zhang, "Erosion process of light-cured and conventional glass ionomer cements in citrate buffer solution," *Dental Materials Journal*, vol. 16, no. 2, pp. 170–179, 1997.
- [12] J. W. Nicholson, B. J. Millar, B. Czarnecka, and H. Limanowska-Shaw, "Storage of polyacid-modified resin composites ("compomers") in lactic acid solution," *Dental Materials*, vol. 15, no. 6, pp. 413–416, 1999.
- [13] A. Lussi and T. Jaeggi, "Dental erosion in children," *Monographs in Oral Science*, vol. 20, pp. 140–151, 2006.
- [14] P. Lambrechts, M. Braem, and G. Vanherle, "Buonocore memorial lecture: evaluation of clinical performance for posterior composite resins and dentin adhesives," *Operative Dentistry*, vol. 12, no. 2, pp. 53–78, 1987.
- [15] A. U. J. Yap, X. Wang, X. Wu, and S. M. Chung, "Comparative hardness and modulus of tooth-colored restoratives: a depth-sensing microindentation study," *Biomaterials*, vol. 25, no. 11, pp. 2179–2185, 2004.
- [16] M. S. Sadjadi and N. Farhadyar, "Preparation and characterization of the hydrophilic nanocomposite coating based on epoxy resin and titanate on the glass substrate," *Journal of Nanoscience and Nanotechnology*, vol. 9, no. 2, pp. 1172–1175, 2009.
- [17] U. Erdemir, E. Yildiz, and M. M. Eren, "Effects of sports drinks on color stability of nanofilled and microhybrid composites after long-term immersion," *Journal of Dentistry*, vol. 40, supplement 2, pp. e55–e63, 2012.
- [18] W. Wu, E. E. Toth, J. F. Moffa, and J. A. Ellison, "Subsurface damage layer of in vivo worn dental composite restorations," *Journal of Dental Research*, vol. 63, no. 5, pp. 675–680, 1984.
- [19] K. F. Leinfelder, A. D. Wilder Jr., and L. C. Teixeira, "Wear rates of posterior composite resins," *The Journal of the American Dental Association*, vol. 112, no. 6, pp. 829–833, 1986.
- [20] J. M. Powers and P. L. Fan, "Erosion of composite resins," *Journal of Dental Research*, vol. 59, no. 5, pp. 815–819, 1980.
- [21] G. van der Horst, I. Wesso, A. P. Burger, D. L. Dietrich, and S. R. Grobler, "Chemical analysis of cooldrinks and pure fruit juices—some clinical implications," *The South African Medical Journal*, vol. 66, no. 20, pp. 755–758, 1984.
- [22] I. Khairoun, M. G. Boltong, F. C. M. Driessens, and J. A. Planell, "Some factors controlling the injectability of calcium phosphate bone cements," *Journal of Materials Science: Materials in Medicine*, vol. 9, no. 8, pp. 425–428, 1998.
- [23] E. Asmussen, "Softening of BISGMA-based polymers by ethanol and by organic acids of plaque," *Scandinavian Journal of Dental Research*, vol. 92, no. 3, pp. 257–261, 1984.
- [24] U. Örtengren, F. Andersson, U. Elgh, B. Terselius, and S. Karlsson, "Influence of pH and storage time on the sorption and solubility behaviour of three composite resin materials," *Journal of Dentistry*, vol. 29, no. 1, pp. 35–41, 2001.
- [25] W. M. Palin, G. J. P. Fleming, F. J. T. Burke et al., "The frictional coefficients and associated wear resistance of novel low-shrink resin-based composites," *Dental Materials*, vol. 21, no. 12, pp. 1111–1118, 2005.
- [26] A. Onat, "Mechanical and dry sliding wear properties of silicon carbide particulate reinforced aluminium-copper alloy matrix composites produced by direct squeeze casting method,"

Journal of Alloys and Compounds, vol. 489, no. 1, pp. 119–124, 2010.

- [27] B. Ji, “A study of the interface strength between protein and mineral in biological materials,” *Journal of Biomechanics*, vol. 41, no. 2, pp. 259–266, 2008.
- [28] H. Gao, B. Ji, I. L. Jäger, E. Arzt, and P. Fratzl, “Materials become insensitive to flaws at nanoscale: lessons from nature,” *Proceedings of the National Academy of Sciences of the United States of America*, vol. 100, no. 10, pp. 5597–5600, 2003.
- [29] B. Ji and H. Gao, “Mechanical properties of nanostructure of biological materials,” *Journal of the Mechanics and Physics of Solids*, vol. 52, no. 9, pp. 1963–1990, 2004.
- [30] H. Gao and B. Ji, “Modeling fracture in nanomaterials via a virtual internal bond method,” *Engineering Fracture Mechanics*, vol. 70, no. 14, pp. 1777–1791, 2003.
- [31] N. Moszner and S. Klapdohr, “Nanotechnology for dental composites,” *International Journal of Nanotechnology*, vol. 1, no. 1-2, pp. 130–156, 2004.
- [32] C. P. Turssi, J. R. Saad, S. L. Duarte Jr., and A. L. Rodrigues Jr., “Composite surfaces after finishing and polishing techniques,” *American Journal of Dentistry*, vol. 13, no. 3, pp. 136–138, 2000.
- [33] S. B. Mitra, D. Wu, and B. N. Holmes, “An application of nanotechnology in advanced dental materials,” *Journal of the American Dental Association*, vol. 134, no. 10, pp. 1382–1390, 2003.

Research Article

Interaction Potential between Parabolic Rotator and an Outside Particle

Dan Wang, Yajun Yin, Jiye Wu, Xugui Wang, and Zheng Zhong

Department of Engineering Mechanics, School of Aerospace, Tsinghua University, Beijing 100084, China

Correspondence should be addressed to Yajun Yin; yinyj@mail.tsinghua.edu.cn

Received 29 April 2014; Accepted 19 June 2014; Published 7 July 2014

Academic Editor: Shaoyun Fu

Copyright © 2014 Dan Wang et al. This is an open access article distributed under the Creative Commons Attribution License, which permits unrestricted use, distribution, and reproduction in any medium, provided the original work is properly cited.

At micro/nanoscale, the interaction potential between parabolic rotator and a particle located outside the rotator is studied on the basis of the negative exponential pair potential $(1/R)^n$ between particles. Similar to two-dimensional curved surfaces, we confirm that the potential of the three-dimensional parabolic rotator and outside particle can also be expressed as a unified form of curvatures; that is, it can be written as the function of curvatures. Furthermore, we verify that the driving forces acting on the particle may be induced by the highly curved micro/nano-parabolic rotator. Curvatures and the gradient of curvatures are the essential elements forming the driving forces. Through the idealized numerical experiments, the accuracy of the curvature-based potential is preliminarily proved.

1. Introduction

In recent years, various phenomena at micro/nanoscales increasingly draw people's attention. The highly curved spaces widely exist at micro/nanoscales. As a typical form, curved surfaces are objects studied in differential geometry. In addition, there is another space form, that is, the curved surface body. A curved surface body is a three-dimensional body. In this sense, it is outside the range of curved spaces. Nevertheless, when the size scale we study is small enough, the large specific surface area and the highly curved outer surface will powerfully connect curved surface body with curved space.

Similar to curved surfaces, curved surface bodies widely exist at micro/nanoscales. In biological system, organic particles may be transported between cells by the tubular conduits of tunneling nanotubes [1] (Figure 1). Human fibroblasts extend by sensing the fiber curvatures [2]. Inward curvatures of the plasma membrane may cause BAR-domain proteins to release Rac [2, 3]. Silicone oil droplets on conical surfaces will move spontaneously towards the end with bigger diameter [4]. Through the interaction between the tip (Figure 2) and the tested object [5], atomic force microscope can probe the morphologies of surfaces [6]. All these cases involve the interaction of the curved surface bodies.

Previously, based on the pair-potential of particles $((1/R)^n)$, Yin et al. [7] studied the interaction between micro/nano-curved surface and a particle located outside the surface. Wu et al. [8, 9] explored the interaction between micro/nano-curved surface and a particle located inside the surface. Their researches verify that interaction between highly curved surface and particle can be expressed as the function of curvatures. Then they give the following propositions. (a) At micro/nanoscale, the highly curved surface can induce driving forces. (b) The essential elements that form the driving forces are curvatures and the gradient of curvatures.

Previous studies inspire us to raise questions. Will the interaction potential between curved surface body and particle be expressed as the function of curvatures? Whether the curved surface of the curved surface body can induce the driving forces as well? This paper will give the answers.

2. Interaction between Semi-Infinite Plane Body and a Particle Located outside the Plane

As a prelude, we review the interaction between semi-infinite plane body and a particle located outside the plane, which has already existed in the flat space.

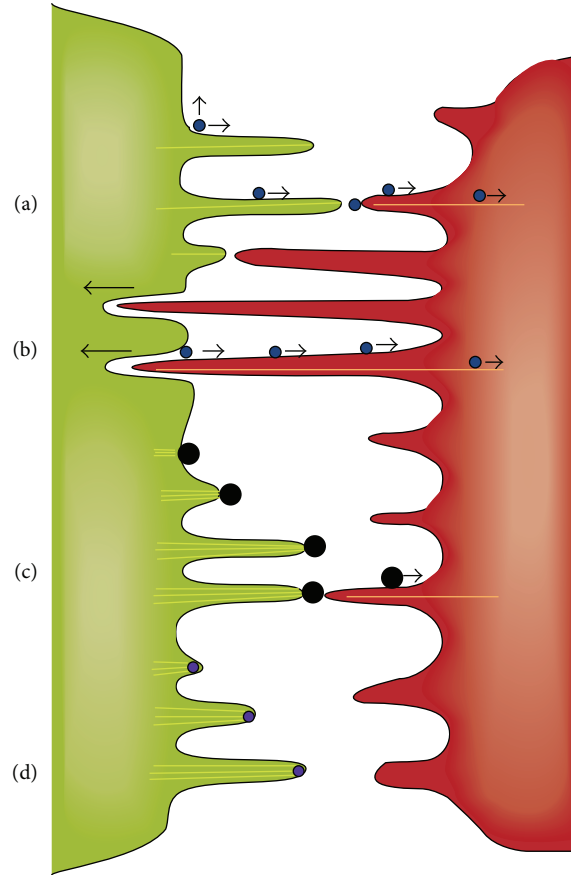


FIGURE 1: The transportation of organic particles between cells by tunneling nanotubes [1].

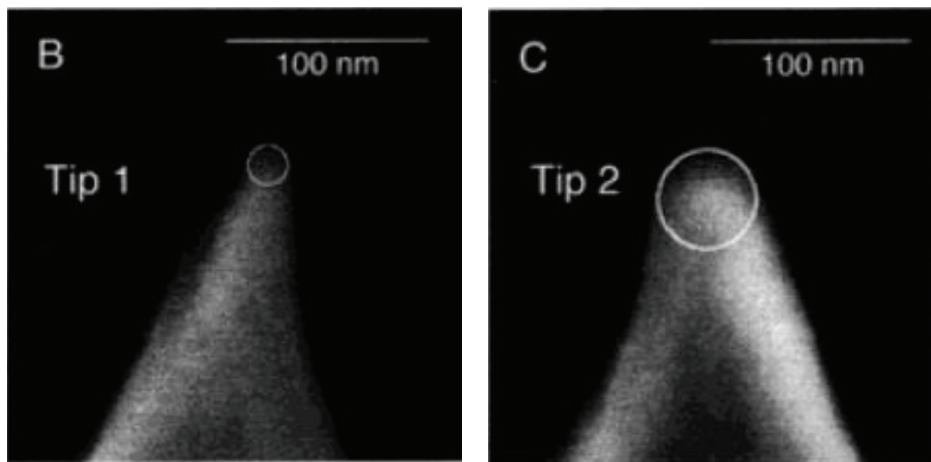


FIGURE 2: Atomic force microscopes with sharp probe (B) and blunt probe (C) [5].

Semi-infinite plane body belongs to the three-dimensional Euclid space. Thus, the interaction between it and an outside particle is a classical mechanical problem. The potential can be found in the book written by Israelachvili [10]. As shown in Figure 3, if we assume that the pair-potential between particles has the form of $u(r) = C/r^n$, the number density of molecules in semi-infinite plane body

is ρ , and the nearest distance between the particle and the plane is h , then the interaction potential of the particle p and semi-infinite body can be written as

$$\bar{U}_n = \frac{2\pi\rho C}{(n-2)(n-3)h^{n-3}}, \quad n \geq 4. \quad (1)$$

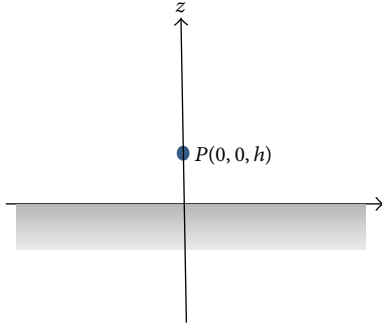


FIGURE 3: The interaction between semi-infinite plane body and an outside particle.

If the surface of the plane body shown in Figure 3 bends, it will become a curved surface body. Hence, semi-infinite plane body is not only a particular case of the curved surface body, but also the foundation for further studies.

3. Classification of Parabolic Rotators

Previously, researchers have studied the interaction between certain curved surface body and a particle, like a sphere and a cylinder [11, 12]. As a preliminary test, this paper will study another simple case, that is, the interaction between a parabolic rotator and a particle located outside the rotator.

According to the bending direction, parabolic rotators can be divided into two categories, that is, convex parabolic rotator and concave parabolic rotator (Figure 4). Obviously, these two kinds of parabolic rotators are different when they interact with an outside particle. From this perspective, these two cases should be studied separately.

Whatever it is convex or concave, the biggest commonality of two kinds of parabolic rotators is that they have similar curved surfaces, that is, the revolutionary paraboloid. In this sense, it is possible to study two kinds of parabolic rotators uniformly. A unified coordinate system is used to ensure the uniformity.

As shown in Figures 5 and 6, a local Cartesian coordinate system $O-xyz$ is built at the vertex O of the parabolic rotator. The $x-y$ plane is the tangent plane of the parabolic rotator at the vertex O . The function of the revolutionary paraboloid for the convex and concave rotators can be uniformly expressed as $z = (c/2)(x^2 + y^2)$ in such coordinate system. By the differential geometry [13], the principal curvatures at the vertex O of the revolutionary paraboloid are $c_1 = c_2 = c$ with $c > 0$ in the illustrated coordinate system.

Assuming that the outside particle p is located on the axis z and has a distance h to the vertex O , the coordinate of the particle p is $(0, 0, -h)$ for convex parabolic rotator and $(0, 0, h)$ for concave parabolic rotator. To ensure uniformity, we write the coordinate of the particle p as $(0, 0, z_p)$. Therefore, $z_p = -h$ corresponds to convex parabolic rotator and $z_p = h$ corresponds to concave parabolic rotator. Define the dimensionless coordinates as

$$\tilde{z}_p = \frac{z_p}{h}. \quad (2)$$

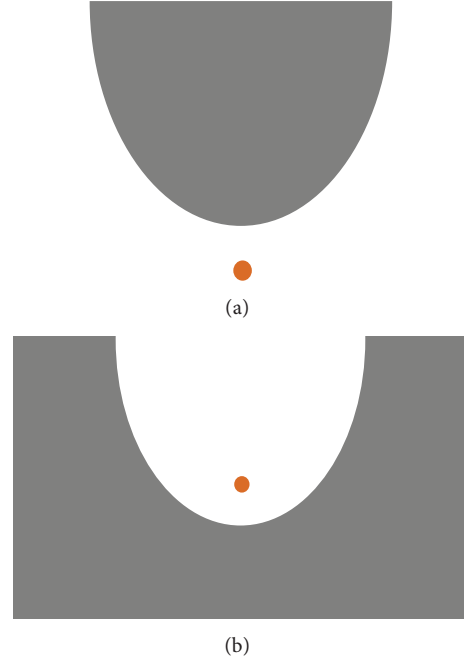


FIGURE 4: (a) Convex parabolic rotator and an outer particle; (b) concave parabolic rotator and an outer particle.

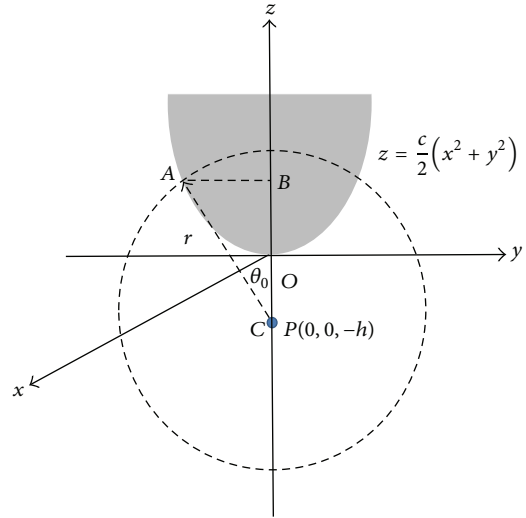


FIGURE 5: The coordinate system of convex parabolic rotator and an outside particle.

Obviously, there are only two values for \tilde{z}_p . $\tilde{z}_p = -1$ corresponds to convex parabolic rotator, and $\tilde{z}_p = +1$ corresponds to concave parabolic rotator.

4. Interaction Potential between Parabolic Rotator and a Particle

4.1. *The General Formulation of the Potential.* In order to derive the interaction potential between the particle p and the parabolic rotator, we draw a sphere with the center at particle

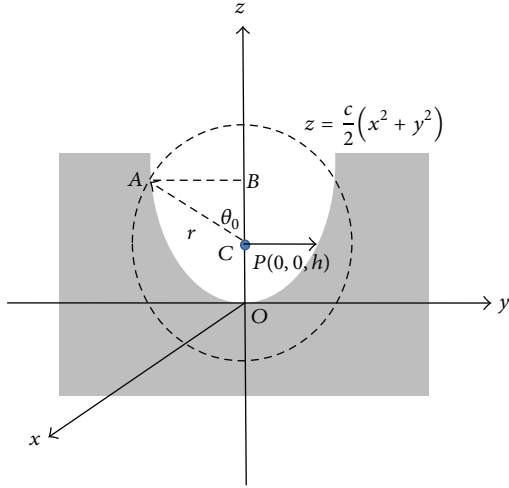


FIGURE 6: The coordinate system of concave parabolic rotator and an outside particle.

p and the radius r . The intersection part of spherical surface and parabolic rotator is an arc surface with the area S . Then the potential between the particle and parabolic rotator is

$$U_n = \int_h^\infty \frac{C\rho_v S}{r^n} dr. \quad (3)$$

Equation (3) is valid for both convex parabolic rotator and concave parabolic rotator.

4.2. The Uniform Formulation of the Area of the Arc Surface. The area S in (3) can be determined as follows. For convex parabolic rotator (Figure 5), we have

$$\widehat{S} = \int_0^{2\pi} d\varphi \int_0^{\theta_0} r^2 \sin \theta d\theta = 2\pi r^2 (1 - \cos \theta_0). \quad (4)$$

The spherical center angle θ_0 satisfies

$$\cos \theta_0 = \frac{z + h}{r}. \quad (5)$$

In triangle ABC, we have

$$x^2 + y^2 + (z + h)^2 = r^2. \quad (6)$$

By combining $z = (c/2)(x^2 + y^2)$ with (5) and (6), we get

$$\cos \theta_0 = \frac{\sqrt{(2h/c) + (1/c^2) + r^2} - (1/c)}{r}. \quad (7)$$

Substitution of (7) into (4) leads to

$$\widehat{S} = 2\pi r \left[r + \frac{1}{c} - \frac{1}{c} \sqrt{1 + 2hc + (cr)^2} \right]. \quad (8)$$

For concave parabolic rotator (Figure 6), there is

$$\check{S} = 4\pi r^2 - \int_0^{2\pi} d\varphi \int_0^{\theta_0} r^2 \sin \theta d\theta = 2\pi r^2 (1 + \cos \theta_0), \quad (9)$$

$$\cos \theta_0 = \frac{z - h}{r}. \quad (10)$$

In triangle ABC, there is

$$x^2 + y^2 + (z - h)^2 = r^2. \quad (11)$$

By combining $z = (c/2)(x^2 + y^2)$ with (10) and (11), we get

$$\cos \theta_0 = \frac{\sqrt{-(2h/c) + (1/c^2) + r^2} - (1/c)}{r}. \quad (12)$$

Substitution of (12) into (9) gives

$$\check{S} = 2\pi r \left[r - \frac{1}{c} + \frac{1}{c} \sqrt{1 - 2hc + (cr)^2} \right]. \quad (13)$$

Obviously, with the dimensionless coordinate \tilde{z}_p , (8) and (13) can be uniformly written as

$$S = 2\pi r \left[r - \frac{1}{\tilde{z}_p c} + \frac{1}{\tilde{z}_p c} \sqrt{1 - 2h\tilde{z}_p c + (\tilde{z}_p cr)^2} \right]. \quad (14)$$

4.3. Curvature-Based Interaction Potential between Particle and Parabolic Rotator. By substituting (14) into (3), we obtain the interaction potential between the particle p and convex and concave parabolic rotators uniformly:

$$\begin{aligned} U_n &= 2\pi\rho_v C \\ &\times \int_h^\infty \frac{1}{r^{n-1}} \\ &\times \left[r - \frac{1}{\tilde{z}_p c} + \frac{1}{\tilde{z}_p c} \sqrt{1 - 2h\tilde{z}_p c + (\tilde{z}_p cr)^2} \right] dr. \end{aligned} \quad (15)$$

The objective of this section is to express (15) as an explicit function of curvature. The technique is mature, that is, the series expansion for small parametric variable [14]. The distance h is used as the characteristic length in dimensionless transformations:

$$\tilde{c} = ch, \quad \tilde{r} = \frac{r}{h}. \quad (16)$$

Then (15) can be written as

$$\begin{aligned} U_n &= \frac{2\pi\rho_v C}{h^{n-3}} \\ &\times \int_1^\infty \frac{1}{\tilde{r}^{n-1}} \\ &\times \left[\tilde{r} - \frac{1}{\tilde{z}_p \tilde{c}} + \frac{1}{\tilde{z}_p \tilde{c}} \sqrt{1 - 2\tilde{z}_p \tilde{c} + (\tilde{z}_p \tilde{c} \tilde{r})^2} \right] d\tilde{r}. \end{aligned} \quad (17)$$

In (17), let

$$f(\tilde{c}) = \sqrt{1 - 2\tilde{c} + (\tilde{c}\tilde{r})^2}. \quad (18)$$

Here $\tilde{c} = \tilde{z}_p \tilde{c}$ and $f(\tilde{c})$ is the continuously differentiable function of \tilde{c} . Suppose that the distance h is a small quantity

TABLE 1: The error of curvature-based potential between the convex parabolic rotator and the particle ($n = 6$).

\tilde{c}	$(\tilde{U}_6)_{\text{numerical}}$	$(\tilde{U}_6)_{\text{polynomial}}$	$\delta = \frac{(\tilde{U}_6)_{\text{polynomial}} - (\tilde{U}_6)_{\text{numerical}}}{(\tilde{U}_6)_{\text{numerical}}}$
0.5	0.554354020074120	0.625000000000000	0.127438382996544
0.4	0.609849704658992	0.640000000000000	0.049438894715652
0.3	0.677316303948916	0.685000000000000	0.011344324662327
0.1	0.866023611886837	0.865000000000000	0.001181967642437
0.05	0.929014971306476	0.928750000000000	2.852174772848038e - 004
0.03	0.956428713838380	0.956350000000000	8.229974407998883e - 005
0.01	0.985151878051310	0.985150000000000	1.906357133214219e - 006
0.005	0.992534562174735	0.992537500000000	2.959922381342625e - 006
0.001	0.998496854809661	0.998501500000000	4.652183245473563e - 006
0.0001	0.999845094980028	0.999850015000000	4.920782226301011e - 006

compared to the curvature radius at the vertex of parabolic rotator. Therefore, the dimensionless curvatures satisfy $\tilde{c} \ll 1$ and $|\tilde{c}| \ll 1$. Take \tilde{c} as the small parametric variable and use the method of series expansion [14]. Function $f(\tilde{c})$ can be expanded as Taylor's series of small parametric variable \tilde{c} :

$$f(\tilde{c}) \approx f(0) + \left(\frac{\partial f}{\partial \tilde{c}} \Big|_{\tilde{c}=0} \right) \tilde{c} + \frac{1}{2!} \left(\frac{\partial^2 f}{\partial \tilde{c}^2} \Big|_{\tilde{c}=0} \right) \tilde{c}^2 + \frac{1}{3!} \left(\frac{\partial^3 f}{\partial \tilde{c}^3} \Big|_{\tilde{c}=0} \right) \tilde{c}^3 + \frac{1}{4!} \left(\frac{\partial^4 f}{\partial \tilde{c}^4} \Big|_{\tilde{c}=0} \right) \tilde{c}^4 + \dots \quad (19)$$

$$+ \frac{1}{m!} \left(\frac{\partial^m f}{\partial \tilde{c}^m} \Big|_{\tilde{c}=0} \right) \tilde{c}^m + O(\tilde{c}^m).$$

We omit the terms whose orders are higher than 3 to get the polynomial of variable \tilde{c} :

$$f(\tilde{c}) \approx f(0) + f'(0)\tilde{c} + \frac{f''(0)}{2!}\tilde{c}^2 + \frac{f'''(0)}{3!}\tilde{c}^3 + O(\tilde{c}^3)$$

$$= 1 - \tilde{c} + \frac{1}{2}(\tilde{r}^2 - 1)\tilde{c}^2 + \frac{1}{2}(\tilde{r}^2 - 1)\tilde{c}^3. \quad (20)$$

Substitution of (20) into (17) leads to the uniform polynomial of curvature-based potential:

$$U_n = \bar{U}_n \left[1 + \frac{n-3}{n-4} \tilde{z}_p \tilde{c} + \frac{n-3}{n-4} (\tilde{z}_p \tilde{c})^2 \right]. \quad (21)$$

Equation (21) requires $n \geq 5$. The value of index n is determined by the expanding order of \tilde{c} in (19). If the series is expanded to \tilde{c}^3 , then $n \geq 4$ is needed.

Although parabolic rotator is three-dimensional body, (21) indicates that the interaction potential between the rotator and the particle is still decided by the curvature c . If $c \rightarrow 0$, we have $U_n \rightarrow \bar{U}_n$; that is, the interaction potential U_n will degenerate to \bar{U}_n . Once the flat surface is curved, the interaction potential is no longer \bar{U}_n , and a modified term of curvatures must be involved. The more curved the space is, the more significant the influence of modified term of curvatures is.

5. Numerical Verification

What is the accuracy of the curvature-based potential of polynomial? The answer will be provided through numerical verification.

First, both sides of curvature-based potential of polynomial (21) are divided by \bar{U}_n to get the dimensionless form:

$$(\bar{U}_n)_{\text{polynomial}} = \frac{U_n}{\bar{U}_n} = 1 + \frac{n-3}{n-4} \tilde{z}_p \tilde{c} + \frac{n-3}{n-4} (\tilde{z}_p \tilde{c})^2. \quad (22)$$

Then both sides of (17) are divided by \bar{U}_n to get the dimensionless potential of integral form:

$$(\bar{U}_n)_{\text{numerical}} = (n-2)(n-3) \times \int_1^\infty \frac{1}{\tilde{r}^{n-1}} \times \left[\tilde{r} - \frac{1}{\tilde{z}_p \tilde{c}} + \frac{1}{\tilde{z}_p \tilde{c}} \sqrt{1 - 2\tilde{z}_p \tilde{c} + (\tilde{z}_p \tilde{c})^2} \right] d\tilde{r}. \quad (23)$$

Finally, $(\bar{U}_n)_{\text{numerical}}$ in (23) and $(\bar{U}_n)_{\text{polynomial}}$ in (22) are compared, and the accuracy of (22) may be estimated:

$$\delta = \left| \frac{(\bar{U}_n)_{\text{polynomial}} - (\bar{U}_n)_{\text{numerical}}}{(\bar{U}_n)_{\text{numerical}}} \right| \times 100\%. \quad (24)$$

In the numerical calculations, we will take $n = 6$. The errors of curvature-based potential of convex and concave parabolic rotators are listed in Tables 1 and 2, respectively. From these we can see that the curvature-based potential has enough accuracy when \tilde{c} is a small quantity.

TABLE 2: The error of curvature-based potential between the concave parabolic rotator and the particle ($n = 6$).

\tilde{c}	$(\tilde{U}_6)_{\text{numerical}}$	$(\tilde{U}_6)_{\text{polynomial}}$	$\delta = \frac{(\tilde{U}_6)_{\text{polynomial}} - (\tilde{U}_6)_{\text{numerical}}}{(\tilde{U}_6)_{\text{numerical}}}$
0.5	1.999990099763677	2.125000000000000	0.062505259526582
0.4	1.767008983006020	1.840000000000000	0.041307666059404
0.3	1.548796643131850	1.585000000000000	0.023375151946961
0.1	1.162688575661165	1.165000000000000	0.001987999527320
0.05	1.078359520840800	1.078750000000000	3.621048005354316e - 004
0.03	1.046242770650530	1.046350000000000	1.024899310924430e - 004
0.01	1.015137871366782	1.015150000000000	1.194776942179518e - 005
0.005	1.007530503256329	1.007537500000000	6.944448479219859e - 006
0.001	1.001496244320401	1.001501500000000	5.247827567111332e - 006
0.0001	1.000145034778507	1.000150015000000	4.979499292623452e - 006

6. Discussions

6.1. *Local Properties of the Curvature-Based Potential.* The integrand in (3) is

$$g(\tilde{r}, \tilde{c}) = \frac{1}{\tilde{r}^{n-1}} \left[\tilde{r} - \frac{1}{\tilde{z}_p \tilde{c}} + \frac{1}{\tilde{z}_p \tilde{c}} \sqrt{1 - 2\tilde{z}_p \tilde{c} + (\tilde{z}_p \tilde{c} \tilde{r})^2} \right]. \quad (25)$$

The domain of integration is $[h, \infty)$. Hence the interaction between parabolic rotator and the particle reflects the global properties of the system. However, in the viewpoint of physics, the short-range interaction pair-potential determines that the particle p mainly interacts with the nearest zone of curved surface body. Thus, from the mathematical point of view, the distribution of integrand $g(\tilde{r}, \tilde{c})$ is of highly local properties, which can be further proved as follows. For convex and concave parabolic rotators, there are

$$\begin{aligned} \hat{g}(\tilde{r}, \tilde{c}) &= \frac{1}{\tilde{r}^{n-1}} \left[\tilde{r} + \frac{1}{\tilde{c}} - \frac{1}{\tilde{c}} \sqrt{1 + 2\tilde{c} + (\tilde{c}\tilde{r})^2} \right], \\ \check{g}(\tilde{r}, \tilde{c}) &= \frac{1}{\tilde{r}^{n-1}} \left[\tilde{r} - \frac{1}{\tilde{c}} + \frac{1}{\tilde{c}} \sqrt{1 - 2\tilde{c} + (\tilde{c}\tilde{r})^2} \right]. \end{aligned} \quad (26)$$

The distribution diagrams are shown in Figures 7 and 8. We can see that the values of the integrand mainly distribute in the region of the dimensionless radius $\tilde{r} \in [1, 3]$. Beyond this region the integrand decreases to zero rapidly.

Moreover, we can interpret the mechanism in Figures 7 and 8 concretely. Along with the increase of the radius \tilde{r} , the area of arc surface cutoff by the sphere with center p from the curved surface body gets larger. However, the pair-potential between particle p and particles on the arc surface decreases sharply. Their product will reach the maximum when \tilde{r} comes to a certain value. Later, the effect decreasing potential exceeds that of the increasing area, causing the integrand to decrease rapidly. This is the mathematical foundation for the local properties of the interaction between the particle and the parabolic rotator. Since the local particles of parabolic rotator are mostly distributed on the surface and the surface morphology is depicted by curvatures, the interaction between the particle and parabolic rotator is

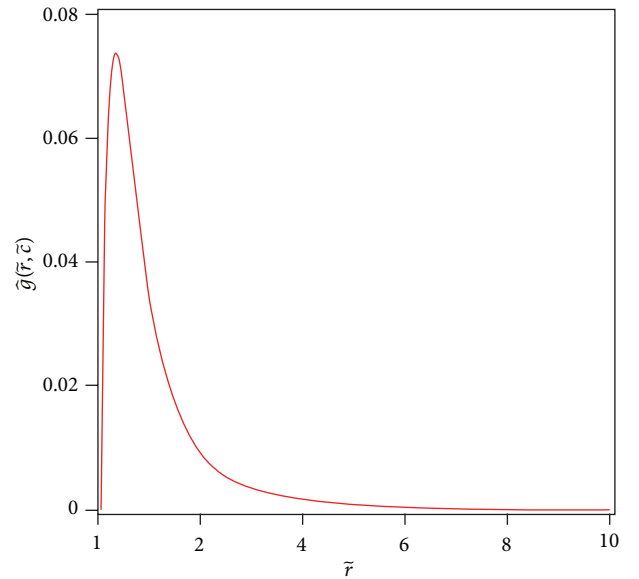


FIGURE 7: The distribution of $\hat{g}(\tilde{r}, \tilde{c})$ along with \tilde{r} when $n = 6$, $\tilde{c} = 0.1$.

mainly determined by curvatures and can be written as the curvature-based form finally.

6.2. *The Driving Force on the Particle.* The dimensional form of the curvature-based potential in (21) is

$$U_n = \bar{U}_n \left[1 + \frac{n-3}{n-4} z_p c + \frac{n-3}{n-4} (z_p c)^2 \right]. \quad (27)$$

Supposing that the movement of the particle is restricted on the axis z , the driving force exerted on the particle in the z direction is

$$\begin{aligned} F_z &= -\frac{\partial U_n}{\partial z_p} = -\bar{U}_n \frac{n-3}{n-4} c \left[1 + 2z_p c \right] \\ &\quad - \frac{\partial \bar{U}_n}{\partial h} \frac{\partial h}{\partial z_p} \left[1 + \frac{n-3}{n-4} z_p c + \frac{n-3}{n-4} (z_p c)^2 \right]. \end{aligned} \quad (28)$$

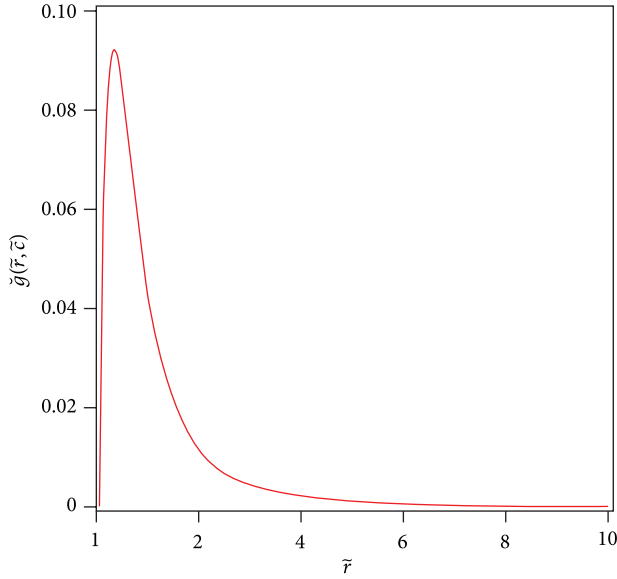


FIGURE 8: The distribution of $\check{g}(\tilde{r}, \tilde{c})$ along with \tilde{r} when $n = 6$, $\tilde{c} = 0.1$.

Here there is $\partial h / \partial z_p = \pm 1$, and it takes minus sign for convex curved surface body and positive sign for concave curved surface body.

If $c \rightarrow 0$, that is, parabolic rotator generates on semifinite plane body, then (28) is

$$F_z = -\frac{\partial \bar{U}_n}{\partial h} \frac{\partial h}{\partial z_p}. \quad (29)$$

Equation (29) is the driving force acting on the particle by semifinite plane body, which is a classical conclusion.

Once $c \rightarrow \infty$, then $F_z \rightarrow \infty$; that is, there are infinite forces acting on the particle if curvatures of vertex of parabolic body tend to infinity. Such vertex with infinite curvatures is a sharp singularity geometrically. Thus, the sharp singularity can induce strong driving force, which provides insight to understand a large amount of abnormal movements around singularities.

Specifically, if such driving force is attractive, strong effect of hydrophilic will cause water droplets come into being around singularities, which can help living organism to absorb water from environment (Figure 9). Otherwise, repulsive force will cause hydrophobic effect and help living organism to discharge water into environment.

The above analysis enhances previous propositions: curved spaces can induce driving forces. Definitely, curvatures can induce driving forces. By changing curvatures, driving forces acting on the particle can be changed, which means that it is possible to regulate movements of particles by noncontacting and geometrical methods.

If the particle P is confined to the parallel curved surface with $h = \text{Const.}$ (Figure 10) and can only move along the generating line of the parallel curved surface, then the particle will sense the tangential force induced by the changing of curvatures. Parabolic body is a particular case of curved surface body, as principle curvatures at vertex are equal; that



(a)



(b)

FIGURE 9: The driving force around singularities: hydrophilic or hydrophobic effect.

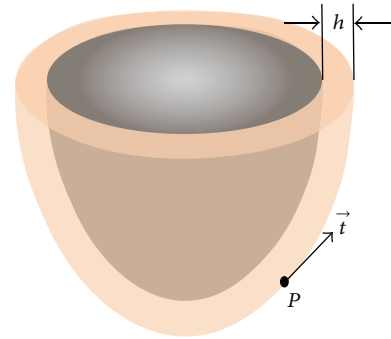


FIGURE 10: The movement of the particle induced by curvatures on the parallel surface.

is, $c_1 = c_2 = c$. But once the particle moves and deviates from the top of vertex, principle curvatures of two directions at the nearest point from the body to the particle come to unequal magnitude. Thus, in order to write the tangential force as a function of the gradient of curvatures, the interaction potential between the particle and general curved surface body should be studied, which will be shown in a subsequent paper.

7. Conclusions

Although the parabolic rotator at micro/nanoscale may be a particular case of curved surface bodies, the propositions deduced from it do not lose universality; that is, they are valid in curved surface bodies with any bending surfaces. In the succeeding papers, we will expand the propositions in this paper to general curved surface bodies. Based on

the progress in this paper, we can say that the propositions derived in the curved surface and curved line will stay valid in the curved surface body as well. In other words, the proposition that micro/nano-curved spaces induce driving force is of universality. It also means that curvature is a crucial factor at micro/nanoscale and should be one of the cores in micro/nanomechanics.

Conflict of Interests

The authors declare that there is no conflict of interests regarding the publication of this paper.

Acknowledgments

This work was supported by the National Natural Sciences Foundation of China (Grant nos. 11072125, 11272175, 11102138, and 10602040) as well as the Natural Science Foundation of Jiangsu province (Grant nos. BK2011075 and BK20130910) and Foundation of Doctoral Supervisor.

References

- [1] N. M. Sherer and W. Mothes, "Cytotubes and tunneling nanotubes in cell-cell communication and viral pathogenesis," *Trends in Cell Biology*, vol. 18, no. 9, pp. 414–420, 2008.
- [2] V. Vogel and M. Sheetz, "Local force and geometry sensing regulate cell functions," *Nature Reviews Molecular Cell Biology*, vol. 7, no. 4, pp. 265–275, 2006.
- [3] B. Habermann, "The BAR-domain family of proteins: a case of bending and binding?" *EMBO Reports*, vol. 5, no. 3, pp. 250–255, 2004.
- [4] É. Lorenceau and D. Quéré, "Drops on a conical wire," *Journal of Fluid Mechanics*, vol. 510, pp. 29–45, 2004.
- [5] D. J. Wold and C. D. Frisbie, "Fabrication and characterization of metal-molecule-metal junctions by conducting probe atomic force microscopy," *Journal of the American Chemical Society*, vol. 123, no. 23, pp. 5549–5556, 2001.
- [6] C. Argento and R. H. French, "Parametric tip model and force-distance relation for Hamaker constant determination from atomic force microscopy," *Journal of Applied Physics*, vol. 80, no. 11, pp. 6081–6090, 1996.
- [7] Y. Yin, C. Chen, C. Lü, and Q. Zheng, "Shape gradient and classical gradient of curvatures: driving forces on micro/nano curved surfaces," *Applied Mathematics and Mechanics*, vol. 32, no. 5, pp. 533–550, 2011.
- [8] J. Y. Wu, Y. J. Yin, X. G. Wang, and Q. S. Fan, "Interaction potential between micro/nano curved surface and a particle located inside the surface (I): driving forces induced by curvatures," *Science China Physics, Mechanics and Astronomy*, vol. 55, no. 6, pp. 1066–1076, 2012.
- [9] J. Y. Wu, Y. J. Yin, K. Huang, and Q. S. Fan, "Interaction potential between micro/nano curved surface and a particle located inside the surface (II): numerical experiment and equipotential surfaces," *Science China: Physics, Mechanics and Astronomy*, vol. 55, no. 6, pp. 1077–1082, 2012.
- [10] J. Israelachvili, *Intermolecular and Surface Forces*, Academic Press, London, UK, 2nd edition, 1991.
- [11] H. C. Hamaker, "The London-van der Waals attraction between spherical particles," *Physica*, vol. 4, no. 10, pp. 1058–1072, 1937.
- [12] L. Bo, H. P. Zhao, and X. Q. Feng, "Spontaneous instability of soft thin films on curved substrates due to van der Waals interaction," *Journal of the Mechanics and Physics of Solids*, vol. 59, no. 3, pp. 610–624, 2011.
- [13] B. Q. Su, H. S. Hu, C. L. Shen, Y. L. Pan, and G. L. Zhang, *Differential Geometry*, People's Education Press, 1979.
- [14] J. Y. Wu, *Biomembrane free energy and the driving forces induced by curvature gradients [Ph.D. thesis]*, School of Aerospace, Tsinghua University, Beijing, China, 2012.